

Winter 2004

# On the Rayleigh -Brillouin scattering in air

Qihua Zheng

*University of New Hampshire, Durham*

Follow this and additional works at: <https://scholars.unh.edu/dissertation>

---

## Recommended Citation

Zheng, Qihua, "On the Rayleigh -Brillouin scattering in air" (2004). *Doctoral Dissertations*. 255.  
<https://scholars.unh.edu/dissertation/255>

This Dissertation is brought to you for free and open access by the Student Scholarship at University of New Hampshire Scholars' Repository. It has been accepted for inclusion in Doctoral Dissertations by an authorized administrator of University of New Hampshire Scholars' Repository. For more information, please contact [nicole.hentz@unh.edu](mailto:nicole.hentz@unh.edu).

# NOTE TO USERS

This reproduction is the best copy available.

**UMI**<sup>®</sup>



ON THE RAYLEIGH-BRILLOUIN SCATTERING IN AIR

BY

QIUHUA ZHENG

(B.S.) Tianjin University, China, 1994

(M.S.) University of New Hampshire, 2000

DISSERTATION

Submitted to the University of New Hampshire

in Partial Fulfillment of

the Requirements for the Degree of

Doctor of Philosophy

in

Physics

December, 2004

UMI Number: 3158684

Copyright 2005 by  
Zheng, Qihua

All rights reserved.

### INFORMATION TO USERS

The quality of this reproduction is dependent upon the quality of the copy submitted. Broken or indistinct print, colored or poor quality illustrations and photographs, print bleed-through, substandard margins, and improper alignment can adversely affect reproduction.

In the unlikely event that the author did not send a complete manuscript and there are missing pages, these will be noted. Also, if unauthorized copyright material had to be removed, a note will indicate the deletion.

**UMI**<sup>®</sup>

---

UMI Microform 3158684

Copyright 2005 by ProQuest Information and Learning Company.

All rights reserved. This microform edition is protected against unauthorized copying under Title 17, United States Code.

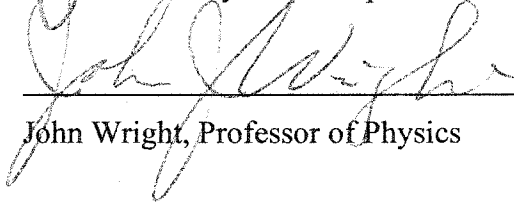
ProQuest Information and Learning Company  
300 North Zeeb Road  
P.O. Box 1346  
Ann Arbor, MI 48106-1346

This dissertation has been examined and approved.



---

Dissertation director, James Ryan  
Professor of Physics and Space Science Center (EOS)



---

John Wright, Professor of Physics



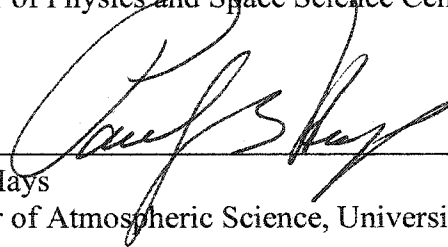
---

Richard Kaufmann, Professor of Physics



---

Martin Lee  
Professor of Physics and Space Science Center (EOS)



---

Paul B. Hays  
Professor of Atmospheric Science, University of Michigan

10 December 2004

Date

## DEDICATION

*To my wife*

## ACKNOWLEDGEMENTS

I am indebted to my advisor, Professor James Ryan, who gave me the opportunity and support for my doctoral research, who always taught me to attend to concise physics when facing complicated problems, and who has been generous with inspiring ideas and suggestions. I want to thank Professor Paul Hays of Michigan for his invaluable suggestions and help from the very beginning of this study. I want to thank Professor Berrien Moore for his encouragement and support throughout the whole process.

I am grateful to have learned kinetics, fluid mechanics, and atmospheric physics -- all of which have been fundamental to my research—from Professor Richard Kaufmann and Professor Martin Lee. I also thank Professor John Wright for his astute insights concerning my thesis topics.

I thank Dr. Ivan Dors, my friend and colleague, for giving me comments and suggestions with regard to every aspect of my work. I wouldn't have gotten this far without him. I want to thank Professor Mark McConnell for his invaluable assistance. Many thanks also to Michael Dehring of Michigan Aerospace Corporation for his help with GroundWinds instrument and data analysis.

I thank Professor John Dawson for his kindness and his Quantum Mechanics classes, from which I learned a lot. I want to thank Professors Robert Lambert, Harvey Shepard and Joseph Hollweg for their great lectures on Math, Quantum and statistical theory.

Finally, I want to thank my parents, Aizhen Yan and Guilun Zheng, my sister, Yihua Zheng, and her husband, Robert Herschbach, and my brother, Zhuohua Zheng, for their steady support.



## TABLE OF CONTENTS

DEDICATION.....	iii
ACKNOWLEDGEMENTS.....	iv
LIST OF TABLES.....	viii
LIST OF FIGURES.....	ix
ABSTRACT.....	xiii
CHAPTER	
1 INTRODUCTION.....	1
1.1 The Problem.....	1
1.1.1 Rayleigh Scattering and Wind Measurement.....	2
1.1.2 Three Scattering Regimes.....	4
1.1.3 Current Rayleigh-Brillouin Scattering Models.....	8
1.1.4 Light Transmission in the Atmosphere.....	10
1.2 Molecular Scattering Spectrum.....	11
1.3 Wind Measurements.....	13
1.3.1 The Atmosphere.....	13
1.3.2 The GroundWinds Lidar System.....	14
1.4 Objective of Research.....	18
1.5 Preview.....	19
2 RAYLEIGH-BRILLOUIN SCATTERING IN AIR.....	21
2.1 Rayleigh Scattering Spectra.....	22
2.1.1 The Relations Between Spectrum of Light Scattering in Gases and $G(\mathbf{r}, t)$ ..	24
2.1.2 The Van Hove Space-Time Density Correlation Function $G(\mathbf{r}, t)$ ..	31

3 MODELING OF RAYLEIGH-BRILLOUIN SCATTERING SPECTRUM.....	35
3.1 Hydrodynamics Approach – Rayleigh-Brillouin Scattering.....	35
3.2 The Kinetic Approach of Rayleigh-Brillouin Scattering.....	48
3.2.1 Linearized Boltzmann Equation .....	48
3.2.2 Homogeneous Case.....	50
3.2.3 Inhomogeneous Case .....	53
3.2.4 Diatomic Gases .....	57
3.3 An Alternative Approach and Tenti’s Model .....	65
4 RAYLEIGH-BRILLOUIN SCATTERING SPECTRUM AND TEMPERATURE PROFILE .....	69
4.1 Introduction.....	69
4.2 Instrument Description/Specifications.....	70
4.2.1 Laser.....	70
4.2.2 Telescope .....	70
4.2.3 Spectrometer .....	71
4.2.4 Optics .....	72
4.2.5 Detector.....	73
4.3 Clean Spectra.....	74
4.3.1 Description of GroundWinds Data .....	75
4.3.1.1 Criteria for Data Selection .....	76
4.3.2 Broadening Effects, Turbulence and Line-of-Sight Winds .....	77
4.3.2.1 Instrument Broadening.....	79
4.3.3 Elimination of Broadening Effects and Deconvolve Algorithm.....	80
4.3.3.1 Thermal Blooming.....	82
4.3.4 Aerosol and Planetary Boundary Layer (PBL).....	84
4.4 Modified Hydrodynamic Model.....	87

4.5 Tenti's S6 Model and Temperature Profiling.....	89
4.6 Landau-Placzek Ratio.....	91
4.7 RBS Spectra and Temperature Profile.....	92
4.7.1 Rayleigh Spectra.....	92
4.7.2 Temperature Profile.....	101
4.7.3 Temperature Bias Caused by Non-Uniform Lidar Returns.....	108
4.8 Discussions.....	110
5 MOLECULAR BACKSCATTERING COEFFICIENTS IN THE AIR.....	115
5.1 Lidar Equation and Lidar Ratio.....	115
5.2 Retrieval of Molecular Backscatter Coefficients and Extinction Coefficients...	117
5.2.1 Backscatter Coefficients by Rayleigh Theory.....	117
5.2.2 Backscatter Coefficients from GroundWinds Data.....	119
5.3 An Alternative Method to Retrieve the Backscattering Coefficients.....	127
5.4 Conclusions and Discussions.....	129
6 ON THE RAYLEIGH-BRILLOUIN SCATTERING WITH EXTERNAL FORCES	132
6.1 Introduction.....	132
6.2 Sound.....	133
6.3 Rayleigh-Brillouin Scattering in Gases with External Forces.....	134
7 CONCLUSIONS.....	143
REFERENCES.....	145
APPENDIX.....	149
The Plasma Dispersion Function.....	149

## LIST OF TABLES

Table 1.1	Type of Factors affecting Rayleigh Scattering in Air.....	18
Table 4.1	Laser Specifications.....	70
Table 4.2	Telescope Specifications.....	71
Table 4.3	Molecular and Aerosol Etalon Specifications.....	72
Table 4.4	Depolarization Ratios for Major Air Species at Various Wavelength* .....	113

## LIST OF FIGURES

Figure 1.1	During a Rayleigh-Brillouin scattering process, an incident photon was scattered by a molecule. It is first absorbed by the molecule, induces a dipole electric field, and then reemitted at the same frequency. The differential cross-section is proportional to the fourth power of the incident photon frequency..	2
Figure 1.2	Wind velocity is determined by the Doppler shift between the unshifted Rayleigh-Brillouin scattering (RBS) model and the measured RBS spectrum. GroundWinds lidar is the first lidar system that provides a chance to directly measure the RBS spectra in the air .....	3
Figure 1.3	Three regimes are categorized by the kinetic parameter $\gamma$ , whose physical meaning is the ratio of the incident light wavelength and the mean free path of the scattering medium -- for our purposes, the atmosphere.....	5
Figure 1.4	This is a typical Rayleigh-Brillouin Scattering spectrum in the hydrodynamic regime. A He-Ne laser with a 632.8 nm wavelength is beamed into the water and Benedek et al (1971) measured the Rayleigh-Brillouin scattering spectrum. The distance between the sideband peaks and the central peak depends on the sound velocity of water.....	7
Figure 1.5	Plot of the kinetic S6 model with a fitted Gaussian of the same area. There are two components on the 'shoulder' of the model compared to the Gaussian distribution .....	9
Figure 1.6	Scattering components from laser illumination molecular gases (not to scale). For Nitrogen, Vibrational Raman accounts for about 0.1% of the total and $2000\text{cm}^{-1}$ away from the central. Rotational Raman raman lines accounts for 1-2% of the total and off by $10\text{-}100\text{cm}^{-1}$ from the Cabannes line. The width of Rayleigh-Brillouin line: about $0.03\text{-}0.04\text{cm}^{-1}$ .....	11
Figure 1.7	The atmosphere of the earth.....	13
Figure 1.8	Direct detection Doppler lidar. ....	16
Figure 3.1	Relationship between $q$ , $k$ and $k_{sc}$ .....	39
Figure 3.2	Representation of molecular light scattering spectrum.....	41
Figure 3.3	Two molecules/atoms colliding process .....	49
Figure 3.4	Change of S6 model from kinetic regime to hydrodynamic regime. The first one is S6 model in kinetic regime and the bottom one illustrates S6 model in the hydrodynamic regime, while the middle one is in between ( $\gamma=5.0$ ).....	68
Figure 4.1	Transformation of Fabry-Pérot circular fringes to linear.....	73

Figure 4.2	Conceptual ray trace illustrating the CLIO concept. ....	73
Figure 4.3	CCD Lidar Detector time history. As the light scatters from different altitudes, the image is shifted across the detector (steps a through e). At the end the image is shifted back to the start for the next laser pulse (step e to a). Only the segment of the CCD marked "open" is actually exposed to light.....	74
Figure 4.4	A delta-function is broadened after passing through an optical system. ....	78
Figure 4.5	Illustration of distribution of registered photons on the detector with (a) a real measurement and (b) a perfect measurement.....	78
Figure 4.6	Illustration of a function broadened by a Lorentzian function .....	82
Figure 4.7	Measured RBS spectrum with little (ignorable) aerosol signals. Blue solid line is the fit of kinetic S6 model. Black solid line is the measured RBS spectrum. Pink lines are the molecular, aerosol, and background components. (a) Aerosol signal is large. (b) Aerosol signal is very small (ignorable).....	86
Figure 4.8	The modified hydrodynamic model. Three Lorentzian lineshapes are overlapped and their superposition is shown as the thick black line. The displaced length is determined by the sound speed of the air molecules.....	88
Figure 4.9	Shown above is the kinetic model. The white line is the S6 kinetic model is compared with a Gaussian. ....	89
Figure 4.10	Aerosol signal strength .....	93
Figure 4.11	Molecular signal strength.....	94
Figure 4.12	A plot of reference fringe.....	95
Figure 4.13	A plot of raw fringe. The corresponding altitude is 3.5 km.....	96
Figure 4.14	One deconvolved Rayleigh-Brillouin scattering spectrum .....	96
Figure 4.15	Deconvolved Rayleigh-Brillouin scattering spectrum(upper) and deconvolved reference signal (down) .....	97
Figure 4.16	Comparison of raw RBS fringe and deconvolved RBS spectrum. ....	97
Figure 4.17	Comparison of S6 model and a thermal broadening Gaussian. They are plotted under same temperature .....	99
Figure 4.18	Plot of S6 model at same atmospheric conditions except the temperature. Black solid line corresponds to a temperature 300K while the blue dash line corresponds to 260K .....	100
Figure 4.19	Landau Placzek ratio vs. altitude (km) .....	101

Figure 4.20	Retrieved temperature profile at 6:00am on July 31 <sup>st</sup> , 2002.....	103
Figure 4.21	Retrieved temperature profile from RBS raw fringe at 4:00am on July 31 <sup>st</sup> , 2002.....	104
Figure 4.22	Retrieved temperature profile from deconvolved RBS spectra. The data was taken on Feb 20, 2003 at 2:15am EST.....	105
Figure 4.23	Fit the kinetic S6 model to the measured RBS fringe. The black solid line is the raw RBS spectrum, the red line is the molecular part and purple line stands for the aerosol part. The upper fitting image is corresponding to an altitude of 4.93 km and the lower is corresponding to an altitude of 4km ...	106
Figure 4.24	Temperatures are biased up by the non-uniform distribution of photometric returns at different altitude .....	109
Figure 4.25	Plot of variance over 40 consecutive measurements of RBS spectra, they are a) a variance plot from data taken at 10:00 EST July 31, 2002 and b) a variance plot from data taken at 6:00 EST July 31, 2002.....	112
Figure 5.1	A typical Rayleigh spectrum: photon returns versus different channels .....	120
Figure 5.2	One lidar photometric returns of the molecular channels.....	122
Figure 5.3	the overlap function of GroundWinds NH lidar system.....	122
Figure 5.4	Fitting scheme.....	123
Figure 5.5	Theoretical molecular backscatter coefficients of air (by eq. 5.11).....	124
Figure 5.6	Comparison between measured backscatter coefficients (black solid line) and that from theory (pink dotted line).....	126
Figure 5.7	Comparison of backscatter coefficients from GroundWinds lidar measurements, from theory, and calculated by using Landau-Placzek ratio. Red line stands for theoretical BC (Backscatter Coefs) for the air. Black line stands for calculated BC from photometric returns of GWNH data. Purple line stands for calculated BC using Landau-Placzek ratio from GWNH data. Blue square line stands for theoretical BC value assuming the air in the hydrodynamic regime .....	126
Figure 5.8	Simulation of photometric returns using (a) theoretical value and (b) Twice of the theoretical value of molecular backscatter coefficients.....	128
Figure 5.9	Retrieved aerosol molecular ratio by fitting the S6 model to the measured RBS spectra.....	130

Figure 6.1 The spectral change when an external force is applied. The blue line is the RBS spectrum of standard air at 300K and 1atm without an external force. The black line is the RBS spectrum of air, which subjects to an external force. .... 142

Figure 6.2 A plot of change of the RBS spectrum when an acoustic wave is propagating in the air. The blue line is for the normal air. The black line is the RBS spectrum for the air with a propagating sound wave. The sound power level is 100db and the sound frequency is 1000Hz. .... 142



## ABSTRACT

### ON THE RAYLEIGH-BRILLOUIN SCATTERING IN AIR

by

Qihua Zheng

University of New Hampshire, December, 2004

GroundWinds lidar system is a high-spectral-resolution lidar system that can directly measure the Rayleigh-Brillouin scattering (RBS) spectra, from which the wind, temperature, and turbulence in the troposphere can be measured. Its transmitter is a double-frequency Nd-YAG laser at 532nm. Most of the data used in this research were taken on 31 July 2002.

A widely used mathematic model—the S6 model—is fitted to the measured RBS spectra. The discrepancies between the measured temperature from the Rayleigh-Brillouin spectra and from the radiosonde, combined with the discrepancies between the model and the measured RBS spectra, indicate that there is room for the S6 model to be improved. On the other hand, they also reveal that air turbulence information, which—along with the variance analysis—can be used in the turbulence measurements. The change in Rayleigh-Brillouin scattering spectra in fluids under external forces was theoretically investigated and can be used for acoustic wave detections, low-frequency plasma studies and other applications.

In addition, Rayleigh backscatter coefficients in air, for the first time, were measured using the molecular photometric returns. The measured molecular backscatter coefficients are approximately twice as large as their theoretical counterparts. This could be related to the collective effects of air molecules, i.e., the scattering structure factor.

# CHAPTER 1

## INTRODUCTION

### 1.1 The Problem

Rayleigh scattering is important in the analysis of chemical solutions, temperature measurements of flares, and other applications in physics, chemistry, and engineering. The blue sky and red sunset are a result of this phenomenon. The differential cross section for Rayleigh scattering in a homogenous gas can be calculated using electromagnetic theory, both classically and quantum mechanically. However, Rayleigh scattering spectra in many gas species, particularly when they are in the kinetic regime, are complicated. Things become more complicated when different gas species are present—as with Rayleigh scattering in air—because of depolarization (the scattered photons have a polarization different from that of incident photons) and inter-diffusion of the two species.

We will study a component of Rayleigh scattering, Brillouin scattering, using the GroundWinds lidar system. Rayleigh-Brillouin scattering spectra are difficult to measure because of the required spectral resolution. The emergence of laser technology in 1960s, however, has provided the necessary monochromatic radiation. Rough Rayleigh-Brillouin scattering spectra were measured (G. Fiocco 1968; Schwiesow R. 1981) with early lidar systems. The modern (GroundWinds) lidar system is able to acquire much better measurements of Rayleigh-Brillouin scattering spectra.

### 1.1.1 Rayleigh Scattering and Wind Measurement

When a monochromatic light beam propagates in the atmosphere at a frequency different from that of molecular and atomic transitions, it will be scattered by the molecules in its path. If the scattered light frequency is unchanged, we call this Rayleigh scattering. However, this is never exactly the case, because the scattered light always disperses in frequency. In addition, there are also two distinct shifted components arising, respectively, from stochastic pressure fluctuations in the atmosphere; these are known as the Stokes and anti-Stokes components. The scattering due to the pressure fluctuations can be viewed as a process in which the incident light is scattered by acoustic phonons. This is called Brillouin scattering.

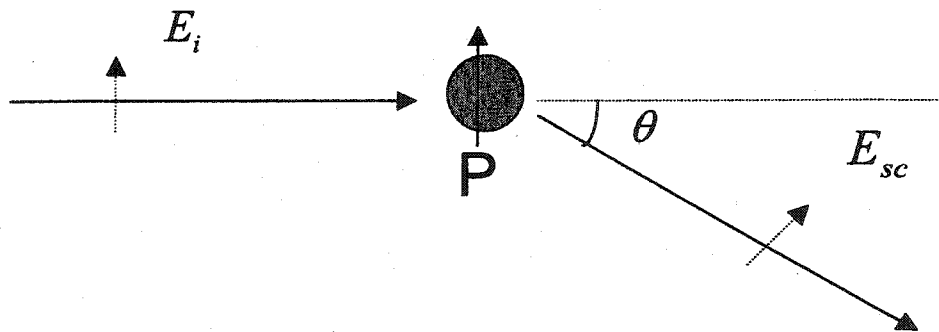


**Figure 1.1** During a Rayleigh-Brillouin scattering process, an incident photon was scattered by a molecule. It is first absorbed by the molecule, induces a dipole electric field, and then reemitted at the same frequency. The differential cross-section is proportional to the fourth power of the incident photon frequency

Young (1983) demonstrated that Brillouin scattering is a component of Rayleigh scattering, since Lord Rayleigh treated both of them in his celebrated work. Technically speaking, whenever we mention Rayleigh scattering or Rayleigh-Brillouin scattering (RBS), we are actually referring to the same phenomenon, although a distinction commonly exists in the vernacular of radiative transfer.

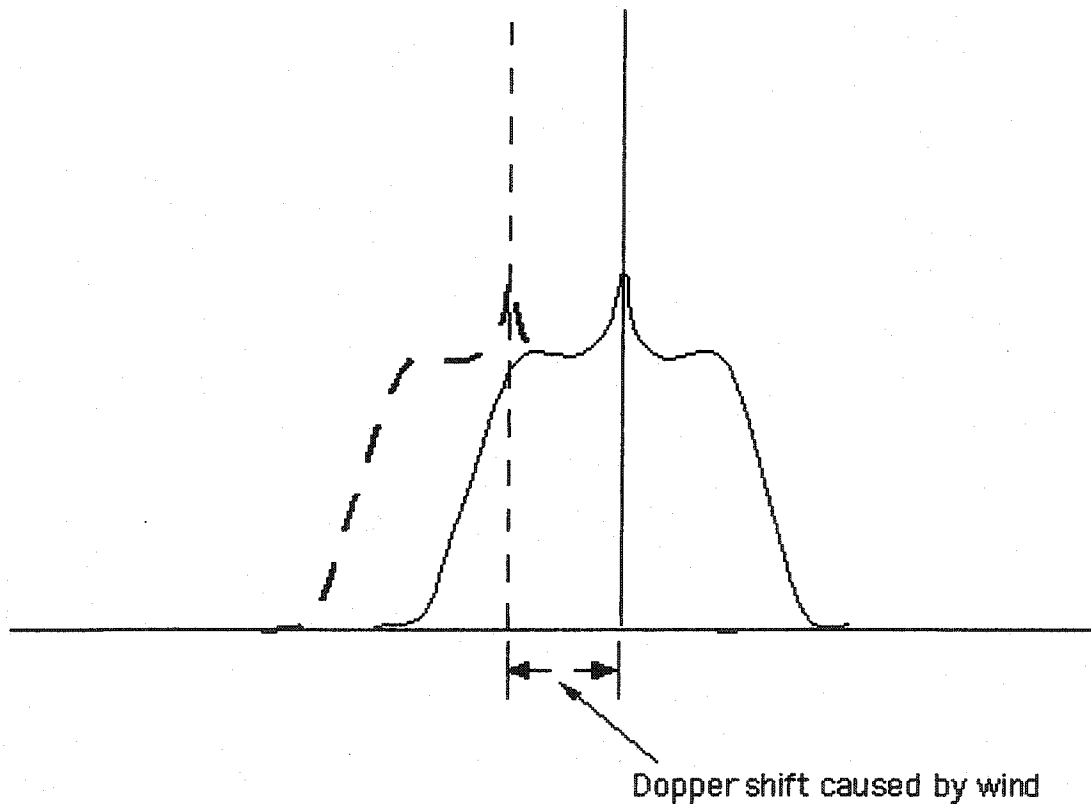


**Figure 1.2** Wind velocity is determined by the Doppler shift between the unshifted Rayleigh-Brillouin scattering (RBS) model and the measured RBS spectrum. GroundWinds lidar is the first lidar system that provides a chance to directly measure the RBS spectra in the air.

Measuring tropospheric winds was the design goal for the GroundWinds instrument. The measurement of wind velocity by a lidar system makes use of the Doppler effect (as shown in Figure 1.2). The bulk motion of a parcel of air molecules in the wind scatters the light systematically to a higher or lower frequency, depending on the wind direction. If we know the unshifted frequency, we can compare it to the spectrum produced by the wind. This simple idea as described below is complicated by the fact that the shape of the scattered spectrum is more complicated than the original monochromatic beam. Knowledge of the shape of the frequency dispersion for Raleigh and Brillouin scattering will allow better measurements of the wind velocity.

### 1.1.2 Three Scattering Regimes

Before we proceed to discuss Rayleigh-Brillouin scattering in the atmosphere, it is helpful to define three different scattering regimes by comparing the molecular mean free path to the wavelength of the light. If the mean free path of a scattering gas medium is much larger than the wavelength of the incident light (very tenuous gas), we say the scattering occurs in the **Knudsen regime**. In this regime, the Rayleigh scattering spectrum is approximately Gaussian, because the gas is collisionless with no collective effects. If the mean free path of the scattering gas medium is much smaller than the wavelength of the incident light (dense gases or liquids), we call this the **hydrodynamic regime**; in this case, the Rayleigh-Brillouin scattering spectrum is composed of three

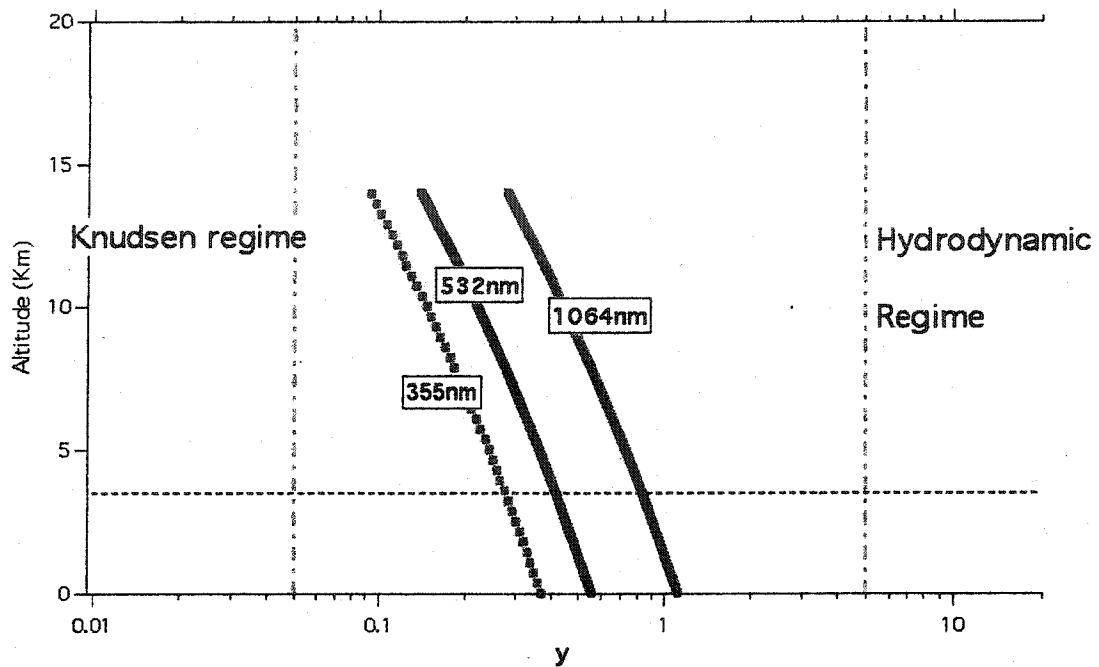


**Figure 1.3 Three regimes are categorized by the kinetic parameter  $y$ , whose physical meaning is the ratio of the incident light wavelength and the mean free path of the scattering medium -- for our purposes, the atmosphere**

Lorentzians displaced by the corresponding sound velocity of the scattering medium. If the mean free path of the scattering gas medium is comparable to the wavelength of the incident light, we call this the kinetic regime (pressure of 1 atm and lower); the Rayleigh-Brillouin scattering spectrum is a complicated mixture of the Knudsen and hydrodynamic spectra. Figure 1.3 shows the three different spectra with respect to standard lidar wavelengths. The parameter  $y$  is a dimensionless pressure quantity described in chapter 3.

When a scattering process occurs in the Knudsen regime, it implies the scattering medium (gas) is dilute and the scattering spectrum is a Gaussian with a width determined by the average thermal speed, appropriately Doppler shifted by the bulk velocity. By contrast, the hydrodynamic regime applies to or very dense gases, The three-Lorentzian distribution (Figure 1.4) occurs. We don't know exactly the RBS spectrum of the air because it is in the kinetic regime for visible, near infrared and near ultraviolet. What we do know is that the larger the kinetic parameter  $\gamma$  is, the more structured the RBS spectra are. The light spectra in the Knudsen regime and the hydrodynamic regime are simple and can be described analytically. The equations that describe the processes in the hydrodynamic regime are mass conservation equation, momentum conservation (Navier-Stokes) equation and energy conservation equation. Unfortunately, the mean free path in the atmosphere is comparable to the wavelength for all lidar applications. Thus Rayleigh-Brillouin backscattering as a remote sensing probe of the atmosphere typically falls into the kinetic regime. In the kinetic regime, Boltzmann or Boltzman-like equations are necessary to describe the scattering phenomenon.

When Rayleigh first studied the elastic light scattering in the air (Rayleigh 1871; Rayleigh 1899), the Rayleigh line could not be resolved. Mandelshtam and Brillouin independently found that frequency of the scattered light was shifted by an amount proportional to the sound speed in air (Mandelshtam 1913; Brillouin 1922). After the discovery of Raman scattering (Raman, 1928), Gross (1930), in his studies on Raman scattering in liquids, discovered a triplet structure (ref. Figure 1.4). This triplet structure was later explained (Landau 1934) as two shifted Brillouin scattering peaks and one undisplaced part—the Gross line. Landau and Placzek (1934) also showed that, in

liquids, the ratio of the outer Brillouin components to the intensity of the whole triplets is approximately the ratio of specific heats. They also claimed that the width of the Gross line, caused by non-propagating entropy fluctuations, was proportional to the thermal diffusivity of the scattering medium.

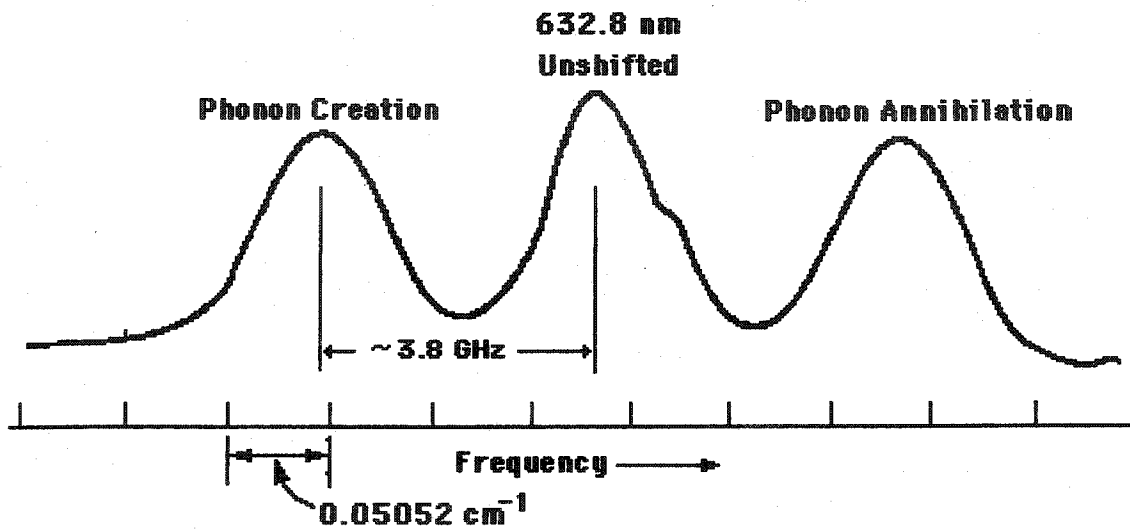


**Figure 1.4** This is a typical Rayleigh-Brillouin Scattering spectrum in the hydrodynamic regime. A He-Ne laser with a 632.8 nm wavelength is beamed into the water and Benedek et al (1971) measured the Rayleigh-Brillouin scattering spectrum. The distance between the sideband peaks and the central peak depends on the sound velocity of water.



### 1.1.3 Current Rayleigh-Brillouin Scattering Models

The Rayleigh-Brillouin scattering spectrum in the atmosphere has long been assumed to be a Gaussian by many researchers. That assumption is not correct; the molecular scattering spectrum in gases is more structured than previously considered. Since 1964, Yip (1964,1965,1967,1971) and his collaborators published a series of well-known papers on the Rayleigh-Brillouin scattering in rarefied gases. In these studies, they employed current kinetic theory and the BGK (1954) model to solve the linearized Boltzmann equation. They obtained a Rayleigh-Brillouin Scattering spectrum for monatomic gases, and showed that the RBS spectrum in monatomic gases with pressure below one bar had more structure than was commonly assumed. Tenti (1974) extended this research to molecular gases by making use of the linearized kinetic Wang-Chang and Ulenbeck (WCU) equation that includes molecular internal energies not considered in the earlier BGK model. Several experiments (May 1980, Sandoval 1976, Lao 1976) were conducted in the lab to verify this model with some molecular gases and the results showed a better fit to the data. However, among these verifications, there was apparently only one experiment in the literature conducted on nitrogen in the hydrodynamic regime and none under typical atmospheric conditions. Kattawar and Young (1983) concluded that Tenti's S6 model (shown in Figure 1.5) is the best model available for atmospheric applications based on those experimental results. Since then the S6 model has not only been used in the Lidar measurements of atmospheric parameters but also applied to many other studies such as aerospace engineering researches (Fielding 2002; Xingguo Pan 2002).

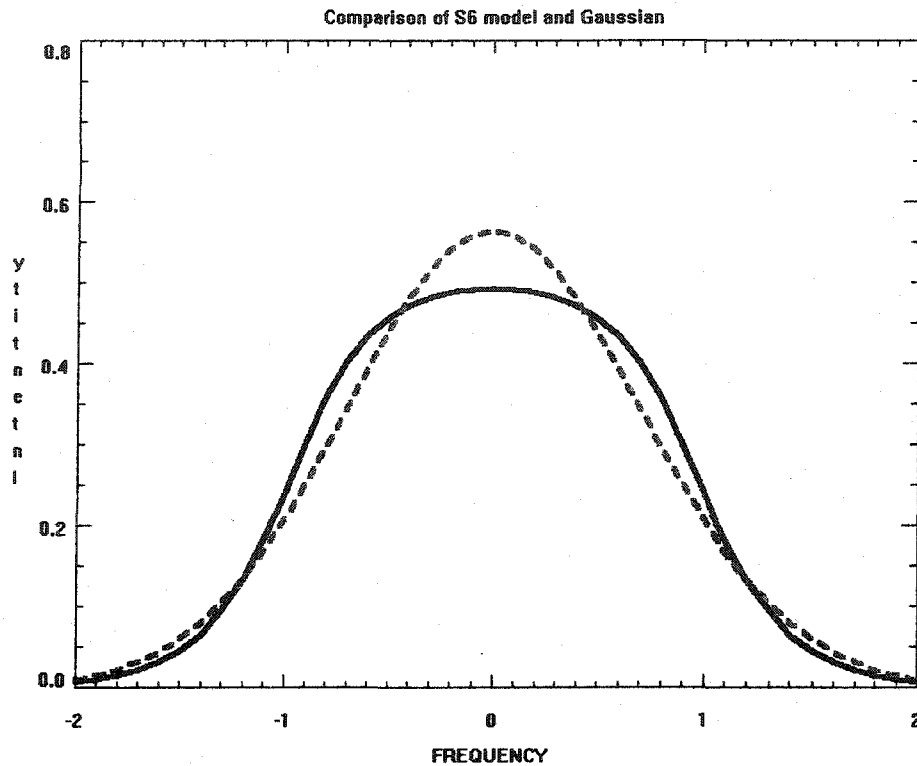


**Figure 1.5** Plot of the kinetic S6 model with a fitted Gaussian of the same area. There are two components on the 'shoulder' of the model compared to the Gaussian distribution

Kattawar and Young (1983) expressed two concerns about the kinetic S6 model. Firstly, air is a molecular mixture of nitrogen and oxygen rather than a single molecular species. Secondly, there should be an incoherent scattering component due to molecular anisotropies. This part might be small -- less than 5 percent -- but it could affect some measurements. These two issues are not included or discussed in any current models. Kattawar and Young also raised some other problems with the kinetic S6 model. They then concluded that because of approximation in the S6 model it would be difficult to measure the temperature profile to better than 1 K. In addition, since neither the

Boltzmann nor Boltzmann-like (such as WCU equation) equation can be solved analytically, any of the models we discussed here will be an approximation. Another important fact is that to date there is no lab experiment known that was performed on the two main species of the air—oxygen and nitrogen, either pure or mixed, under typical atmospheric conditions. Altogether, without a controlled laboratory experiment or, more importantly, atmospheric measurements on air, we cannot judge how these effects listed above will depart from the kinetic S6 model.

#### **1.1.4 Light Transmission in the Atmosphere**

Light transmission in the atmosphere is an important issue in space science research and atmospheric research. The turbulent atmosphere has a large effect on the backscattered signal. Rayleigh scattering, in which light is scattered by air molecules, therefore is important to light transmission studies.

The GroundWinds incoherent lidar system has more than twenty spectral channels for the lidar returns. This feature allows us to study the molecular backscatter coefficients which have been taken to be those predicted by classical electromagnetic theory (Yan 2000; Chen 2002; Sicard 2002).

The attenuation of a light beam in the molecular air free of aerosols is determined by the Rayleigh scattering cross sections or molecular extinction coefficients. This was first calculated by Lord Rayleigh in 1880's and later by Cabannes (1921), who included the effects of the anisotropy of gas molecules. Tabulations of Rayleigh scattering coefficients for different frequencies are based on electromagnetic theory (Penndorf

1957; Bates 1984; Bucholtz 1995) and measurements of air anisotropies. One experimental measurement (Hans Naus 2000) was performed on nitrogen gas in the lab. However, so far there is not any experiment verification conducted on the real atmosphere. With the incoherent GroundWinds lidar systems, we are able to measure the backscatter and extinction coefficients for air.

## 1.2 Molecular Scattering Spectrum

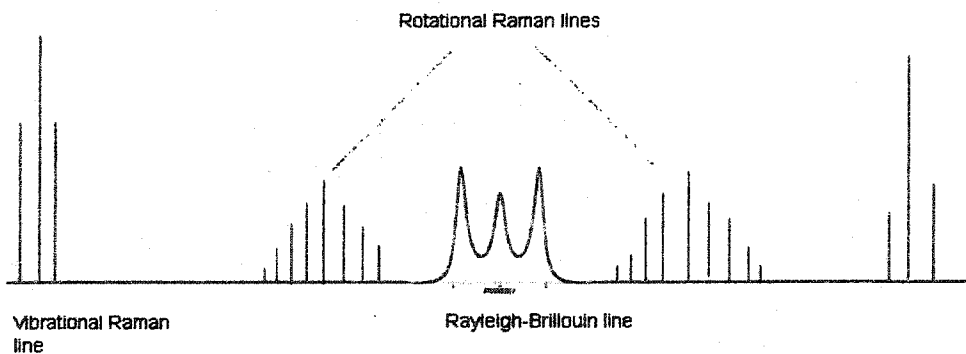


**Figure 1.6 Scattering components from laser illumination molecular gases (not to scale). For Nitrogen, Vibrational Raman accounts for about 0.1% of the total and  $2000\text{cm}^{-1}$  away from the central. Rotational Raman raman lines accounts for 1-2% of the total and off by  $10\text{-}100\text{cm}^{-1}$  from the Cabannes line. The width of Rayleigh-Brillouin line: about  $0.03\text{-}0.04\text{cm}^{-1}$ .**

Although we are only interested in Rayleigh-Brillouin scattering in the air, it is necessary to appreciate other molecular scattering processes. Moreover, these scattering processes are historically intertwined with Rayleigh scattering. When Lord Rayleigh treated light scattering in the air, Raman scattering and Brillouin scattering were still

unknown. Figure 1.6 shows a spectral distribution of molecular light scattering components. The spectral lines far outside are vibrational Raman lines. These are related to the vibrational energy of molecules. The Rayleigh-Brillouin line is located in the middle with its fine structure—three Lorentzians in hydrodynamic regime. Rotational Raman lines, in figure 1.6, are usually not far from elastic Rayleigh-Brillouin scattering line spectrally. Rotational Raman scattering is produced by rotational transitions of the (diatomic) molecules during the scattering process. Normally the backscattered intensities of shifted Raman scattering components—including both translational and vibrational Raman scattering—are weak compared to the “unshifted” Rayleigh-Brillouin scattering (RBS) counterparts in the middle. This is because RBS intensity is proportional to the molecular polarizability while the intensities of Raman scatterings are proportional to the spatial gradient of molecular polarizability. For the main molecular species in air, such as nitrogen and oxygen, their polarizabilities are nearly uniform. Therefore the Raman scattering is a weak process compared to Rayleigh-Brillouin scattering, our interest in this study.

## 1.3 Wind Measurements

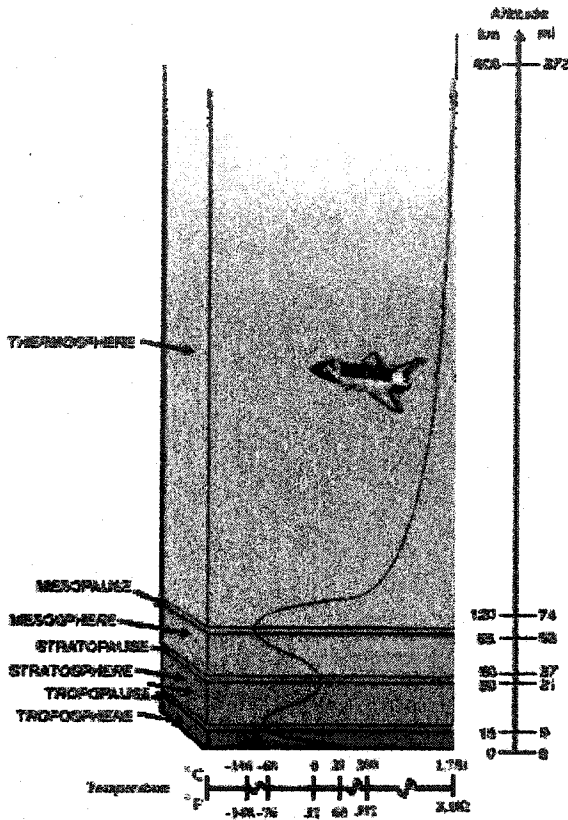


Figure 1.7 The atmosphere of the earth

### 1.3.1 The Atmosphere

A gaseous layer called the atmosphere surrounds the Earth. Scientists divide the atmosphere into several sub layers according to the temperature changes and gas motion. These are the troposphere, stratosphere, mesosphere and thermosphere. From the surface of the Earth to about 8-14 kilometers high is the troposphere. Almost all weather occurs

here. The gases in this layer are relatively dense. The temperature decreases with altitude in this region. The lapse rate is about 8-12 K per kilometer. The temperature decrease halts at the tropopause, which divides the troposphere and the stratosphere. The tropopause and the troposphere together are called the lower atmosphere. This part of the atmosphere is important because it provides the basic constitutional needs of the life. As stated earlier, GroundWinds lidar system is a ground based lidar system whose main goal is to obtain better measurements of the wind velocity with the goal of improving the quality of weather forecasts. Its working region is mostly in the troposphere. So when 'the air' or 'the atmosphere' is mentioned, we are referring to the lower atmosphere.

The air is mainly composed of nitrogen (78%), oxygen (21%) and argon (1%). Other than these, there is also some water vapor (0~5%), ozone and carbon dioxide. Among these components, nitrogen and oxygen are dual-atom molecular gases. They constitute 99% of dry air. Water, ozone and carbon dioxide are polyatomic molecular gases. In addition to these molecular and atomic gases, there is dust and molecular clusters named aerosols suspended in the air. These aerosols play a significant role in light scattering. The planetary boundary layer (PBL) of the atmosphere is rich in aerosols, many produced by the human activity. These aerosols enhance the scattering by air molecules most aerosols lie below the boundary layer.

### **1.3.2 The GroundWinds Lidar System**

As the name suggests, a Doppler lidar system utilizes the Doppler shift to determine the wind velocities. Generally, a Doppler lidar system has four key elements:

1) a laser system to generate the light source, 2) a transmitting telescope that sends the laser beam into the scattering media, 3) a receiver that includes a receiving telescope and related optical subsystems, and 4) a data acquisition system.

Basically, there are two types Doppler wind lidar systems: incoherent (Abreu 1981; Chanin 1989; Tepley 1991; Flesia 1999; Gentry 2000) and coherent (Huffaker 1966; Huffaker 1976; Kavaya 1989) Doppler wind lidar systems. Among the incoherent lidar systems, fringe imaging direct lidar system and double-edge lidar system are the most common wind lidar systems. For direct lidar measurements, molecular lidar measurements have many advantages over the aerosol lidar measurements (Fischer 1995; McKay 2000), since it is sensitive to the entire troposphere—not just the PBL. Double-edge method (Chanin 1989; Korb 1998; Flesia 1999; Gentry 2000) was also designed to be used in a direct molecular lidar system to measure the wind velocities.

The double-edge technology uses two edge filters on the two shoulders of the Rayleigh scattering spectra, respectively. The wind velocity can be deduced when the photometric returns in two channels are known. The knowledge of the shape of the Rayleigh-Brillouin scattering is crucial to this technology. GroundWinds lidar systems are also direct lidar systems. Except for coherent Doppler lidar systems, all the lidar systems mentioned above use either the whole or part of the Rayleigh-Brillouin backscattering spectra in the atmosphere. Therefore, a better understanding of the Rayleigh-Brillouin scattering in the air is critical to many lidar measurements as well as air dynamics.



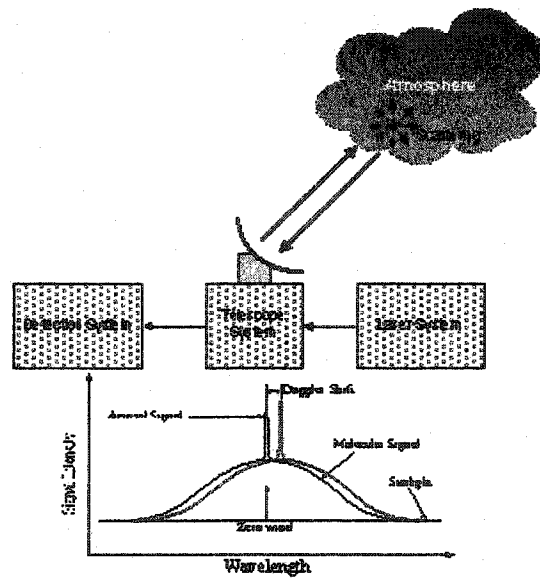


**Figure 1.8 Direct detection Doppler lidar.**

The GroundWinds lidar system is an incoherent lidar system. It makes use of a high spectral resolution Fabry-Perot interferometer capable of detecting Doppler shifts of the backscattered signal that correspond to velocities less than 1 m/s. It also employs a CCD detector, which has a high detection quantum efficiency, and a Circle to Line Interferometer Optical system (CLIO), which converts the circular fringes from the Fabry-Perot interferometer into a linear pattern.

The GroundWinds lidar system can be divided into three parts (see figure 1.8): laser system, telescope and detection system. A Nd:YAG laser is used as the probe source. The whole system works in the following way: The laser beam is transmitted to the air; the backscattered photons are gathered by the receiving telescope, then the photons guided through an optical system where the Fabry-Perot interferometer spreads

these photons into a circular pattern; and finally, the expected signal coming from the CLIO is recorded by the CCD detector. If there are few aerosols, the recorded signal on the CCD is actually the Rayleigh-Brillouin spectrum from which the Doppler shifts, hence the wind velocity, can be calculated. However, the aerosol density in the boundary layer is usually high, so a strong aerosol signal is commonly seen superposed on the Rayleigh-Brillouin line.

Two slightly different lidar systems are used in GroundWinds project. Their laser wavelengths are different. The GroundWinds lidar system at Bartlett, NH makes use of a frequency-doubled 532 nm Nd:YAG laser while the GroundWinds lidar system at Mauna Loa, HI makes use of a frequency-tripled Nd:YAG laser whose wavelength is 355nm. Since Brillouin scattering effects are more pronounced (Tenti 1974; Rye 1998) with a long wavelength laser, New Hampshire data were primarily used in the following data processing and related atmospheric researches:

Global wind measurements are of great importance in the study of meteorology and climate change (Atlas 1997; Baker 1998). The immediate, major benefit from wind measurements is the improvement of mid-term and long-term weather forecasts.

The GroundWinds lidar system was designed to measure the incoherent light backscattering spectrum in air. In real measurements, there are many factors that affect the line shape of the Rayleigh-Brillouin scattering. We need to know exactly how these factors will affect our measurements and if so, how much and in what way they will change the line shape. To be clear, we should divide these factors into two categories. The first category includes all the effects that caused by the light source—the

monochromatic laser beam. The second one includes all effects that caused by the atmospheric air, the probed gas medium.

**Table 1.1 Type of Factors affecting Rayleigh Scattering in Air**

Atmospheric cause	Instrument and laser atom interaction
Mixed air	Raman scattering
Turbulence broadening	Resonance fluorescence
Aerosol	Thermal blooming
	Instrument broadening
	Beam divergence and jitter

#### **1.4 Objective of Research**

The primary goal of this thesis is to study the Rayleigh-Brillouin scattering spectra in the air. This will be done through: the discrepancies between the mathematic model and real measurements and: the discrepancies between the measured temperature profiles by lidar and by radiosonde (balloon). We will use the measured RBS spectra to measure the temperature profile of the air and then evaluate the current mathematical models of RBS spectrum for diatomic molecules. From temperature profiling and variance analysis, wind turbulence can also be studied. A theoretical derivation of the change of the Rayleigh Brillouin scattering lineshape due to external forces or latent energy in the atmosphere will be presented for further analysis of RBS spectral data.

In addition, we can use the photometric returns at different altitudes from molecular channels to, for the first time, measure the molecular backscatter coefficients in air.

## 1.5 Preview

In chapter 2 we are going to review the molecular scattering power spectrum from the basic Maxwell equations. To solve for a theoretical molecular scattering spectrum expression in the kinetic regime, we need to first find the connection between the Boltzmann distribution function  $f(\mathbf{r}, \mathbf{v}, t)$  of the model equation – that is, from linearized Boltzmann or Boltzmann like equations – and the electric field of the incident light of the Maxwell equations. The density correlation function  $G(\mathbf{r}, t)$ , invented by Van Gove for studying neutron scattering, is an appropriate candidate which, in the kinetic regime, renders the backscattering power spectrum in the atmosphere capable of expressing a space-time Fourier transformation of the Boltzmann distribution function. We also show that the molecular scattering spectrum is proportional to the Fourier transformation of the instantaneous density fluctuations.

In chapter 3, the molecular scattering spectrum is solved using the Navier-Stokes equation and the energy conservation equation in the hydrodynamic regime and the linearized Boltzmann equation for diatomic gases in the kinetic regime, respectively; the relation between equations of the two models in the two different regimes is also discussed. We show that the resulting Rayleigh-Brillouin scattering spectrum for the kinetic regime is composed of two parts: polarized Rayleigh-Brillouin scattering and depolarized Rayleigh-Brillouin scattering, with the depolarized part contributing a small

portion of the total. Tenti's kinetic model is discussed afterwards; pointing out that the model only includes the polarized part of the Rayleigh-Brillouin scattering.

In chapter 4, data analysis is performed and temperature retrieved using the S6 model. The GroundWinds lidar system is first introduced; the main components and data acquisition method of the incoherent Doppler lidar system are discussed. The thermal blooming effect is analyzed afterwards. It is shown that thermal blooming is not an issue for the GroundWinds data products.

In chapter 5, Molecular backscatter coefficients for air are measured for the first time.

In chapter 6, the Rayleigh-Brillouin scattering spectrum of air molecules subject to external forces is investigated theoretically by solving the corresponding linearized Boltzmann equation. This general case could be applied to Rayleigh-Brillouin scattering with a strong acoustic field and to the retrieval of the turbulence information and other forms of latent energy in the air.

## CHAPTER 2

### RAYLEIGH-BRILLOUIN SCATTERING IN AIR

Rayleigh scattering spectra in dilute gases can be described with a Doppler shift and an assumed Maxwellian distribution of gas molecules (Loudon 2000). In this case the resulting Rayleigh line is a Gaussian, with a width determined by gas temperature. This model, however, is not rigorous because it ignores the specific gas properties, gas dynamics and molecular inner energy. Rayleigh scattering spectra should be understood from the perspective of gas dynamics (kinetics) and gas properties. For fluids and dense gases, Rayleigh scattering spectra can be computed from hydrodynamic equations, including the Navier-Stokes equation. The Rayleigh scattering spectra in the hydrodynamic regime were shown to be (Pecora 1964; Mountain 1966) the Fourier transform of density correlations. For dilute molecular gases (kinetic regime), hydrodynamic equations are not appropriate and in the kinetic regime, the kinetic Boltzmann equation should be employed to calculate the Rayleigh line shape.

Pecora (1964) showed that Rayleigh scattering spectrum, represented by  $S(k, \omega)$ , is the Fourier transform of the *density correlation function*  $G(r, t)$  which was proposed by Van Hove (1954). In the hydrodynamic regime, the density correlation function is represented as an ensemble average of density correlations with respect to space ( $r$ ) and time ( $t$ ).

It is more complicated to calculate the Rayleigh scattering spectra in the kinetic regime. The connection between the density correlation function  $G(r,t)$  and the phase space distribution  $f(r,v,t)$  in kinetic Boltzmann or Boltzmann-like equation is not obvious as it is in the hydrodynamic regime. Their relationship was finally established by Van Leeuwen (1965). Therefore we are able to calculate the Rayleigh scattering spectrum from the kinetic equations.

Although the connection between Rayleigh scattering spectra and the kinetic equation has been established, solving the kinetic Boltzmann or Boltzmann equation is still difficult or impossible. Therefore one must first linearize it by assuming the scattering gas medium is near equilibrium.

To better understand Rayleigh scattering in molecular gases, we examine the Rayleigh spectra from the perspective of the kinetic Boltzmann equation and the hydrodynamic model equations. We include the hydrodynamic approach because it is simpler yet informative. Because the unshifted Rayleigh line and Brillouin lines are well separated, the physics behind the scattering phenomenon can be easily understood.

## 2.1 Rayleigh Scattering Spectra

Before proceeding to derive the expression for Rayleigh scattering, we should consider light scattering by a homogeneous distribution of gas atoms where the incident light is assumed to be a monochromatic laser beam with frequency  $\omega$ . We further assumed the beam density is well defined and the beam does not suffer any absorptions or losses with laser atom interactions. If the atoms are uniformly distributed and the

distance between any two atoms is larger than the wavelength of the incident light, then the components of the scattered field within a half-wavelength will cancel the counterpart one wavelength away. Thus there will be no scattering incurred and the incident light will go straight through the gas without any losses; the gas itself is 100% transparent.

However, in a molecular gas, optical inhomogeneities arise from statistical fluctuations of some physical quantities (e.g., pressure and temperature). This leads to the fluctuations of the dielectric constant  $\epsilon$  of the gas. Light is thus scattered.

The studies of spectra of light scattering in gases, from one perspective, are extensions of the studies of spectra of light scattering in solid states and liquids. It became necessary to know the exact spectrum of rarefied gases for many applications to the atmosphere after the invention of laser technology. People (G. Fiocco 1971; Schwiesow R. 1981) assumed a Gaussian line shape, based on a Doppler shift and Maxwellian distribution of gas molecules, to describe the Rayleigh-Brillouin scattering spectrum. In the 1960's, Sidney Yip and his colleagues successfully proved that the *density correlation function*  $G(\mathbf{r}, t)$  (where  $\mathbf{r}$  is the position vector) as employed by Van Hove in 1954 to study neutron scattering, was related to the density distribution function  $f(\mathbf{r}, \mathbf{v}, t)$  in the linearized Boltzmann equation. The molecular scattering spectrum, represented by  $S(\mathbf{k}, \omega)$ , was shown to be the Fourier transform of  $G(\mathbf{r}, t)$  by Komarov and Pecora (1963, 1964).

$$S(\mathbf{k}, \omega) = 2 \operatorname{Re} \int_0^{\infty} dt \int d^3r \exp(i\mathbf{k} \cdot \mathbf{r} - \omega t) G(\mathbf{r}, t). \quad (2.1)$$



In the following section, we will present a derivation obtaining equation (2.1).

### 2.1.1 The Relations Between Spectrum of Light Scattering in Gases and $G(\mathbf{r}, t)$

We should consider the general case in which incident light is scattered by a group of neutral molecules. Assume that dielectric constant  $\epsilon$  is a function of the local density  $\rho$ , which itself is a function of position  $\mathbf{r}$  and time  $t$ , i.e.,  $\epsilon = \epsilon(\rho(\mathbf{r}, t))$ . We shall then, following Pecora (1963) and Komarov (1964), use perturbation method to solve the Maxwell equations.

For the total electric field in the scattering process,

$$\nabla \times \nabla \times \mathbf{E} = -(1/c^2)(\partial^2 \mathbf{D}/\partial t^2) \quad (2.2)$$

where, because there are no free charges

$$\nabla \cdot \mathbf{D} = 0. \quad (2.3)$$

Here  $\mathbf{E}$  is the sum of the incident light electric field  $\mathbf{E}_{inc}$  and the scattered electric field  $\mathbf{E}_{sc}$ ,  $\mathbf{E} = \mathbf{E}_{inc} + \mathbf{E}_{sc}$ ,  $\mathbf{D}$  is the Maxwell displacement vector,  $\mathbf{D} = \epsilon \mathbf{E}$ . Equations (2.2)

and (2.3) can be written as,

$$\nabla^2 \mathbf{E} - \nabla(\nabla \cdot \mathbf{E}) = \frac{1}{c^2} \cdot \frac{\partial^2 (\epsilon \mathbf{E})}{\partial t^2} \quad (2.4)$$

and

$$\nabla \cdot (\epsilon \mathbf{E}) = 0. \quad (2.5)$$

Expanding the electric field  $\mathbf{E}$  in terms of the incident light electric field  $\mathbf{E}_0$  and higher orders term and assuming  $|\mathbf{E}_{sc}| \ll |\mathbf{E}_0|$ :

$$\mathbf{E} = \mathbf{E}_0 + \mathbf{E}_1 + \mathbf{E}_2 + \dots \quad (2.6)$$

Here,  $\mathbf{E}_{inc} = \mathbf{E}_0$ ,  $\mathbf{E}_{sc} = \mathbf{E}_1 + \mathbf{E}_2 + \dots$ .

The dielectric constant  $\epsilon$  can be expanded in a Taylor series around the average gas density,  $\rho_0$

$$\epsilon(\rho) = \epsilon_0 + \epsilon_1 + \dots = \epsilon_0 + \left(\frac{\partial \epsilon}{\partial \rho}\right)_{\rho_0} (\rho - \rho_0) + \dots \quad (2.7)$$

Here we have assumed that the dielectric constant is a scalar, i.e., the tensor part of the instantaneous dielectric constant is much smaller than the diagonal terms.

Substituting the two expressions (2.6) and (2.7) into (2.4) and (2.5) and comparing terms of equal order of magnitude, we obtain a series of successive equations, one for each term in the expansion of the scattered field. The ones we are interested in are given below:

Zeroth order (the non-attenuated term): 
$$\nabla^2 \mathbf{E}_0 - \frac{\epsilon_0}{c^2} \frac{\partial^2 \mathbf{E}_0}{\partial t^2} = 0$$

(2.8)

First order (scattering with no damping):

$$\nabla^2 \mathbf{E}_1 - \frac{\epsilon_0}{c^2} \frac{\partial^2 \mathbf{E}_1}{\partial t^2} = \frac{1}{c^2} \frac{\partial^2 (\epsilon_1 \mathbf{E}_0)}{\partial t^2} - \frac{\nabla(\nabla \cdot \epsilon_1 \mathbf{E}_0)}{\epsilon_0} \quad (2.9)$$

Second order:

$$\nabla^2 \mathbf{E}_2 - \frac{\epsilon_0}{c^2} \frac{\partial^2 \mathbf{E}_2}{\partial t^2} = \frac{1}{c^2} \frac{\partial^2 (\epsilon_1 \mathbf{E}_1 + \epsilon_2 \mathbf{E}_0)}{\partial t^2} - \frac{\nabla(\nabla \cdot (\epsilon_1 \mathbf{E}_1 + \epsilon_2 \mathbf{E}_0))}{\epsilon_0} \quad (2.10)$$

Equation (2.10) is a standard non-damping electromagnetic wave equation. Equation (2.9) is the first order scattered field vector due to first order density fluctuations or single scattering process. We only consider the zero-order and the first-order equations. The expression for  $\mathbf{E}$  becomes,

$$\mathbf{E}_{inc} = \mathbf{E}_0, \quad \mathbf{E}_{sc} = \mathbf{E}_1.$$

The solution to the equation (2.8) is a plane wave propagating on the direction  $\mathbf{k}_i$ :

$$\mathbf{E}_{inc} = \mathbf{E}_0 \exp(i \mathbf{k}_i \cdot \mathbf{r} - i \omega_i t) \quad (2.11)$$

with

$$|\mathbf{k}_i| = \sqrt{\epsilon_0} \omega_i / c.$$

Here  $\mathbf{k}_i$  is the propagation vector of the incident light wave,  $\omega_i$  is its angular frequency, and  $c$  is the velocity of light in vacuum.

To solve equation (2.9), it is easier if we use a Fourier transform representation of  $\mathbf{E}_{sc}$ , i.e.,

$$\mathbf{E}_{sc}(\mathbf{r}, t) = \iint dt d\mathbf{r}^3 \mathbf{E}_{sc}(\mathbf{k}_f, \omega_f) \exp(-i \omega_f t) \exp(-i \mathbf{k}_f \cdot \mathbf{r}) \quad (2.12)$$

Where  $\mathbf{k}_f$  and  $\omega_f$  are the wave vector and angular frequency of scattered wave, respectively. Substituting into (2.11) and (2.12) into (2.9), and rearranging and we obtain,

$$\mathbf{E}_{sc}(\mathbf{k}, \omega_f) = -\frac{\mathbf{E}_0 \sin \psi}{R 8\pi^2 c^2} \exp(i\mathbf{k}_f \cdot \mathbf{R}) \int_{-\infty}^{\infty} dt \exp(i\omega_f t) \int d\mathbf{r}^3 \exp(i\mathbf{k} \cdot \mathbf{r}) \frac{\partial^2}{\partial t^2} [\epsilon_1(\mathbf{r}, t) \exp(-i\omega_f t)] \quad (2.13)$$

With

$$\mathbf{k} = \mathbf{k}_i - \mathbf{k}_f \quad \text{and} \quad |\mathbf{k}_i| = |\mathbf{k}_f|$$

Here  $\psi$  is the angle between two propagating vectors  $\mathbf{k}_i$  and  $\mathbf{k}_f$ . With the expression for the scattered field, the spectral density can be written as:

$$I(\mathbf{k}, \omega_f) = \frac{1}{2\pi} \int \langle \mathbf{E}_{sc}(\mathbf{k}, t') \cdot \mathbf{E}_{sc}^*(\mathbf{k}, t'+t) \rangle \exp(i\omega t) dt \quad (2.14)$$

or equivalently

$$I(\mathbf{k}, \omega_f) = \frac{1}{2\pi T} \int_{-T}^T dt \int_{-T}^T d\tau \mathbf{E}^*(\mathbf{k}, t) \mathbf{E}(\mathbf{k}, \tau) \exp[i\omega_f(t - \tau)] = \frac{|\mathbf{E}(\mathbf{k}, \omega_f)|^2}{T}$$

Here  $T$  denotes a time period of integration and is assumed to be much greater than the coherence time of the scattered light.

The angular brackets in the above expression denote a correlation of two field vectors at different time, which is an ensemble average of the electric field. As we stated earlier, the whole system we consider here is close to equilibrium. The Ergodic theory in the statistical mechanics implies,

$$\langle \mathbf{E}_{sc}(\mathbf{k}, t') \cdot \mathbf{E}_{sc}^*(\mathbf{k}, t + t') \rangle = \langle \mathbf{E}_{sc}(\mathbf{k}, 0) \cdot \mathbf{E}_{sc}^*(\mathbf{k}, t) \rangle \quad (2.15)$$

Using equations (2.13), (2.14) and (2.15), we obtained the scattered power spectrum

$$I(\mathbf{k}, \omega_f) = \frac{|\mathbf{E}_0|^2 \sin^2 \psi}{R^2 32\pi^3 c^4} \int_{-\infty}^{\infty} dt \exp(i\omega_f t) \times \int d^3 r' \int d^3 r'' \exp(i\mathbf{k} \cdot (\mathbf{r}' - \mathbf{r}'')) \times \left\langle \frac{\partial^4}{\partial t^4} \varepsilon_1(\mathbf{r}', 0) \varepsilon_1(\mathbf{r}'', t) \exp(-i\omega_f t) \right\rangle \quad (2.16)$$

The number density may be written as a summation of Dirac delta functions

$$\rho(\mathbf{r}, t) = \sum_{j=1}^N \delta[\mathbf{r} - \mathbf{r}_j(t)] \quad (2.17)$$

where  $\mathbf{r}_j(t)$  is the position of the  $j^{\text{th}}$  molecule at time  $t$ , and the sum is taken over all molecules in the system.

Replacing  $\rho(\mathbf{r}, t)$  in equation (2.7) by the expression (2.17)

$$\varepsilon_1(\mathbf{r}^n, t) = \left( \frac{\partial \varepsilon}{\partial \rho} \right)_{\rho=\rho_0} \left\{ \sum_j \delta[\mathbf{r}^n - \mathbf{r}_j(t)] - \rho_0 \right\} \quad (2.18)$$

Substituting (2.18) into (2.16), we get

$$I(\mathbf{k}, \omega_f) = \frac{|\mathbf{E}_0|^2}{R^2} \left( \frac{\partial \varepsilon}{\partial \rho} \right)_{\rho=\rho_0}^2 \frac{\sin^2 \psi}{32\pi^3 c^4} \int_{-\infty}^{\infty} dt \exp(i\omega_f t) \frac{\partial^4}{\partial t^4} \times \left\{ \left\langle \sum_j^N \sum_l^N \exp[-i\mathbf{k} \cdot (\mathbf{r}_j(0) - \mathbf{r}_l(t))] - (2\pi)^3 \delta(\mathbf{k}) \rho_0^2 V \right\rangle \exp(-i\omega_0 t) \right\} \quad (2.19)$$

The density correlation function proposed by Van Hove (1954) is

$$G(\mathbf{r}, t) = \left( \frac{1}{2\pi} \right)^3 \frac{1}{N} \int \left\langle \sum_j \sum_l \exp\{-i\mathbf{k} \cdot [\mathbf{r}_j(0) - \mathbf{r}_l(t)]\} \right\rangle \exp(-i\mathbf{k} \cdot \mathbf{r}) d^3 k \quad (2.20)$$

where  $N$  is the number of total scattering particles. The angular brackets  $\langle \dots \rangle$  indicate an ensemble average over the initial states of the system. Generally  $G(\mathbf{r}, t)$  is complex and has no simple physical meaning (Van Hove, 1958). However, when considered in classical terms, it gives the probability per unit volume of finding an atom resides at position  $\mathbf{r}$  and time  $t$  provided an atom at the origin at  $t = 0$ . These two atoms cannot be

the same one. We will discuss more about  $G(\mathbf{r}, t)$  in the following sections of this chapter.

The inverse Fourier transform representation of  $G(\mathbf{r}, t)$  is:

$$F(\mathbf{k}, t) = \langle \sum_j \sum_l \exp\{-i\mathbf{k} \cdot [\mathbf{r}_j(0) - \mathbf{r}_l(t)]\} \rangle = N \int G(\mathbf{r}, t) \exp(i\mathbf{k} \cdot \mathbf{r}) d^3r. \quad (2.21)$$

Rewriting equation (2.19) by making use of the expression (2.21), we obtain

$$I(\mathbf{k}, \omega_f) = \frac{|\mathbf{E}_0|^2}{R^2} \left( \frac{\partial \epsilon}{\partial \rho} \right)_{\rho=\rho_0}^2 \frac{\sin^2 \psi}{32\pi^3 c^4} \int_{-\infty}^{\infty} dt \exp(i\omega_f t) \\ \times \int d^3r \exp(i\mathbf{k} \cdot \mathbf{r}) \frac{\partial^4}{\partial t^4} \{NG(\mathbf{r}, t) - \rho_0^2 V\} \exp(-i\omega_f t) \quad (2.22)$$

In most cases the  $G(\mathbf{r}, t)$  function will vary slowly compared to the frequency of the incident electromagnetic wave ( $10^{14} \sim 10^{15}$  Hz). Therefore we can treat the density correlation function  $G(\mathbf{r}, t)$  as a constant and remove it from the time derivative

$$\frac{\partial^4}{\partial t^4} \{NG(\mathbf{r}, t) - \rho_0^2 V\} \exp(-i\omega_f t) \approx [NG(\mathbf{r}, t) - \rho_0^2 V] \frac{\partial^4}{\partial t^4} \{\exp(-i\omega_f t)\} \quad (2.23)$$

Using this approximation and knowing that  $N = \rho_0 V$ , we obtain the spectral density

$$I(\mathbf{k}, \omega_f - \omega_i) = \frac{|\mathbf{E}_0|^2}{R^2} \left( \frac{\partial \epsilon}{\partial \rho} \right)_{\rho=\rho_0}^2 \frac{\sin^2 \psi}{32\pi^3 c^4} \omega_i^4 N \iint [G(\mathbf{r}, t) - \rho_0] \exp\{i\mathbf{k} \cdot \mathbf{r} - i(\omega_i - \omega_f)t\} d^3 r dt \quad (2.24)$$

This equation shows that the scattering spectrum is simply the space-time Fourier transform of the density correlation  $G(\mathbf{r}, t)$ .

### 2.1.2 The Van Hove Space-Time Density Correlation Function $G(\mathbf{r}, t)$

The density correlation function, proposed by Van Hove (1954), was defined by expression (2.19). With the help of the convolution formulae for the Fourier transform, we obtain an equivalent form of equation (2.19):

$$G(\mathbf{r}, t) = N^{-1} \left\langle \sum_{j,l} \int d\mathbf{r}' \delta(\mathbf{r} + \mathbf{r}_j(0) - \mathbf{r}') \delta(\mathbf{r}' - \mathbf{r}_l(t)) \right\rangle. \quad (2.25)$$

$\langle \dots \rangle$  stands for ensemble average of the initial state. For long times and large  $r$ , the density correlation function  $G(\mathbf{r}, t)$  reduces to the autocorrelated density

$$G(\mathbf{r}, t) = N^{-1} \int d\mathbf{r}' \langle \rho(\mathbf{r}' - \mathbf{r}, 0) \rho(\mathbf{r}', t) \rangle \quad (2.26)$$



Since the spectra density of the light scattering in gases is just a Fourier transform of  $G(\mathbf{r}, t)$ , we can obtain the power spectrum  $S(\mathbf{k}, \omega)$  using equation (2.26).

$$S(\mathbf{k}, \omega) \propto I(\mathbf{k}, \omega) \propto \langle \rho(\mathbf{k}, 0) \rho(\mathbf{k}, \omega) \rangle = \langle \rho^*(\mathbf{k}, \omega) \rho(\mathbf{k}, \omega) \rangle \quad (2.27)$$

However, since we have assumed long times and large  $r$  (or large collision frequency) in the derivation of (2.26), the power spectrum representation in (2.27) can only be used in the hydrodynamic regime in which the gas medium must be dense. This implies that the collision time of the gas molecules must be much less than the light pulse and the mean free path must be much shorter than the incident light wavelength.

In the kinetic regime, the light wavelength is comparable to the mean free path of the gas molecules; thus the expression (2.27) cannot be used in general. Sidney et al. (1964) solved this problem by successfully linking the density correlation function  $G(\mathbf{r}, t)$  with the linearized Boltzmann-like equations. Therefore if we can solve the related linearized Boltzmann-like equations, we can obtain  $G(\mathbf{r}, t)$  hence the spectrum of light scattering  $S(\mathbf{k}, \omega)$  (ref. Equation 2.24), in which the information about the density fluctuations is contained.

In a rarefied gas such as air, where the system deviates only slightly from equilibrium, it can be described by a kinetic equation such as Boltzmann equation. To explain the connection between  $G(\mathbf{r}, t)$  and the linearized Boltzmann-like equations, we use a simplified kinetic equation proposed by Bhatnagar, Gross and Krook (1954) to describe a monatomic dilute gas. The equation satisfies mass, energy and momentum conservation as well as the Boltzmann H theorem, which states that the total entropy of a

closed system increases with time. The kinetic equation BGK used to treat the monatomic neutral gas is (Bhatnagar 1954):

$$\left(\frac{\partial}{\partial t} + \mathbf{v} \cdot \nabla\right) h(\mathbf{r}, \mathbf{v}, t) = \alpha \left\{ \rho(\mathbf{r}, t) - h(\mathbf{r}, \mathbf{v}, t) + \left[ \frac{2}{v_0^2} \mathbf{v} \cdot \mathbf{q}(\mathbf{r}, t) + \left( \frac{v^2}{v_0^2} - \frac{3}{2} \right) \frac{\tau(\mathbf{r}, t)}{T_0} \right] \right\},$$

(2.28)

where  $h(\mathbf{r}, \mathbf{v}, t)$  is the distribution of density fluctuation from  $\rho_0$ . Others are defined as follows:

$$f_0(v) = (\pi v_0^2)^{-3/2} \exp(-v^2 / v_0^2),$$

$$v_0 = \sqrt{\frac{2k_B T_0}{M}},$$

$$\mathbf{q}(\mathbf{r}, t) = \int d^3 v \mathbf{v} h(\mathbf{r}, \mathbf{v}, t), \quad (2.29)$$

$$\rho(\mathbf{r}, t) = \int d^3 v h(\mathbf{r}, \mathbf{v}, t),$$

$$T_0^{-1} \tau(\mathbf{r}, t) = \frac{1}{3v_0^2} \int d^3 v v^2 h(\mathbf{r}, \mathbf{v}, t) - Z(\mathbf{r}, t)$$

where  $M$  is the atomic mass,  $k_B$  is the Boltzmann constant,  $T_0$  is the equilibrium temperature of the gas, and  $\tau$  is the deviation of the temperature  $T$ ,  $\tau = T/T_0 - 1$ .  $\alpha$  is uniform collision frequency. We consider one particle sitting at the origin at  $t = 0$ , i.e.

$$h(\mathbf{r}, \mathbf{v}, 0) = \delta(\mathbf{r}). \quad (2.30)$$

Now, bearing in mind that  $G(\mathbf{r}, t)$  is the density correlation function describes relationship between one particle at origin and another particle was found at  $\mathbf{r}$  after a specific time gap  $t$ . Now we assert

$$G(\mathbf{r}, t) = (\rho(\mathbf{r}, t) + 1)\rho_0 = \left( \int d^3v h(\mathbf{r}, \mathbf{v}, t) + 1 \right) \rho_0 \quad (2.31)$$

since the two quantities have the same physical meaning. So we can solve the groups of equations (2.28), (2.29), (2.30) and (2.31) for the expected  $G(\mathbf{r}, t)$ .

From equations (2.24), (2.27) and (2.31), one can easily tell that the power spectrum  $S(\mathbf{k}, \omega)$ , in the kinetic regime, is proportional to the Fourier transform of the instantaneous change of the gas densities. It seems the scattering spectra from the kinetic Boltzmann equation is different from the power spectrum—we got in equation (2.27)—in which  $S(\mathbf{k}, \omega)$  is proportional to the square of the Fourier transform of the instantaneous change of gas density, for the hydrodynamic instances. However, it is not true; the ensemble average of the initial state will average out one  $\delta\rho(\mathbf{k}, \omega)$ , the scattering spectrum in the hydrodynamic regime is still proportional to  $\delta\rho(\mathbf{k}, \omega)$ , Fourier transform of the instantaneous change of the gas density.

## CHAPTER 3

### MODELING OF RAYLEIGH-BRILLOUIN SCATTERING SPECTRUM

#### 3.1 Hydrodynamics Approach – Rayleigh-Brillouin Scattering

In last section we derived an expression for the spectrum of light scattering in gases. Rayleigh-Brillouin scattering spectrum in the gases can be divided into two categories: 1) when light is scattered by the dilute gases, i.e., in the kinetic regime, a linearized Boltzmann or Boltzmann-like equation should be used to calculate the spectrum; 2) when light was scattered by the dense gas, the model equations for the Rayleigh-Brillouin scattering spectra are a group of hydrodynamic equations; although the kinetic Boltzmann equation can still be used in this regime, the hydrodynamic equations provide a simpler picture of the physics in Rayleigh-Brillouin scattering. It is therefore a better choice for us to discuss Rayleigh-Brillouin scattering in the hydrodynamic regime first before we have to deal with the more sophisticated kinetic equations in the kinetic regime.

From Chapter 2, we learned that the scattered density spectra is a function of the dielectric constant, i.e.,

$$I_{sc} = I_{sc}(\varepsilon) . \quad (3.1)$$

In order to calculate the scattering spectrum, we need to evaluate the instantaneous dielectric constant. We take the density  $\rho$  and temperature  $T$  as the independent thermodynamic variables and express the instantaneous change of the dielectric constant as

$$\Delta\varepsilon = \left(\frac{\partial\varepsilon}{\partial\rho}\right)_T \Delta\rho + \left(\frac{\partial\varepsilon}{\partial T}\right)_\rho T \quad (3.2)$$

Fabelinskii (1968) estimated that the dielectric constant typically depends much more strongly on density than on temperature (less than 2%); therefore we can use the following expression:

$$\Delta\varepsilon = \left(\frac{\partial\varepsilon}{\partial\rho}\right) \Delta\rho. \quad (3.3)$$

Now the problem has changed to evaluate the instantaneous change of density. We choose the entropy  $S$  and pressure  $P$  as our independent thermodynamic variables. We then have,

$$\Delta\rho = \left(\frac{\partial\rho}{\partial P}\right)_S \Delta P + \left(\frac{\partial\rho}{\partial S}\right)_P \Delta S. \quad (3.4)$$

The first term on the right hand side describes adiabatic density fluctuations, that is, undamped acoustic wave that produce Brillouin scattering. The last term on the right

hand side describes isobaric density fluctuations (entropy fluctuations) and accounts for unshifted Gross line. We will see that these two parts lead to different spectral distributions of the scattered light because the equations of motion for pressure and entropy are different: for  $\Delta P$ , the equation of motion is a damped acoustic wave equation; for  $\Delta S$ , the corresponding equation of motion is a diffusion equation. A Rayleigh-Brillouin spectrum in the hydrodynamic regime is shown in Figure 3.2.

If the incident light electric field represented by  $\mathbf{E}_0(\mathbf{r}, t)$  and the scattered light electric field is  $\mathbf{E}_{sc}(\mathbf{r}, t)$ , we set

$$\mathbf{E}_{sc} \equiv \mathbf{E}_0 \phi(\mathbf{r}, t) \quad (3.5)$$

From section 2.1 we know that  $\phi(t)$  has the following properties:

$$\phi(\mathbf{r}, t) \propto \Delta \varepsilon \propto \Delta P(\mathbf{r}, t) \quad (3.6)$$

Then the Stokes equation of motion for a pressure wave propagating in liquids is shown to be (Fabelinskii 1997)

$$\frac{\partial^2 \phi}{\partial t^2} - \Gamma \nabla^2 \frac{\partial \phi}{\partial t} - v_s^2 \nabla^2 \phi = 0 \quad (3.7)$$

or

$$\frac{\partial^2 \Delta P}{\partial t^2} - \Gamma \nabla^2 \frac{\partial(\Delta P)}{\partial t} - v_s^2 \nabla^2 (\Delta P) = 0 \quad (3.8)$$

by making use of the expression (3.6). Here  $\Gamma$  is the acoustic wave damping constant.  $v_s$  denotes the velocity of sounds, which is

$$v_s^2 = \left( \frac{\partial P}{\partial \rho} \right)_s = \frac{\gamma P}{\rho} \quad (3.9)$$

for ideal gases.

To solve a wave equation like equation (3.7), a common used method is to set

$$\phi = \phi_0 \exp(i\mathbf{q} \cdot \mathbf{r} - \Omega t) + \text{c.c.} \quad (3.9)$$

For convenience, we assume the scattered wave is propagating along the z-axis,

$$\phi = \phi_0 \exp(iqz - \Omega t) + \text{c.c.} \quad (3.10)$$

Substituting (3.10) into (3.7), we get a dispersion relation for  $\Omega$ ,

$$\Omega^2 = q^2 (v_s^2 - i\Omega\Gamma) \quad (3.11)$$

The solution to equation (3.7) is of the form

$$\phi(z, t) = \sum_q \exp(iqz) \psi(t) \quad (3.12a)$$

with

$$\psi(t) \equiv \psi(0) \exp\left(-\frac{\Gamma q^2}{2} t\right) \cos \Omega t \quad (3.12b)$$

The power spectrum related to (3.12) is

$$I(\omega) \propto E_0^2 \int_0^{\infty} \langle \psi(0) \psi(t) \rangle \exp(-i\omega t) dt = E_0^2 \langle |\psi(0)|^2 \rangle \frac{\Omega^2 q^2 \Gamma}{(\omega^2 - \Omega^2)^2 + \Gamma^2 q^4 \omega^2} \quad (3.13)$$

If  $\Gamma q^2 \ll \Omega$  then

$$I(\omega) \propto A \cdot \frac{1}{\pi} \frac{\Gamma q^2 / 2}{(\omega - \Omega)^2 + \Gamma^2 q^4 / 4} \quad (3.14)$$

From (3.11)  $\Omega = qv_s$ . This is a shifted Lorentzian distribution with a width equals to  $\Gamma q^2$ . This is the Stokes part of the Brillouin scattering.

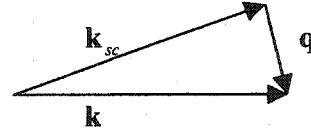


Figure 3.1 Relationship between  $\mathbf{q}$ ,  $\mathbf{k}$  and  $\mathbf{k}_{sc}$

If the incident light wave vector and frequency are  $\mathbf{k}$  and  $\omega$ , the scattered light wave field wave vector is  $\mathbf{k}_{sc}$ , they are differed by the vector  $\mathbf{q}$  because the light photons were scattered by the propagating pressure wave (see figure 3.1). So we have

$$\mathbf{q} = \mathbf{k} - \mathbf{k}_{sc}, \quad |\mathbf{k}| = |\mathbf{k}_{sc}| = \frac{n\omega}{c} \quad (3.15)$$



$n$  is the refractive index. Since  $\Omega = qv_s$ , and  $\mathbf{q}$  has to satisfy

$$q = 2|\mathbf{k}| \sin\left(\frac{\theta}{2}\right) \quad (3.16)$$

according to the geometry and configuration in figure 3.3. Combining (3.11), (3.15) and (3.16), we obtain

$$\Omega = 2n\omega \frac{v_s}{c} \sin\left(\frac{\theta}{2}\right) \quad (3.17)$$

As we have shown in (3.14), due to the attenuation of the acoustic wave, the scattered light is not monochromatic but has a spread power spectrum.

The equation of motion for the entropy fluctuations are described by a diffusion equation, which is,

$$\rho c_p \frac{\partial S}{\partial t} - \kappa \nabla^2 S = 0. \quad (3.18)$$

Here  $c_p$  is the specific heat at constant pressure for the gas,  $\kappa$  is the thermal conductivity. It is easy to solve this equation. A solution is

$$S = S_0 + S(0) \exp\left(-\frac{\kappa q^2}{\rho c_p} t\right) \exp(i\mathbf{q} \cdot \mathbf{r}), \quad (3.19)$$

where  $S_0$  is the average entropy.

The corresponding spectrum is simply the Fourier transform of (3.19)

$$I(\omega) = I_s \frac{\kappa q^2 / \rho c_p}{\omega^2 + (\kappa q^2 / \rho c_p)^2}. \quad (3.20)$$

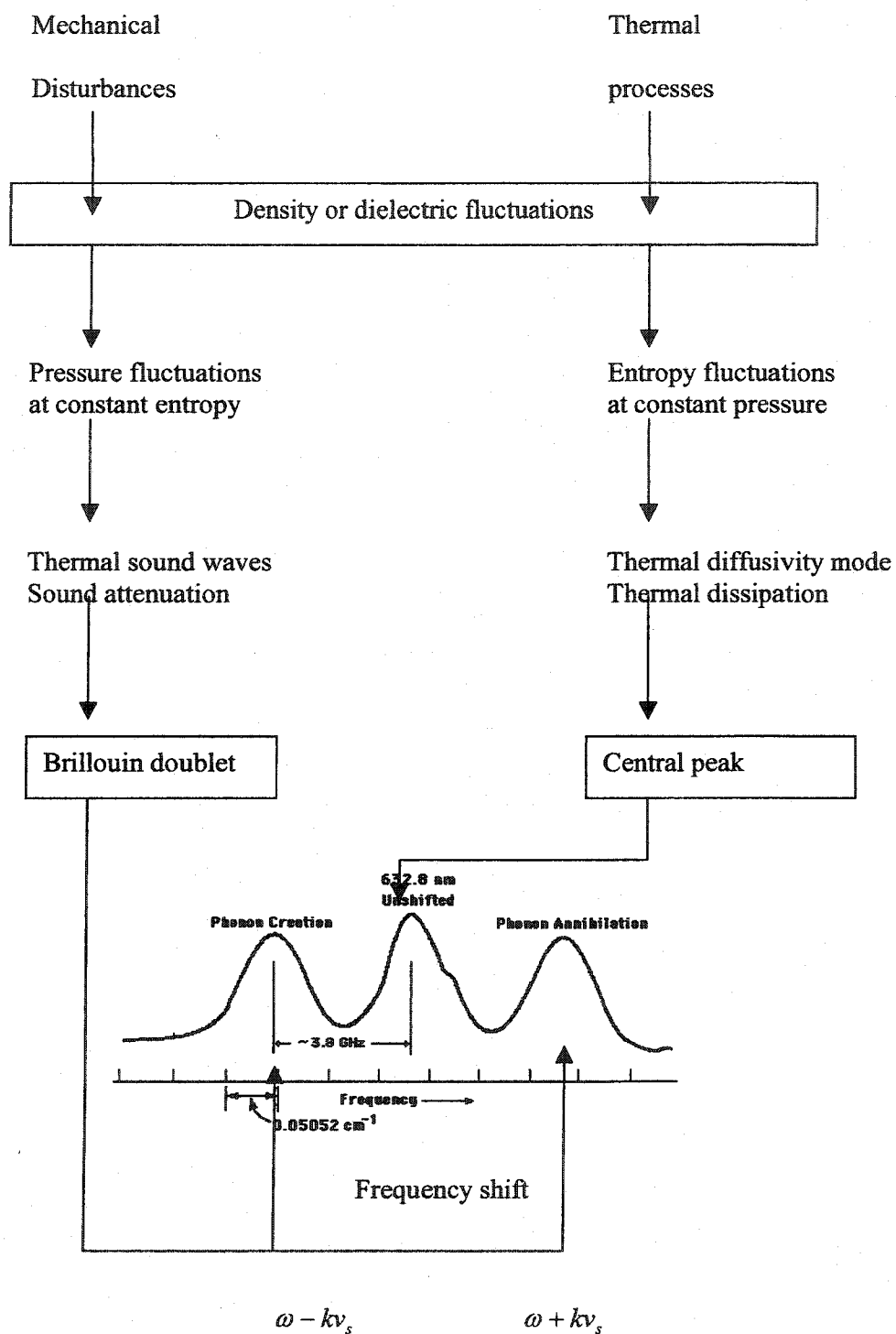


Figure 3.2 Representation of molecular light scattering spectrum.

It is also a Lorentzian distribution but it is not shifted. This forms the Rayleigh central line.

We have known so far that the Rayleigh-Brillouin scattering in dense gases or liquids is due to entropy fluctuations that account for the unshifted Rayleigh line (also Gross line). Pressure fluctuations (i.e., acoustic wave) account for the Brillouin side bands. We now switch to a more rigorous and general theoretical model that can be applied on spontaneous Rayleigh-Brillouin scattering and stimulated Rayleigh-Brillouin scattering. We will only develop a theoretical model for spontaneous Rayleigh-Brillouin scattering here because it is our interest. However, this model can be easily extended into one for the stimulated Rayleigh-Brillouin scattering.

This model is based on three hydrodynamic equations. They are the equation of mass, momentum, and energy conservation, respectively:

$$\frac{\partial}{\partial t} \rho + \rho \nabla \cdot \mathbf{u} + \mathbf{u} \cdot \nabla \rho = 0 \quad (3.21a)$$

$$\rho \frac{\partial \mathbf{u}}{\partial t} + \rho (\mathbf{u} \cdot \nabla) \mathbf{u} = -\nabla P + \left( \frac{4}{3} \eta + \xi_s \right) \nabla (\nabla \cdot \mathbf{u}) - \eta_s \nabla \times (\nabla \times \mathbf{u}) \quad (3.21b)$$

$$\rho C_v \frac{\partial T}{\partial t} + \rho C_v (\bar{u} \cdot \nabla T) + \rho C_v \left( \frac{\gamma - 1}{\beta} \right) (\nabla \cdot \mathbf{u}) = \kappa \nabla^2 T. \quad (3.21c)$$

Here  $\eta_s$  is the shear viscosity,  $\xi$  is the bulk viscosity and  $\beta = -\frac{1}{\rho} \left( \frac{\partial \rho}{\partial T} \right)_P$  is the thermal expansion coefficient. No damping of wave energy was assumed in equation (3.21). As we can see, there are four unknowns in the three equations:  $\rho$ ,  $T$ ,  $P$  and  $\mathbf{u}$ . Taking the pressure as a function of density and temperature, we have,

$$P = \left(\frac{\partial P}{\partial \rho}\right)_T \rho + \left(\frac{\partial P}{\partial T}\right)_\rho T. \quad (3.22)$$

From statistical mechanics, we know

$$\left(\frac{\partial P}{\partial \rho}\right)_T = \frac{1}{\gamma} \left(\frac{\partial P}{\partial \rho}\right)_S = \frac{1}{\gamma} v_s^2 \quad (3.23)$$

and

$$\left(\frac{\partial P}{\partial T}\right)_\rho = \frac{1}{\gamma} \left(\frac{\partial P}{\partial \rho}\right)_S \left(\frac{\partial \rho}{\partial T}\right)_P = \frac{\beta}{\gamma} v_s^2 \rho_0. \quad (3.24)$$

Substituting into (3.22), we obtain an expression for the pressure  $P$  in terms of  $\rho$ ,  $T$ ,

$$P = \frac{v_s^2}{\gamma} (\rho + \beta \rho_0 T) \quad (3.25)$$

The fundamental idea to solve equations (3.21) is to assume small density perturbation.

The three equations can then be linearized. We take

$$\rho = \rho_0 + \rho_1 \quad \rho_1 \ll \rho_0 \quad (3.26a)$$

$$T = T_0 + T_1 \quad T_1 \ll T_0 \quad (3.26b)$$

$$P = P_0 + P_1 \quad P_1 \ll P_0. \quad (3.26c)$$

Each symbol with subscript zero represents the local average of the thermodynamic variable it stands for. They are all constants. Thus equation (3.25) can be rewritten as

$$P_1 = \frac{v_s^2}{\gamma}(\rho_1 + \beta\rho_0 T_1) \quad (3.27)$$

Substituting equations (3.26) and (3.27) into the three hydrodynamic equations (3.21), we obtain a group of linearized mass, momentum and energy conservation equations:

$$\frac{\partial \rho_1}{\partial t} + \rho_0 \nabla \cdot \mathbf{u} = 0 \quad (3.28a)$$

$$\rho_0 \frac{\partial \mathbf{u}}{\partial t} + \frac{v_s^2}{\gamma} \nabla \rho_1 + \frac{\rho_0 \beta v_s^2}{\gamma} \nabla T_1 - \left( \frac{4}{3} \eta_s + \xi \right) \nabla (\nabla \cdot \mathbf{u}) = 0 \quad (3.28b)$$

$$\rho_0 c_v \frac{\partial T_1}{\partial t} + \rho_0 \frac{c_v (\gamma - 1)}{\beta} (\nabla \cdot \mathbf{u}) - \kappa \nabla^2 T_1 = 0 \quad (3.28c)$$

Bearing in mind that we are pursuing an expression of density, i.e., the solution of  $\rho_1$ . To do this, we need first to eliminate variable  $\mathbf{u}$  by taking the divergence of equation (3.28b) then substitute (3.28a) to (3.28b) and (3.29c) to get two equations for  $\rho_1$  and  $T_1$ . We get

$$\frac{\partial^2 \rho_1}{\partial t^2} - \frac{v_s^2}{\gamma} \nabla^2 \rho_1 - \frac{\rho_0 \beta v_s^2}{\gamma} \nabla^2 T_1 - \frac{\left( \frac{4}{3} \eta_s + \xi \right)}{\rho_0} \nabla^2 \left( \frac{\partial \rho_1}{\partial t} \right) = 0 \quad (3.29a)$$

$$\rho_0 c_v \frac{\partial}{\partial t} T_1 - \kappa \nabla^2 T_1 - \frac{c_v (\gamma - 1)}{\beta} \frac{\partial \rho_1}{\partial t} = 0 \quad (3.29b)$$

We notice that equation (3.29a) is a damped wave equation for density variation  $\rho_1$  with a coupled term of temperature  $T_1$ , while equation (3.29b) is a diffusion equation of temperature (entropy)  $T_1$  with a coupled term of density  $\rho_1$ . The difference between equations (3.29a,b) and equations (3.8), (3.18) is that the two equations of (3.29) have additional coupled terms.

Some properties, *e.g.* dispersion relations, can be estimated by assuming both  $\rho_1$  and  $T_1$  have a plane wave description. Nonetheless, to obtain an explicit solution of  $\rho_1$ , we must include the initial conditions. A common but effective method is to apply the Fourier-Laplace transform on the two unknown variables, *i.e.*,

$$\rho(\mathbf{k},s) = \int d\mathbf{r} \int_0^\infty dt \exp(-i\mathbf{k}\cdot\mathbf{r}) \exp(-st) \rho_1(\mathbf{r},t) \quad (3.30a)$$

$$T(\mathbf{k},s) = \int d\mathbf{r} \int_0^\infty dt \exp(-i\mathbf{k}\cdot\mathbf{r}) \exp(-st) T_1(\mathbf{r},t) \quad (3.30b)$$

Substituting (3.30) into (3.29), we obtain

$$\begin{aligned} \left[ s^2 + \frac{v_s^2 k^2}{\gamma} + \frac{(4/3\eta_s + \xi)k^2 s}{\rho_0} \right] \rho(\mathbf{k},s) + \left[ \frac{v_s^2 \beta \rho_0 k^2}{\gamma} \right] T(\mathbf{k},s) = \rho(\mathbf{k},0) \left[ s + \frac{(4/3\eta_s + \xi)k^2 s}{\rho_0} \right] \\ - \left[ \frac{c_v(\gamma-1)s}{\beta} \right] \rho(\mathbf{k},s) + [\rho_0 c_v s + \kappa k^2] T(\mathbf{k},s) = -\rho(\mathbf{k},0) \frac{c_v(\gamma-1)}{\beta} + \rho_0 c_v T(\mathbf{k},0) \end{aligned} \quad (3.31)$$

The solution to equation (3.31) for  $\rho(\mathbf{k},s)$  is

$$\rho(\mathbf{k},s) = \rho(\mathbf{k},0) \frac{s^2 + (a+b)k^2s + abk^4 + v_s^2[(\gamma-1)/\gamma]k^2}{s^3 + (a+b)k^2s^2 + (k^2v_s^2 + abk^4)s + ak^4v_s^2/\gamma} \quad (3.32)$$

The new symbols are

$$a = \frac{\kappa}{\rho_0 c_v}$$

and

$$b = \frac{4/3\eta_s + \xi}{\rho_0}$$

We have discarded one addition term of  $T(\mathbf{k},0)$  on the right hand side of (3.32) because we have been assuming that density and temperature are independent in the whole derivation. The derivation of the inverse Laplace transform of  $\rho(\mathbf{k},s)$  is tricky and lengthy (Mountain 1966). However, after some approximations being made during the inverse process, the result is:

$$\rho(\mathbf{k},t) = \rho(\mathbf{k},0) \left\{ \frac{\gamma-1}{\gamma} \exp\left(-\kappa \frac{k^2}{\rho_0 c_p} t\right) + \frac{1}{\gamma} \exp(-\Gamma k^2 t) \cos(v_s k t) \right\} \quad (3.33)$$

where

$$\Gamma = \frac{1}{2} \left( b + \frac{\gamma-1}{\gamma} a \right) = \frac{1}{2} \left[ \frac{4/3\eta_s + \xi}{\rho_0} + \frac{\gamma-1}{\gamma} \frac{\kappa}{\rho_0 c_v} \right] \quad (3.34)$$

is often called the acoustic attenuation coefficients. The spectrum, using the result in chapter 2, can be obtained as follows:

$$\begin{aligned}
 S(k, \omega) &= 2 \operatorname{Re} \int_0^{\infty} dt \exp(i\omega t) \langle \rho^*(\mathbf{k}, 0) \rho(\mathbf{k}, t) \rangle \\
 &= \langle \rho(-\mathbf{k}, 0) \rho(\mathbf{k}, 0) \rangle \left\{ \frac{\gamma - 1}{\gamma} \frac{k^2 / \rho_0 c_p}{\omega^2 + (k^2 / \rho_0 c_p)^2} + \frac{1}{\gamma} \left[ \frac{\Gamma k^2}{(\omega + kv_s)^2 + (\Gamma k^2)^2} + \frac{\Gamma k^2}{(\omega - kv_s)^2 + (\Gamma k^2)^2} \right] \right\} \\
 &\hspace{15em} \text{Doppler shift}
 \end{aligned}
 \tag{3.35}$$

It appears that the whole spectrum is composed of three Lorentzian distributions. The first term within the braces on the right hand side of expression (3.35) is identified as the Rayleigh line. The left two terms are the Brillouin doublet; the first one of the Brillouin terms is called anti-Stokes Brillouin scattering part and the second one is the Stokes part. The area under the unshifted Rayleigh line  $I_R$  and the area under the Brillouin sidebands  $I_B$  have a well-known relationship: the ratio of  $I_R$  and  $I_B$  is a constant, i.e.,

$$\frac{2I_B}{I_R} = \frac{1}{\gamma - 1}, \tag{3.36}$$

which is called Landau-Placzek ratio.



### 3.2 The Kinetic Approach of Rayleigh-Brillouin Scattering

For gases, when the gas density is not too dense, the Boltzmann equation turns out to be appropriate to describe the gas kinetics. However, there are several issues on the Boltzmann equation: First, the Boltzmann equation cannot be solved analytically; second, Boltzmann equation has its limitation because it assumes the gas cannot be too dense because only binary collisions between gas molecules are taken into account. Because of this, researchers have been using the linearized Boltzmann equation and other Boltzmann-like kinetic equations to describe Rayleigh-Brillouin scattering in gases.

We assume the gas is just a little off from the equilibrium state, so we can use the linearized Boltzmann equation in our application to the gas. The kinetic theory for the dilute gases is complicated so our approach below employs perturbation theory, as in quantum mechanics. We can easily see the many important properties of the linearized Boltzmann equation without even knowing the exact form of the collision operator.

#### 3.2.1 Linearized Boltzmann Equation

We first treat the case in which the gas is monatomic; therefore we don't need to include the internal effects of the molecules such as rotational effects. So the distribution function in the Boltzmann equation is just a function of time, position and velocity, i.e.,

$$f = f(t, \mathbf{v}, \mathbf{r}).$$

Generally, the linearized Boltzmann equation reads,

$$\frac{\partial f}{\partial t} + \mathbf{v} \cdot \nabla f + \mathbf{a} \cdot \nabla_{\mathbf{v}} f = \left. \frac{\delta f}{\delta t} \right|_{coll}$$

or explicitly

$$\frac{\partial f}{\partial t} + \mathbf{v} \cdot \nabla f + \mathbf{a} \cdot \nabla_{\mathbf{v}} f = n \iiint d^3 v_1 \int_0^{2\pi} d\Omega \int_0^{\pi} \sigma(\mathbf{v}, \theta) \mathbf{v}_{rel} \cdot \mathbf{f}^0(\mathbf{v}_1) [f(\mathbf{v}') + f(\mathbf{v}'_1) - f(\mathbf{v}) - f(\mathbf{v}_1)]$$

(3.37)

Here,  $\sigma(\mathbf{v}_{rel}, \theta)$  is the collision cross section.  $\mathbf{v}_{rel}$  is the relative velocity of the colliding particles:

$$\mathbf{v}_{rel} = \mathbf{v} - \mathbf{v}_1 \quad (3.38)$$

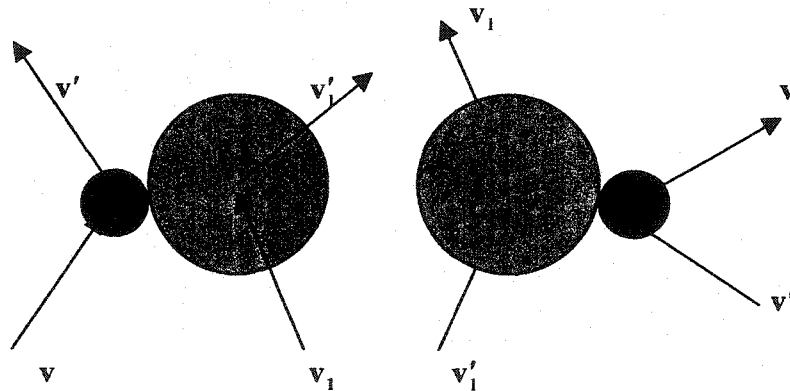


Figure 3.3 Two molecules/atoms colliding process

In the case where there is no external force, *i.e.*  $a_i = 0$ , we obtained from equation (3.37) the following equation,


$$\frac{\partial f}{\partial t} + \mathbf{v} \cdot \nabla f = n \iiint d^3 v_1 \int_0^{2\pi} d\Omega \int_0^\pi \sigma(\mathbf{v}, \theta) \mathbf{v}_{rel} \bullet f^0(\mathbf{v}_1) [f(\mathbf{v}') + f(\mathbf{v}'_1) - f(\mathbf{v}) - f(\mathbf{v}_1)] \equiv Kf \quad (3.39)$$

The right hand side of this equation defines a linear integro-differential operator  $K$ .  $K$  is usually called the *linearized collision operator*.

### 3.2.2 Homogeneous Case

For the sake of simplicity, we first assume  $f = f(\mathbf{v}, t)$ ; it is independent of  $\mathbf{r}$  for a homogeneous case. Further, we assume the distribution function to be of the form,

$$f = f^0(\mathbf{v}) [1 + h(\mathbf{v}, t)] \quad (3.40)$$

Small perturbation  


Where  $f^0(\mathbf{v})$  is the Maxwellian equilibrium distribution,

$$f^0(\mathbf{v}) = \left( \frac{m}{2\pi K_B T} \right)^{3/2} \exp \left[ - \left( \frac{m\mathbf{v}^2}{2K_B T} \right) \right] \quad (3.41)$$

Substituting (3.40) and (3.41) into equation (3.39), and remembering that  $f$  is only function of  $\mathbf{v}$  and  $t$ ,

$$\frac{\partial h}{\partial t} = Kh \quad (3.42)$$

We define an inner product  $(h_A, h_B)$  of two real functions of  $\mathbf{v}$  by

$$(h_A, h_B) = \int_{E^3} d\mathbf{v} f_0(\mathbf{v}) h_A(\mathbf{v}) h_B(\mathbf{v}). \quad (3.43)$$

Where  $E^3$  denotes the three-dimensional Euclid space. One can to prove that the operator  $K$  is self-adjoint:

$$(h_A, Kh_B) = (Kh_A, h_B) \quad (3.44)$$

An important consequence follows from a self-adjoint operator is that  $K$  has real eigenvalues. Therefore, let  $\Phi_n(\mathbf{v})$  be the eigenfunction and  $\lambda_n$  be the corresponding eigenvalue of  $K$ , we have

$$K\Phi_n = \lambda_n \Phi_n, \quad (3.45)$$

where  $\Phi_n$  is a real function and a discrete  $\Phi$  was assumed for simplicity.  $\Phi_n$  is normalized as follows,

$$(\Phi_n, \Phi_n) = \int d\mathbf{v} f_0(\mathbf{v}) |\Phi_n|^2 = 1. \quad (3.46)$$

The function  $\{\Phi_i\}$  form a complete orthogonal basis over the interval  $(0, \infty)$ ,

$$(\Phi_n, \Phi_m) = \int d\mathbf{v} \Phi_n \Phi_m f^0(\mathbf{v}) = 0. \quad (3.47)$$

It has been proved that  $\lambda_n = 0$  is an eigenvalue (From the Boltzmann H theorem, all other eigenvalues have to be negative). In fact, since we have assumed the gas is homogenous, it is not surprising one of the linearized collision operator  $K$ 's eigenvalues is zero that corresponds to collisionless gas. It is degenerate and has five eigenfunctions: a constant, three components of velocity, and kinetic energy. Since we are dealing with the case in which the wavelength of the incident light is large (This will be clearer in the next part), they are, in fact, five hydrodynamic modes that correspond to the conservation of mass, momentum and energy. For an ideal monatomic gas an orthonormal set of eigenfunctions can be written as:

$$\begin{aligned} \lambda_1 = 0 & & \Phi_1 = 1 \\ \lambda_2 = 0 & & \Phi_2 = \left( \frac{m}{K_B T} \right)^{1/2} v_x \\ \lambda_3 = 0 & & \Phi_3 = \left( \frac{m}{K_B T} \right)^{1/2} v_y \\ \lambda_4 = 0 & & \Phi_4 = \left( \frac{m}{K_B T} \right)^{1/2} v_z \end{aligned}$$

$$\lambda_5 = 0 \qquad \Phi_5 = \left(\frac{2}{3}\right)^{1/2} \left[ \left(-\frac{3}{2}\right) + \left(\frac{m}{2K_B T}\right) v^2 \right]$$

(3.48)

### 3.2.3 Inhomogeneous Case

Since the distribution function is now a function of position so:

$$f = f(\mathbf{r}, \mathbf{v}, t) = f^0(\mathbf{v}) [1 + h(\mathbf{r}, \mathbf{v}, t)]$$

(3.49)

Do the same as what we did in part 1), we get

$$\frac{\partial h}{\partial t} + v_i \frac{\partial h}{\partial x_i} = Kh$$

(3.50)

We take the Fourier transform of equation (3.50),

$$\partial_t h + i \mathbf{q} \cdot \mathbf{v} h = Kh(t, \mathbf{q}, \mathbf{v}) .$$

(3.51)

If  $\{\Psi_n\}$  are the eigenfunctions of operator  $K - i \mathbf{q} \cdot \mathbf{v}$ , we have

$$(K - i \mathbf{q} \cdot \mathbf{v}) \Psi_n(\mathbf{v}) = \bar{\lambda} \Psi_n(\mathbf{v}) .$$

(3.52)

Still,  $K - i\mathbf{q} \cdot \mathbf{v}$  satisfies

$$(h_A, [K - i\mathbf{q} \cdot \mathbf{v}]h_B) = ([K - i\mathbf{q} \cdot \mathbf{v}]h_A, h_B), \quad (3.53)$$

but it is no longer Hermitian.

Suppose  $\mathbf{q}$  is small which means that the wavelength is very large and we consider  $(-i\mathbf{q} \cdot \mathbf{v})$  as a small perturbation and for simplicity,  $\mathbf{q}$  vector is aligned on the  $x$ -axis. Let  $\bar{\lambda} = \lambda^{(0)} + \lambda^{(1)} + \lambda^{(2)} + \dots$ , then we have

$$(K - iqv_x)\Psi_n = \bar{\lambda}_n \Psi_n \quad (3.54)$$

with

$$\Psi_n = \sum_{m=1}^5 a_{nm} \Phi_m. \quad (3.55)$$

Substituting (3.55) into (3.54) and knowing that,  $K\Phi_n = 0$ , we obtained a set of algebraic equations,

$$-i \sum_{m=1}^5 \omega_{jm} a_{nm} = \bar{\lambda}_n a_{nj}, \dots, j=1, \dots, 5, n=1, \dots, 5 \quad \dots (3.56)$$

where  $\omega_{jm} = \int dv f^0(\mathbf{v}) \Phi_j(\mathbf{v}) qv_x \Phi_m(\mathbf{v})$ .

Using the eigen-functions, we got in part (2.1). The determinant of the coefficients matrix must be 0 to ensure non-trivial solutions of  $a_{nm}$ ,

$$\begin{vmatrix} -\bar{\lambda} & -iqu & 0 & 0 & 0 \\ -iqu & -\bar{\lambda} & 0 & 0 & -i(\frac{2}{3})^{1/2} qu \\ 0 & 0 & -\bar{\lambda} & 0 & 0 \\ 0 & 0 & 0 & -\bar{\lambda} & 0 \\ 0 & -i(\frac{2}{3})^{1/2} qu & 0 & 0 & -\bar{\lambda} \end{vmatrix} = 0, \quad (3.57)$$

Here  $u = \left(\frac{k_B T}{m}\right)^{1/2}$ .

Finally, we got

$$\begin{aligned} \bar{\lambda}_1 &= +iqv_s, & \Psi_1 &= 2^{-1/2} \left[ \left(\frac{3}{5}\right)^{1/2} \Phi_1 - \Phi_2 + \left(\frac{2}{5}\right)^{1/2} \Phi_5 \right], \\ \bar{\lambda}_2 &= -iqv_s, & \Psi_2 &= 2^{-1/2} \left[ \left(\frac{3}{5}\right)^{1/2} \Phi_1 + \Phi_2 + \left(\frac{2}{5}\right)^{1/2} \Phi_5 \right], \\ \bar{\lambda}_3 &= 0, & \Psi_3 &= \Phi_3, \\ \bar{\lambda}_4 &= 0, & \Psi_4 &= \Phi_4, \\ \bar{\lambda}_5 &= 0, & \Psi_5 &= \left(\frac{2}{5}\right)^{1/2} \left[ -\Phi_1 + \left(\frac{3}{2}\right)^{1/2} \Phi_5 \right] \end{aligned} \quad (3.58)$$

with

$$v_s = \left(\frac{5 k_B T}{3 m}\right)^{1/2}$$



This is actually the velocity of sound of an ideal monatomic gas. Remember we have assumed the gas was ideal and monatomic at the beginning. For more general case, we can choose different coefficients for the homogeneous eigenfunctions and make sure it is still orthonormal. Then we can go over part 2) and get a set of eigenfunctions:

$$\begin{aligned}
 \bar{\lambda}_1 &= +iqv_s, & \Psi_1 &= (c_v/c_p)^{1/2} \left[ 1 + (c_p/c_v)^{1/2} v_x/u + \frac{E - \bar{E}}{\bar{E}} \right], \\
 \bar{\lambda}_2 &= -iqv_s, & \Psi_2 &= (c_v/c_p)^{1/2} \left[ 1 - (c_p/c_v)^{1/2} v_x/u + \frac{E - \bar{E}}{\bar{E}} \right] \\
 \bar{\lambda}_3 &= 0, & \Psi_3 &= v_y/u, \\
 \bar{\lambda}_4 &= 0, & \Psi_4 &= v_z/u, \\
 \bar{\lambda}_5 &= 0, & \Psi_5 &= (c_v/c_p)^{1/2} \left[ \frac{E - \bar{E}}{\bar{E}} \right],
 \end{aligned}
 \tag{3.59}$$

where  $E = \frac{1}{2}mv^2$ ;  $\bar{E} = c_v T$ .  $c_p$  and  $c_v$  are the specific heats at constant pressure and constant volume respectively; the sound velocity now is defined as

$$v_s = \left( \frac{(c_p/c_v)k_B T}{M} \right)^{1/2} \tag{3.60}$$

The eigenfunctions  $\{\Psi_n\}$  constitute a properly normalized set of mutually orthogonal functions. To this extent, there are still three degenerate states where the eigenvalues equal zero.

We can tell from above results that the first two modes are traveling with the velocity of sounds. There are three stationary hydrodynamic modes. If we go further to the second perturbation order, which we will show in the next, there will be damping effects in the first two traveling modes that are reflected in the power spectrum and correspond to the Brillouin scattering sidebands.

So far we have treated the homogeneous case and the inhomogeneous case using perturbative methods without considering the internal structure of molecules. Now we shall consider an ideal diatomic gas in which only the rotational and translational degree are allowed.

### 3.2.4 Diatomic Gases

For the case of light scattering by gas molecules, the scattering spectrum is well described by the Fourier transform of the density correlation function  $G(|\mathbf{r}-\mathbf{r}'|, t)$ :

$$I(\omega, \mathbf{q}) \propto \text{Re} \left\langle \hat{e}_{1l} \hat{e}_{2k} \hat{e}_{1l} \hat{e}_{2m} \iint d\mathbf{r} dt G_{iklm} \exp(i\omega t - i\mathbf{q} \cdot \mathbf{r}) \right\rangle. \quad (3.61)$$

Here,  $\hat{e}_1, \hat{e}_2$  are unit vectors of the polarizations of the incident light photons and scattered light photons, respectively.

Since we include the rotational freedom of molecules, the distribution function now becomes,

$$f = f(t, \mathbf{r}, \mathbf{v}, \mathbf{J}). \quad (3.62)$$

The new variable  $\mathbf{J} = \mathbf{J}(\mathbf{n}, \mathbf{M})$  describes the rotational effect;  $\mathbf{n}$  is a unit vector directed along the axis of the molecule;  $\mathbf{M}$  is the angular momentum of a molecule. Based on the assumption that the gas is nonequilibrium, but it is not far from the equilibrium state, the distribution function can be approximated as:

$$f = f^0(\mathbf{v})(1 + h(t, \mathbf{r}, \mathbf{v}, \mathbf{J})) \quad (3.63)$$

The linearized Boltzmann equation is now

$$\frac{\partial h}{\partial t} + \mathbf{v} \cdot \nabla h + (\boldsymbol{\Omega} \times \mathbf{n}) \frac{\partial h}{\partial \mathbf{n}} = \mathbf{K}h \quad (3.64)$$

with initial condition

$$h(0, \mathbf{r}, \mathbf{v}, \mathbf{J}) = \ell_{ii} \alpha_{ik} \ell_{2k} \delta(\mathbf{r}) \quad (3.65)$$

Here,  $\boldsymbol{\Omega} = \mathbf{M}/I$  is the molecule rotation frequency and  $I$  is the molecule moment of inertia;  $\alpha_{ik}$  is the polarizability tensor of the diatomic gas molecules and it can be represented as follows (Landau, 1985),

$$\begin{aligned} \alpha_{ik} &= \alpha_{ik}(\mathbf{J}) \\ &= \alpha_0 \delta_{ih} + \alpha_1 \varepsilon_{ihl} \left( \frac{M_l}{M_0} \right) + \alpha_2 \left( n_i n_k - \frac{1}{3} \delta_{ik} \right) + \dots \end{aligned} \quad (3.66)$$

We take the Fourier transform of equation (3.64), then integrate over the rotation circle, we have

$$(K - i\mathbf{q} \cdot \mathbf{v} + i\omega)h(\omega, \mathbf{q}, \mathbf{v}, \mathbf{J}) = \int d\varphi C(\mathbf{n}, \mathbf{M}) \quad (3.67)$$

where

$$C(\mathbf{n}, \mathbf{M}) = \hat{\ell}_{1i} \alpha_{ik}(\mathbf{n}, \mathbf{M}) \hat{\ell}_{2k} \quad (3.68)$$

The scattering spectrum will take the form

$$I(\omega, \mathbf{q}) \propto \text{Re} \iiint C(\mathbf{n}, \mathbf{M}) f^0(\mathbf{v}) h(\omega, \mathbf{q}, \mathbf{v}, \mathbf{J}) d\Omega d\mathbf{J} d\mathbf{v} \quad (3.69)$$

The rotational term  $\Omega \times \mathbf{n} \cdot \left( \frac{\partial}{\partial \mathbf{n}} \right)$  has disappeared after the integration because we are now focusing on the unshifted Rayleigh-Brillouin scattering therefore the function  $h$  is independent of the unit vector  $\mathbf{n}$ .

Using the explicit representation the polarizability tensor  $\alpha_{ik}$  above, the right hand side of equation (3.69) turns out to be,

$$\int C(\mathbf{n}, \mathbf{M}) d\varphi = C_0 + C_2 (\mathbf{M}/m) \quad (3.70)$$

$C_0$  and  $C_2$  are given explicitly as

$$C_0 = \alpha_0 (\hat{e}_1 \cdot \hat{e}_2)$$

and

$$C_2 = -\frac{1}{2} \alpha_2 [(\hat{e}_1 \cdot \mathbf{M})(\hat{e}_2 \cdot \mathbf{M}) / M^2 - \frac{1}{3} (\hat{e}_1 \cdot \hat{e}_2)] \quad (3.71)$$

Finally the linearized Boltzmann equation takes the form

$$(K - i\mathbf{q} \cdot \mathbf{v} + i\omega)h(\omega, \mathbf{q}, \mathbf{v}, \mathbf{J}) = C_0 + C_2 \quad (3.72)$$

with the scattering spectrum

$$I(\omega, \mathbf{q}) \propto \text{Re} \iiint d\mathbf{J} d(C_0 + C_2) f^0(\mathbf{v}) h(\omega, \mathbf{q}, \mathbf{v}, \mathbf{J}) \quad (3.73)$$

Now, we shall expand function  $h$  by the eigenfunctions of the linearized collision operator  $K$  in the Hilbert space, i.e.,

$$h(\omega, \mathbf{q}, \mathbf{v}, \mathbf{J}) = \sum_{n=1}^{\infty} a_n(\omega, \mathbf{q}) h_n(\mathbf{v}, \mathbf{J}) \quad (3.74)$$

where the first five eigenfunctions are what we got in section 2.3 which corresponding to the five hydrodynamic modes

$$h_n = \Psi_n \quad n = 1, \dots, 5$$

while the eigenfunctions for the non-hydrodynamic modes satisfy

$$K h_n = \beta_n h_n \quad n > 5 \quad (3.75)$$

$\beta_n$  is the corresponding eigenvalue. The  $\beta_n$ s obviously have to be solved through the explicit form of the linearized collision operator  $K$ .

It changes nothing if we let the direction of vector  $\mathbf{q}$  be parallel to the x-axis. Note that we still assume  $i\mathbf{q} \cdot \mathbf{v}$  is small so we can use the perturbation theory and the results we got in part 2.2. One point we want to note here is so far we have only discussed the solution to the kinetic linearized Boltzmann equation in which we assumed the amplitude of the vector  $\mathbf{q}$  is small therefore we could safely use perturbation theory.

Actually, since  $|\mathbf{q}| = \frac{4\pi}{\lambda} \sin(\theta/2)$ ,  $\theta$  is the scattering angle and  $\lambda$  is the wavelength of the incident light and the scattered light, so if we want to make  $\mathbf{q}$  small, either the scattering angle  $\theta$  is small or the wavelength of the employed laser must be large. For the forward scattering,  $\theta$  is small; it is in the hydrodynamic regime. In the case of backscattering, if the light wavelength is not large compared to the mean free path, this perturbation method that we are using here fails and we have to use other methods to solve the linearized Boltzmann equation.

Multiply the equation (3.74) by  $h_1$  and integrate it over the space, using the fact that  $h_1$  is the eigenfunction of  $K$  and the corresponding eigenvalue is  $iqv_x$ , we obtain

$$i(\omega + qv_x)a_1 + i \sum_{n>5} (qv_x)_{1n} a_n = C_0 (C_v / 2C_p)^{1/2} \quad (3.76a)$$

with

$$(qv_x)_{nm} = \int h_n^* f^0(qv_x) h_m d\mathbf{J} d\mathbf{v}. \quad (3.77)$$

Then we can go through for  $h_2, h_3, \dots$ , we obtain a set of equations:

$$i(\omega - qv_s)a_2 - i \sum_{n>5} (qv_x)_{2n} a_n = C_0(C_v/2C_p)^{1/2} \quad (3.76b)$$

$$-i\omega a_3 + i \sum_{n>5} (qv_x)_{3n} a_n = 0 \quad (3.76c)$$

$$-i\omega a_4 + i \sum_{n>5} (qv_x)_{4n} a_n = 0 \quad (3.76d)$$

$$-i\omega a_5 + i \sum_{n>5} (qv_x)_{5n} a_n = 0 \quad (3.76e)$$

$$(-i\omega + \beta_n)a_n + i \sum_m (qv_x)_{nm} a_m = C_{2n} \quad (3.76f)$$

with

$$C_{2n} = \langle h_n | C_2 \rangle = \int h_n^* f^0 C_2 dz. \quad (3.78)$$

The scattering power spectrum changes accordingly to

$$I(\omega, \mathbf{q}) \propto \text{Re}[C_0(C_v/2C_p)(a_1 + a_2) + C_0 C_v^{-1/2} a_5] + \text{Re} \sum_{n>5} C_{2n} a_n \quad (3.79)$$

We can solve this set of equations by first solving equation (3.76f) for  $a_n$  and substituting it into other equations to get the first five  $a_n$ s. Finally, we get the Rayleigh scattering spectrum as follows:

$$I(\omega, \mathbf{q}) = I_0(\omega, \mathbf{q}) + I_2(\omega, \mathbf{q}) \quad (3.80)$$

$$I_0(\omega, \mathbf{q}) = (C_v/2C_p)C_0^2 \left\{ \frac{\Gamma_1}{(\omega + qv_s)^2 + \Gamma_1^2} + \frac{\Gamma_2}{(\omega - qv_s)^2 + \Gamma_2^2} + \frac{2\Gamma_5}{C_v(\omega^2 + \Gamma_5^2)} \right\} \\ + \left( \frac{C_v}{2C_p} \right)^{1/2} C_0 \Delta C_1 \left\{ \frac{\omega + qv_s}{(\omega + qv_s)^2 + \Gamma_1^2} - \frac{\omega - qv_s}{(\omega - qv_s)^2 + \Gamma_1^2} \right\} \quad (3.81)$$

$$I_2(\omega, \mathbf{q}) = \sum_{n>5} (C_{2n})^2 \frac{\beta_n}{\omega^2 + \beta^2} - (\Delta C_3^2 + \Delta C_4^2) \frac{\Gamma_3}{u^2 + \Gamma_3^2} \\ - (\Delta C_1)^2 \left\{ \frac{\Gamma_1}{(\omega + qv_s)^2 + \Gamma_1^2} + \frac{\Gamma_1}{(\omega - qv_s)^2 + \Gamma_1^2} \right\} \quad (3.82)$$

where  $\Delta C_n$  s are given by

$$\Delta C_j = \sum_{n>5} (qv_x)_{jn} C_{2n} / \beta_n \quad (3.83)$$

These  $\Gamma$ 's are damping coefficients that couple the five hydrodynamic modes and those infinite number of non-hydrodynamic modes. Some of them are given by

$$\Gamma_1 = (q^2/2\rho) \{ (4/3)\eta + \xi + \kappa m [(1/C_v) - (1/C_p)] \}$$

$$\Gamma_3 = (q^2/2\rho)\eta \quad \Gamma_5 = q^2(m/\rho C_p)\kappa \quad (3.84)$$



$\eta$ ,  $\xi$ , and  $\kappa$  are the shear viscosity, bulk viscosity and the thermal conductivity respectively.

From the scattering spectrum above,  $I_0$  describes the polarized Rayleigh-Brillouin scattering while  $I_2$  part describes the *depolarized Rayleigh scattering* where there is a dip right in the middle and two dips on the Brillouin sidebands. If the polarization of the scattered light is parallel to the polarization of the incident light photons— $(\hat{e}_1 \cdot \hat{e}_2)=1$ , according to equation (3.71)—the coefficient  $C_0$  is not 0 and then both the  $I_0$  and  $I_2$  parts exist in equations (3.81) and (3.82) and they describe the total Rayleigh-Brillouin scattering. On the other hand, if polarization of the scattered light is perpendicular to the polarization of the incident light, i.e., it was depolarized, since  $\hat{e}_1 \cdot \hat{e}_2 =0$ , according to equations (3.71),  $C_0$  is now equal to 0, only the  $I_2$ , the depolarized part, survives. It can be seen from the representation of the polarization tensor of molecules and the related derivation that depolarized Rayleigh scattering is due to a tensorial fluctuation. Since the polarization of the scattered light has been changed during this scattering, it is no longer coherent anymore. The proportion of depolarized part in the total Rayleigh scattering varies from different species of gases. For gas species in the air like  $O_2$  and  $N_2$ , their molecular anisotropies are comparatively large; the depolarized parts in these gases will be large too (Table 4.4).

We also find that  $I_0$  is composed of three Lorentzian distributions and two additional asymmetric components that are small compared to the three Lorentzian shape terms because  $\Delta C_1$  is usually small. We can also get these three components using the Navier-Stokes equation. In fact, Navier-Stokes equation can be derived from the Boltzmann equation by making several appropriate approximations. Since  $\Gamma_5$  is only

related to the thermal conductivity, the third Lorentzian actually is one component of Rayleigh scattering which is due to ‘thermal fluctuations’. The other two components are called “Brillouin Scattering” which is due to pressure fluctuations. The integrated intensities of them obey the famous Landau-Placzek relationship

$$\frac{I_{thermal}}{I_{Brillouin}} = \gamma - 1 \quad (3.85)$$

here  $\gamma$  is known to be the ratio of specific heats of molecules. However, with other two additional terms and the depolarized part of Rayleigh scattering, when the gas is not ideal gas, Landau-Placzek ratio will not stick to the above value, it will increase. The increased value varies from the different gases. More details can be found from additional references and our data analysis later on.

### 3.3 An Alternative Approach and Tenti’s Model

We have known that from part 3.2.2 that the perturbation method fails when the mean free path of the gases is comparable with the light wavelength when the scattering angle  $\theta$  is not very small. However, by introducing the non-hydrodynamic modes in part 3.2.3, we were being able to get a clear picture of the Rayleigh-Brillouin Scattering. Some alternative methods had been developed in solving the kinetic equations since 1950s. One of them was used to solve the renowned linearized Wang-Chang Uhlenbeck equation is discussed as below.

The linearized Wang-Chang Uhlenbeck (WCU) equation reads,

$$\begin{aligned} \frac{\partial f}{\partial t} + \mathbf{v} \cdot \nabla h_i(\mathbf{v}) &= n \sum_{jkl} x_j \iiint d^3 \mathbf{v}_1 \int_0^{2\pi} d\Omega \int_0^\pi \sigma_{ij}^{kl}(\mathbf{v}_d, \theta) \mathbf{v}_{rel} \cdot f^0(\mathbf{v}_1) [h_k(\mathbf{v}') + h_l(\mathbf{v}_1') - h_i(\mathbf{v}) - h_j(\mathbf{v}_1)] \\ &\equiv nKh \end{aligned} \quad (3.86)$$

where  $x_j$  is the average fraction of molecules with internal energy  $E_j$ ,

$$x_j = \frac{\exp(-E_j/k_B T)}{\sum_i \exp(-E_i/k_B T)} \quad (3.87)$$

$K$  is the linearized collision operator. The only difference between the linearized Boltzmann equation (3.37) and linearized WCU equation (3.86) is that the WCU equation averages over the different internal energies of the gas molecules.

Using the explicit differential cross sector form and some approximations, one can expand the right-hand side of equation (3.86) by the hydrodynamic-mode eigenfunctions we got in section 3.2.2. Different approximations give different models. One famous model that has been widely used is Tenti's S6 model. In the S6 model, the linearized WCU equation generates six moment equations with appropriate approximations. One has to solve the six moment equations to obtain the density fluctuation spectrum. The polarized Rayleigh-Brillouin scattering spectrum is described by four dimensionless parameters:  $x, y, z$ , and  $f$ :

$$x = \omega / \sqrt{2q\nu_0}, \quad y = nk_B T / \sqrt{2\eta k\nu_0}, \quad z = 3\xi / 2\gamma \eta, \quad f = m\lambda / \eta k_B (\frac{3}{2} + c_v) \quad (3.88)$$

where  $\omega$  is the light frequency,  $\nu_0$  is the average molecule velocity,  $k_B$  is the Boltzmann constant,  $\eta$  and  $\xi$  are the shear and bulk viscosity respectively,  $c_v$  is the molecular specific heat and  $\gamma = c_p / (\frac{3}{2} + c_v)$ . By standard kinetic theory,  $y$  is a measure of the ratio

of the wavelength to the molecular mean free path, and  $x/y$  gives the ratio of the frequency to the collision frequency.

The linearized WCU equation, however, loses its validity when it is applied on the gas molecules with degenerate internal states. For some cases, correlations between two degenerate states could be affected by the so-called reorienting collisions among molecules. In fact, those correlations are involved mainly in phenomena of a tensorial character, which is related to the depolarized Rayleigh Scattering as we have shown in part 3.2.3.

The more appropriate kinetic equation is the linearized Waldmann-Snider (WS) equation, which treats the internal degrees of freedom quantum mechanically. However, in the actual measurements of atmosphere properties by lidar technology, since our interest is mainly the polarized Rayleigh-Brillouin scattering caused by the density fluctuations, the linearized WCU equation is good enough and it is much simpler than the linearized WS equation.

The kinetic S6 model has been widely used in various atmospheric researches. It is good on diatomic molecules with no internal degenerate energy levels. Shown in figure 3.4 is the change of the Rayleigh Brillouin scattering line shape by the S6 model.

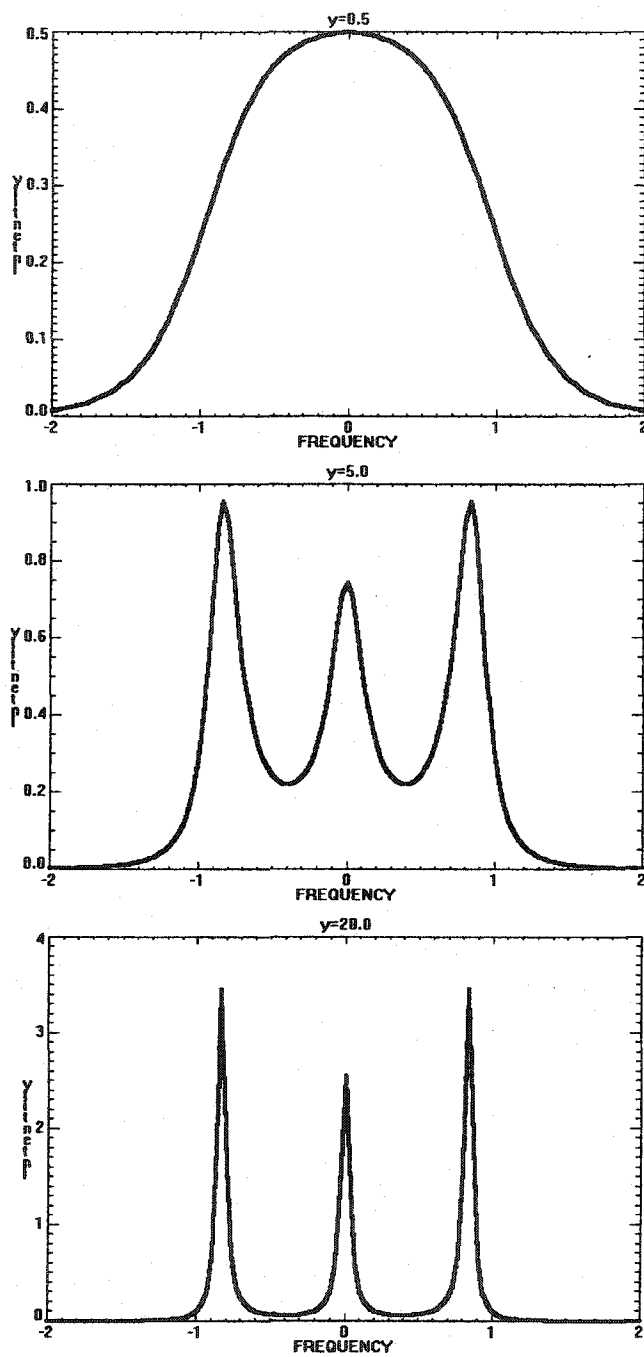


**Figure 3.4** Change of S6 model from kinetic regime to hydrodynamic regime. The first one is S6 model in kinetic regime and the bottom one illustrates S6 model in the hydrodynamic regime, while the middle one is in between ( $y=5.0$ ).

## CHAPTER 4

### RAYLEIGH-BRILLOUIN SCATTERING SPECTRUM AND TEMPERATURE PROFILE

#### 4.1 Introduction

Global wind measurements are important for improving long-term weather forecasts as well as for other atmospheric research on aerosol and pollution. Active remote sensing is an effective way to achieve the goal of observing the global wind field. There are two different optical methods both utilizing the wind-induced Doppler shift of backscattered laser light. They are coherent detection lidar systems and direct detection lidar systems. For the latter, there are two kinds of direct lidar systems: fringe imaging and edge technology. GroundWinds lidar is a modern fringe imaging incoherent Doppler lidar, which detects the Doppler shift from the altered spectra of backscattered light.

The GroundWinds lidar system, like most of other lidar systems, is composed of four key elements: 1) the laser, 2) the transmitting telescope, 3) the receiving telescope, and 4) optics and detection system. In the next section, we will discuss these four elements.

## 4.2 Instrument Description/Specifications

### 4.2.1 Laser

The GroundWinds lidar system uses a commercial pulsed Nd:YAG (NeodymiumYttrium-Aluminum-Garnet) laser. Before the laser beam emerges from the instrument, it passes through a beam expander that reduces the divergence of the emerging light. The laser is fired at a repetition rate of 10 Hz. Its specifications are listed in table 4.1.

**Table 4.1 Laser Specifications**

Manufacturer Model	Continuum 8010
Type	Nd:YAG
Pulse Lengths	8 ns
Power output	4 W
Central wavelength	532 nm Doubled
Type	Multicavity, dielectric

### 4.2.2 Telescope

The telescopes—transmitting telescope and receiving telescope—are mounted together on a common gimbal, which can rotate azimuthally and is fixed at 45° elevation. The receiving telescope specifications are listed below (Table 4.2)

**Table 4.2 Telescope Specifications**

Manufacturer / Type	Torus / Cassegrain (receiving)
Telescope diameter	0.5 m
Effective telescope collecting area	1963 cm <sup>2</sup>
Focal Length	2.0 m
Telescope FOV (half angle)	0.10 mrad
Tolerance on Focus and Alignment	0.02mrad
Telescope Transmission	0.81
Etendue (area * solid angle product)	6.17×10 <sup>-5</sup> cm <sup>2</sup> -sr
Zenith Angle	45°
Type of view	Slew & Stare

### 4.2.3 Spectrometer

GroundWinds lidar systems use a specialized Fabry-Perot (FP) interferometer that is based on the High Resolution Doppler Imager (HRDI) instrument (Hays 1993). The backscattered light collected by the receiving telescope is fed to the interferometer through an optical fiber. The reflected light from Fabry-Perot etalon is reused. This is called light recycling; a new feature first implemented in the GroundWinds lidar systems. Light recycling enhances the efficiency of the interferometer subsystem. A Fabry-Perot interferometer is typically composed of a Fabry-Perot etalon—two flat parallel plates—whose surfaces are coated with reflective materials and auxiliary lens. The GroundWinds lidar molecular and aerosol etalons specifications are listed in table 4.3.



**Table 4.3 Molecular and Aerosol Etalon Specifications**

	Molecular Etalon	Aerosol Etalon
Plate spacing	1.85 cm	15 cm
Number of orders	7.8	6.5
Free spectral range	0.3333 cm <sup>-1</sup>	0.03333 cm <sup>-1</sup>
Plate diameter	6.0 cm	6.0 cm
Coated aperture	4.0 cm	4.4 cm
Working aperture	2.6 cm.	4.4 cm.
Doppler dynamic range	2660 ms <sup>-1</sup> /order	266 ms <sup>-1</sup> /order
Reflectivity	0.86	0.86
Etalon defects (1/e)	5 nm	5 nm
Loss per plate	0.01	0.01
Number of channels	312	312
Focal Length of Collimator	6.0 cm (GPX-25-60-2)	10.0 cm (GPX-50-150-5)
Focal length of objective	26.0 cm (DBL14182 JML)	70.0 cm (CPX10506 JML)
f/number	2.3	2.3
Spacing type	PZT tunable	PZT tunable
Index of Refraction	1.0	1.0

#### 4.2.4 Optics

After the backscattered photons emerge from the Fabry-Perot interferometer and focused by the lens, they form a set of concentric rings. These concentric fringes are then converted to a linear pattern (Figure 4.1) by an optical device called Circle to Line Interferometer Optical system (CLIO)(Hays 1990). Figure 4.2 illustrates how the CLIO works.

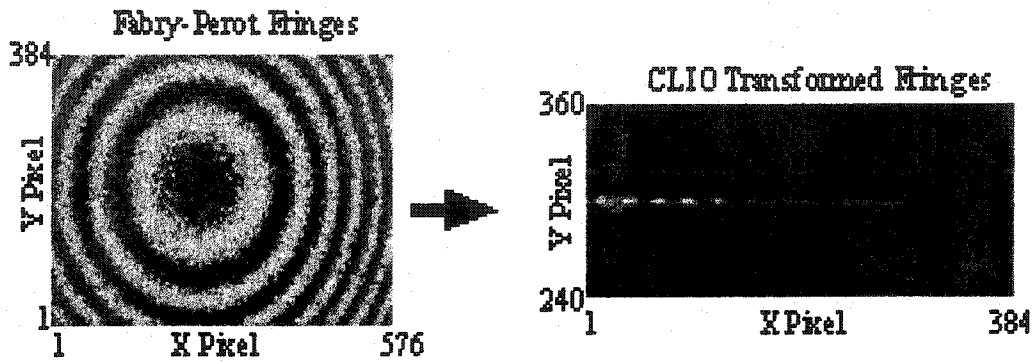


Figure 4.1 Transformation of Fabry-Pérot circular fringes to linear.

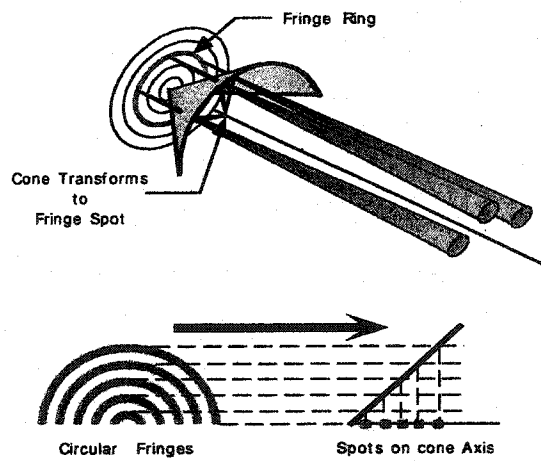
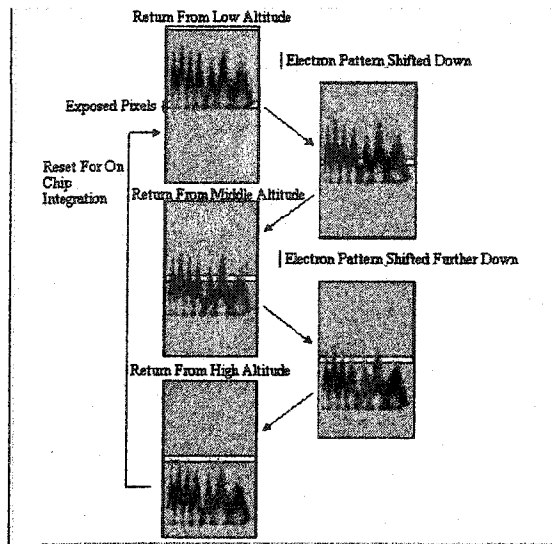


Figure 4.2 Conceptual ray trace illustrating the CLIO concept.

#### 4.2.5 Detector

A Charge-Coupled Device (CCD) detects the spectra produced by the CLIO.



**Figure 4.3 CCD Lidar Detector time history. As the light scatters from different altitudes, the image is shifted across the detector (steps a through e). At the end the image is shifted back to the start for the next laser pulse (step e to a). Only the segment of the CCD marked “open” is actually exposed to light.**

### 4.3 Clean Spectra

Our main goal of this research is to obtain and study Rayleigh-Brillouin backscattering spectra in air. As we stated earlier, the GroundWinds lidar system can measure the molecular RBS backscattering spectra in the atmosphere making it useful at high resolution at high altitude when the air is clear. However, in real measurements, we cannot avoid noise, instrument-broadening effects, and other factors (for example, in our measurements, aerosol contamination) that compromise the true molecular RBS spectra. We discuss these effects and how to eliminate or minimize them so as to acquire genuine RBS spectra to which we can compare current models.

#### 4.3.1 Description of GroundWinds Data

The back-scattered photons received by the telescope processed through the Fabry-Perot interferometer and CLIO will register on a narrow wedge region in the center of a high quantum efficiency CCD. The circular fringes produced by the Fabry-Perot interferometer are converted into a linear pattern that can be detected with a conventional linear detector. For the molecular channel, the CCD records the six outmost fringes of the interferometer. The variation of photon number density across each fringe is the Rayleigh-Brillouin backscattering spectrum convolved with the instrument function.

The first fringe, the innermost in all of the fringes, is always the best measured Rayleigh-Brillouin lineshape for the following reasons: first, its spatial distribution is broader than any other fringe due to the cosine dependence of the spectral response as the distance (angle) off the optical axis of the Fabry-Perot interferometer is increased; second, the illumination pattern of the fiber optics used to transmit the signal does not obstruct the first fringe.

To measure the Rayleigh-Brillouin scattering spectrum at different altitudes, the exposed stripe on the detecting CCD is shifted up at a fixed rate when the outgoing laser beams is on. Before the laser is fired, the CCD begins shifting at a high rate. For any row of returned signals, the corresponding altitude can be determined by the shifting rate of the CCD and the time when laser was fired. A reference signal can also be obtained by making a small portion of transmitted laser light pass through the same optical path as the returned signal from the telescope. Therefore this reference signal provides a measure of the entire instrument broadening effects and system information. By comparing the

observed backscattered spectrum with the reference spectrum the Rayleigh Brillouin backscattering spectrum can thus be obtained.

As was stated above, the CCD detector is shifting upwards at a high rate to record the backscattering spectrum at different altitudes. Two rows of measured data next to each other may not be totally exclusive or independent; in other words, a row of data might be contaminated by some photon counts from adjacent rows. This cross talk of different rows of data must also be considered in the data analysis.

Another important issue that must be carefully treated is the optical defects described earlier. Most of the optical defects are instrumental because many optical devices are astigmatic and not strictly linear. The asymmetries appear in the measured spectrum. For the GroundWinds data, asymmetries can be seen in the measured Rayleigh-Brillouin scattering spectra. However, these asymmetries can be eliminated if the causes and sufficient background information are known. For example, the asymmetry caused by projecting the circular fringe data onto the linear detector CCD can be corrected analytically.

#### **4.3.1.1 Criteria for Data Selection**

Several other factors have significant effects on the data. One of them is the overlap of the telescope field-of-view with the laser beam. The degree of overlap has a large effect on the photometric return. The returned signal is related to the angle between the laser beam and the optical axis of the receiving telescope. Furthermore, the receiving telescope is focused at infinity, therefore, a portion of returned photons scattered by air molecules at low altitudes will not be focused into the fiber optics receiver at the focal plane of the

telescope. The overlap function is complicated and more detail can be found in Measures (1984) and Irgang (2000). For GroundWinds lidar system, the overlap function is steep below 2 km (ref. Figure 5.3). For this reason, we will basically focus on the data above 2 km in our analysis.

#### 4.3.2 Broadening Effects, Turbulence and Line-of-Sight Winds

Normally, we must consider the following two broadening effects for a light scattering experiment in the air: Instrument broadening and turbulence broadening. Other broadening effects such as radiative broadening are small.

When a monochromatic light beam passing through an optical system—assuming there is not any frequency-changing optical device in the optical system—imaged through an optical (e.g. Fabry-Perot) interferometer, then detected by a common electro-optical detector, the power spectrum measured is a Lorentzian while the power spectrum of the incident light is a delta function. The reason is that when a light beam is directing through an optical system, it is subject to some power dissipation, which can usually be represented as an exponential function of time ( $e^{-at}$ ). After this exponential function being Fourier transformed into frequency space, the corresponding power spectrum is a Lorentzian (expression 4.2) with its width determined by the power loss coefficients (Figure 4.4).

The interferometer disperses light in frequency or wavelength along the axis of the detector. A spectrum is obtained by plotting the integrated photon intensities across the detector. The distance between any two points on this axis represents a mapping of the frequency difference depending on several optical parameters. In the ideal case, all

the registered photons on the detector fall into a rectangular slab. We know this is not so for the real measurements. For the real measurements with less than perfect optical devices and alignments, the registered photons form an elliptic area with its long axis being the frequency axis (figure 4.5b) aligned with the spatial x-axis of the detector (rows). Usually the photon intensity is low along the boundary and high in the center of the ellipse. However, with the limited resolution of current optical devices and technologies, we will obtain a pseudo-elliptic area as shown in figure 4.5 (a).

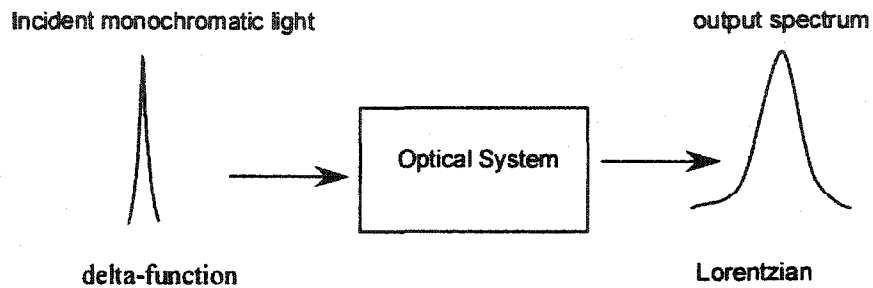


**Figure 4.4** A delta-function is broadened after passing through an optical system.

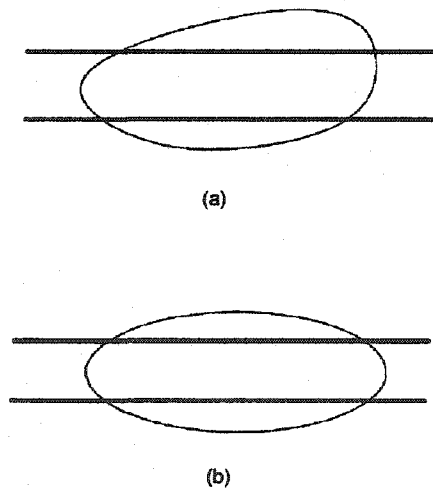


**Figure 4.5** Illustration of distribution of registered photons on the detector with (a) a real measurement and (b) a perfect measurement.

This pseudo-elliptic area will cause some asymmetry and, in some cases, non-linearity. Depending on the degree of the vertical spreading (in the direction of the short axis of the ellipse) and detection method, a small portion of photons of a fringe could be mixed with neighboring fringes.

For GroundWinds lidar system, the reference signal is obtained by directing a small fraction of outgoing laser light to the receiver without any molecular scattering by air. Both the reference signal and the measured molecular signal will be subject to the problems described above.

#### 4.3.2.1 Instrument Broadening

The measured spectra are broadened by the interferometer instrument function, which is normally an Airy function (Lothian 1975; Hernandez 1986) as well as other instrument broadening effects, described by a Lorentzian distribution, of the form

$$I(\omega) = \frac{1}{\pi} \frac{a}{\omega^2 + a^2}. \quad (4.2)$$

where  $a$  is the width. The full width at half maximum (FWHM) of a Lorentzian line is  $2a$ . A combination of Lorentzians can be used to describe the total broadening effects (Vaughan 1989).



### 4.3.3 Elimination of Broadening Effects and Deconvolve Algorithm

The broadening effect of FP interferometer, computable from known FP parameters, can be removed by inverse transform methods (Killeen 1984). We will use a similar method to partially remove the GroundWinds broadening effects. The inversion problem including deconvolution for many cases can be described by the following Fredholm integral equation of the first kind,

$$\int_a^b k(x, x') f(x') dx' = g(x) \quad a \leq x \leq b \quad (4.3)$$

Here  $k(x - x')$  is the kernel, functions  $f(x)$  is the unknown real photon spectrum and  $g(x)$  is the measured spectrum respectively. The simplest non-trivial deconvolution case is of the following form

$$\int_{-\infty}^{\infty} k(x - x') f(x') dx' = g(x) \quad (4.4)$$

By writing equation (4.2) in the form of (4.3), we assume that the kernel  $k(x - x')$  introduces no additional dispersion.

The GroundWinds data are also contaminated by white noise from the CCD and the readout—creating an ill posed problem. Miller (1974) pointed out that many ill-posed problems have been quite well tackled by expansion methods.

Expanding function  $f$  as,

$$f(x) = \sum_{i=0}^n (f, \varphi_i) \varphi_i(x)$$

where functions  $\{\varphi_i\}$  are arbitrary but must form a complete set of orthonormal functions.

Substituting into equation (4.3), we get

$$\sum_{i=0}^n a_i \int_{-\infty}^{\infty} k(x-x') \varphi_i(x') dx' = g(x)$$

with

$$a_i = (f, \varphi_i)$$

In our data, function  $k(x-x')$  embodies all broadening effects. Function  $g(x)$  is the raw data. We chose

$$\begin{aligned} \varphi_i(x) &= 1 & i < x < i+1 \\ &= 0 & \text{otherwise} \end{aligned}$$

We know  $k(x-x')$ ,  $\varphi_i$  and  $g(x)$ , the only unknowns are the coefficients  $\{a_i\}$ . Since any measured spectrum is composed of discrete data points, the set  $\{a_i\}$  is therefore the corresponding deconvolved spectrum. We can fit the raw data to get  $\{a_i\}$ .

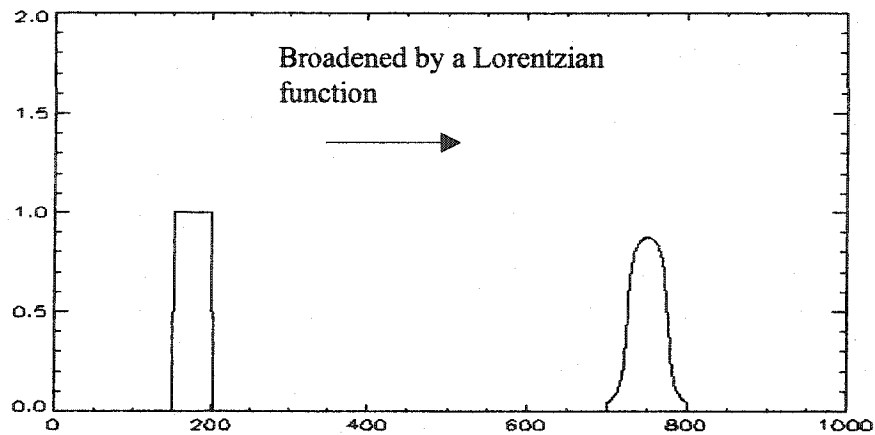


Figure 4.6 Illustration of a function broadened by a Lorentzian function

#### 4.3.3.1 Thermal Blooming

Thermal blooming was first observed and discussed by Leite (1964). When a laser beam is propagating through the atmosphere, it heats the air. The air was in thermal equilibrium before the laser beam was turned on, the local heating will then produce a local change of the refractive index, which in turn will change or redirect the propagating laser beam. This is called thermal blooming. Thermal blooming is a critical issue for high power laser beam.

For a CW (continuous wave) laser beam of total power  $P$  being emitted from an aperture of diameter  $d$  into air at 1 atm, Ulrich and Walsh (1978) estimated the threshold power  $P_{th}$  for the onset of thermal blooming in a transverse flow

$$P_{th} \approx \frac{\pi \gamma p}{2 \gamma - 1} \frac{1}{\alpha(n-1)} \frac{\lambda^2 v}{d} \quad (4.6)$$

Here  $p$  is the air pressure,  $\gamma$  is the specific heats ratio,  $\alpha$  is the laser beam absorption coefficient,  $v$  is the airflow velocity. For the GroundWinds NH lidar system, we have

$$\begin{aligned} p &= 10^5 \text{ pascal} & n-1 &\cong 3 \times 10^{-4} \\ \gamma &= 1.4 & \lambda &= 5320 \times 10^{-10} \text{ m.} \end{aligned}$$

Substituting these values into (4.1), we obtain

$$P_{th} = 5.2 \times 10^{-4} \frac{v}{\alpha d} \quad (4.7)$$

in SI units. If we choose

$$\alpha = 1.0 \times 10^{-3} \text{ km}^{-1} \quad v = 0.3 \text{ m/s} \quad (\text{relatively quiet air})$$

and  $d=7$  mm for GroundWinds lidar system laser beam, we predict a power threshold for thermal blooming to be  $P_{th}=2200.0\text{W}$ . The GroundWinds laser power is 4W. We will therefore neglect the thermal blooming effect in our analysis.

#### 4.3.4 Aerosol and Planetary Boundary Layer (PBL)

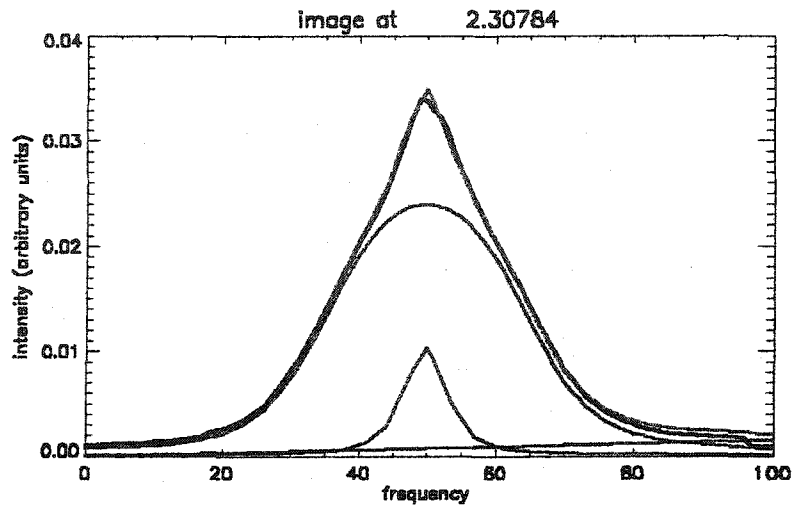
One important issue, in GroundWinds data analysis as well as in many other direct lidar systems is aerosol contamination of the molecular Rayleigh-Brillouin backscattering spectrum. For a direct lidar system as GroundWinds lidar system, it is important to separate the molecular and aerosol signals. Ideally the aerosol signal can be isolated from the molecular signal because the aerosol signal, a result of the Mie scattering in the air, is normally a narrow Gaussian, much narrower than the corresponding molecular RBS spectrum. However, this is not the case in the real lidar measurements because of instrumental broadening. This broadening is not necessarily well behaved and will likely spread in the y-direction on the detector plane. Shown in figure 4.7 (a) and (b) are measured Rayleigh spectra at different 2.3km and 7.8km respectively. We can easily see that in figure 4.7(a), which corresponds to an altitude 2.3km, a strong aerosol signal is mixed with the molecular signal. In figure 4.7 (b), the aerosol signal is too weak to be apparent.

The planetary boundary layer (PBL) is the lower part of the troposphere. The PBL is directly influenced by the friction drag of the Earth, solar heating, and human activities, etc. The thickness of PBL is not constant. Due to the solar heating and related vertical/horizontal mixing, diffusion, and turbulence, usually the PBL is thicker during the daytime or in warm weather. The height of PBL can reach 3 kilometers but its upper surface is often not well defined. Above the PBL is the free atmosphere.

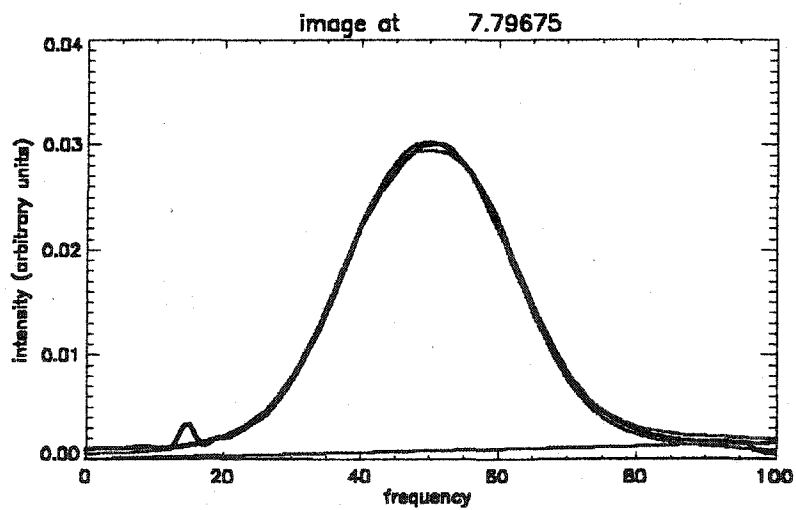
One characteristic of the PBL is that it is turbulent, as compared to the troposphere above it. But the most important feature of PBL for lidar measurements is

that it has a much greater aerosol concentration that attenuates the backscattered lidar signals. The aerosol extinction coefficient is normally 30 to 40 times larger than the molecular extinction coefficients. On the other hand, one can also use the aerosol signal at low altitude to measure line-of-sight wind velocity.

For the wind measurements, the existence of an aerosol signal in the molecule signal might not be bad if we can separate them apart because aerosol signal can help to calibrate the molecular signal; the line-of-sight velocities from aerosol signal and molecular signal should be the same. As we know, the aerosol backscattering spectra, a Gaussian in most cases, is much narrower than the molecular RBS spectra and we can "model out" the aerosol component. In doing so, we can also obtain the aerosol/molecular ratio of the air, which can be used in other atmospheric studies. However, when the mixed aerosol/molecular signal is broadened by the instrument, it is more difficult to separate them.



(a)



(b)

**Figure 4.7 Measured RBS spectrum with little (ignorable) aerosol signals. Blue solid line is the fit of kinetic S6 model. Black solid line is the measured RBS spectrum. Pink lines are the molecular, aerosol, and background components. (a) Aerosol signal is large. (b) Aerosol signal is very small (ignorable).**

#### 4.4 Modified Hydrodynamic Model

We know that Brillouin peaks, or Brillouin doublets, in the hydrodynamic regime, are displaced from the central Gross line of RBS spectra by  $\frac{2v_s}{c}$  times the incident light frequency, where  $c$  is the light speed and  $v_s$  is the velocity of sound in the air. All three peaks are Lorentzians and are fully resolved in the hydrodynamic regime. They are not resolved under typical atmospheric conditions in the hydrodynamic model because the sound velocity in the air is small compared to its counterparts in water or dense gases. Furthermore, in the kinetic regime, the hydrodynamic model cannot be used because the mean free path of the air molecules and incident light wavelength are comparable or of the same order. Therefore the resulting Rayleigh-Brillouin scattering spectrum is not simply three lines--a sum of two Brillouin lines and the central Gross line with their widths being determined by the thermal conduction and acoustic attenuation coefficients for air in the hydrodynamic regime, but it is just one complex Rayleigh-Brillouin line. It turns out that the three-line hydrodynamic solution is just the first order expansion the kinetic solution that can be used in our analysis. The physics image here is hence not so clear as it in the hydrodynamic model, but is blurred by many superposed terms. However, as we have shown in chapter 3, despite the first order expansion, higher-order terms are all expanded upon the Brillouin lines although these terms are not necessarily symmetric themselves. We also know that in the kinetic regime, the Landau-Placzek ratio—the ratio between central Gross line and Brillouin doublets—is not fixed. It varies with the temperature, pressure, and other atmospheric parameters. For this reason, we employ a modified hydrodynamic model consisting of three Lorentzian peaks, as in the



ideal hydrodynamic model, but their amplitudes as well as their widths--determined by thermal conduction and acoustic attenuation coefficients of the air--are variable. The use of a modified hydrodynamic model is based on the philosophy that if a hierarchy of models, from simple to complex, can be used for understanding and predicting atmospheric behavior, in some occasions, the simpler model provides direct insight into physics and some important properties of the atmosphere.

The modified hydrodynamic model (MHM) is illustrated in figure 4.8. The frequency of the central Gross line is unchanged. Two Brillouin lines are displaced by twice of the sound velocity of the air from the central Gross line. The amplitude and widths for all three lines are adjustable when the model is fit to the data. Since the widths are related to the thermal conduction and acoustic attenuation coefficients as well as thermal relaxations, it is of interest to see how these coefficients vary with altitude.

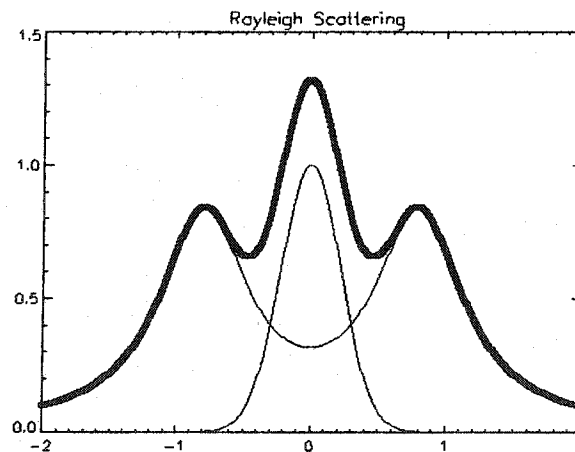


**Figure 4.8** The modified hydrodynamic model. Three Lorentzian lineshapes are overlapped and their superposition is shown as the thick black line. The displaced length is determined by the sound speed of the air molecules

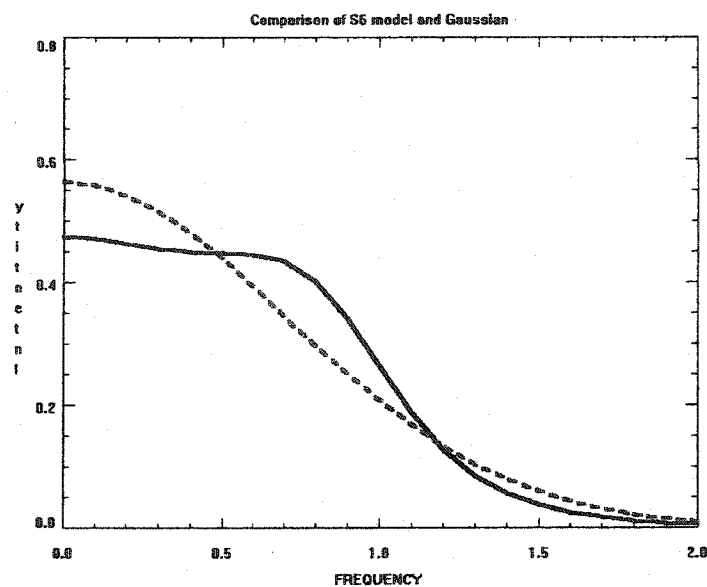


**Figure 4.9** Shown above is the kinetic model. The white line is the S6 kinetic model is compared with a Gaussian.

#### 4.5 Tenti's S6 Model and Temperature Profiling

Tenti's S6 model has been widely accepted as the best model by most lidar researchers. The model was proposed in 1974 and was tested in under different circumstances (May 1975; Lao 1976; Sandoval 1976; May 1980). Laboratory results agree well with the theoretical S6 model in the hydrodynamic regime and intermediate part. However, in the pure kinetic regime, there were discrepancies between the model and laboratory results (Sandoval 1976). The kinetic model depends on two dimensionless parameters  $x$  and  $y$  as we mentioned in last chapter. Temperature and pressure of air molecules are combined in the  $y$  parameter. An empirical formula is calculated from the standard air model for parameter  $y$  in S6 model, which takes the form

$$y = 0.2308 \times (T + 110.4) \frac{\lambda P}{T^2} \quad (4.8)$$

From the above formula, even if pressure and temperature are changed, it is possible to have  $y$  unchanged. This means it is difficult to determine the temperature and pressure simultaneously only by experiment. On the other hand, we can easily see that when temperature is extremely high or pressure is very low,  $y$  approaches to zero and the model will be approximately a thermal-broadened Gaussian. It can be easily understood. When the temperature is extremely high or the pressure is very low, the motion gas molecules are totally random. Neighboring molecules do not impose any effects on single molecule's motion.

To evaluate the performance of the kinetic S6 model for the air, we must verify two things: first, we must compare the S6 model to a measured clean Rayleigh-Brillouin backscattering spectrum of the air; second, probably more important and useful in real application, is to test the kinetic S6 model performance on real atmospheric properties, such as the temperature profile in the air. That is, the change of S6 model over the altitude--so temperature and pressure change in S6 model--should agree with the measured Rayleigh-Brillouin backscattering spectra at different altitude. In another words, if we use the kinetic S6 model to fit to the GroundWinds data to retrieve a temperature profile and it agrees with the temperature profile from radiosonde or balloon data, this suggests we have a fairly good model. The first verification method is to ensure the shape of the kinetic S6 model agrees with that of measured RBS spectra. The second verification is to ensure the inherent nature of S6 model--the change of the model over the gradual temperature and pressure change in the air--is correct. The laboratory experiments so far have done only the first kind under higher pressure ( $>1\text{atm}$ ).

Altogether, if we can retrieve a correct temperature profile to assure we have a good RBS model, then this will remove a source of systematic error in a wind measurement: the main goal for the GroundWinds instrument. Conversely, if we cannot retrieve a good temperature profile, this implies that the shape is not correct and one should use a better model when fitting data to avoid the introduction of more errors.

#### 4.6 Landau-Placzek Ratio

Landau and Placzek (Landau 1934; Landau 1985) found that for Rayleigh-Brillouin scattering the ratio between the intensity of Brillouin doublets,  $2I_B$ , and the intensity of the unshifted Gross line,  $I_R$ , is fixed and is

$$\frac{I_R}{2I_B} = \gamma - 1. \quad (4.9)$$

where  $\gamma$  is the ratio of specific heats.

Although many (Yip 1967; Yip 1971; Young 1982) claimed this relationship (4.9) holds for both the hydrodynamic regime and the kinetic regime, it has not been supported by experiments (O'Connor 1975) or by theoretical calculations of thermal relaxation theory (P. C. Wait 1996; Fabelinskii 1997). Equation (4.9) is derived from a group of hydrodynamic equations with standard assumptions; the most important being that the scattering medium does not absorb heat, i.e., sound transport is adiabatic. In reality, the Landau-Placzek ratio is close to  $\gamma - 1$  even in the hydrodynamic regime.

It is a different case in the kinetic regime. First, in the kinetic regime, the Rayleigh-Brillouin scattering spectrum does not display three clear lines as it in the hydrodynamic regime. The Brillouin lines and the unshifted Gross line are unresolved.

Therefore, there is no way to accurately retrieve the Landau-Placzek ratio directly from the RBS spectrum. Second, thermal broadening effect (the cause of unshifted Gross line) is becoming relatively more intense compared to acoustic fluctuations (the cause of Brillouin scattering) as the scattering gas medium gets thinner. Thus, the Landau-Placzek ratio will deviate from  $\gamma - 1$  when in the kinetic regime.

## 4.7 RBS Spectra and Temperature Profile

### 4.7.1 Rayleigh Spectra

The data to be analyzed were taken during the AirMap campaign on July 31, 2002. It was a typical sunny summer day and the data had been taken continuously over the entire day. Every two-hour data set was recorded. Three datasets were chosen for data analysis. They were taken at 3:40am, 5:40am, and 7:40am respectively. The integration time for the measurements is 10 seconds. The aerosol level above the boundary layer is normally lower than at any other time in a day before sunrise. On this specific day, radiosonde data were also taken at 12:00am and 12:00pm respectively. The corresponding aerosol and molecular signal strength at different altitudes are shown in figure 4.10 and 4.11. The color bar indicates different photon intensities. For both of them, yellow stands for the highest photometric return (greater than  $10^7$  photons) while blue stands for the lowest photometric returns (lower than 100 photons). One can see that the planetary boundary layer (PBL) is formed just above the ground and extends to an altitude of approximately two and a half kilometers thick. The aerosol level is weak above the PBL. For the molecular channel, the photometric return attenuates as the altitudes increases. At 15km, the photometric return is less than 100. For the sake of data

analysis of molecular Rayleigh-Brillouin scattering spectra, we will put the emphasis on the data whose corresponding altitudes are above the PBL and below 15km.

The main interest of this research is the measured Rayleigh-Brillouin scattering (RBS) spectra. Basically the real air is not in local thermodynamic equilibrium (LTE) and the scattering itself is an example of non-local thermodynamic equilibrium. For this reason, in addition to temperature, many atmospheric properties are reflected in the RBS spectra, such as thermal conductivity, viscosity, and turbulence. Therefore the RBS spectra in the air could be a useful tool in related atmospheric researches.

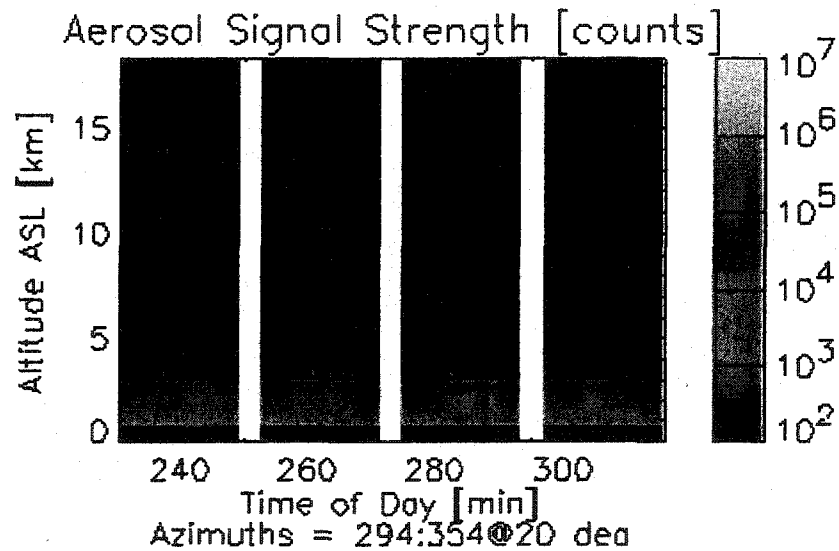


Figure 4.10 Aerosol signal strength

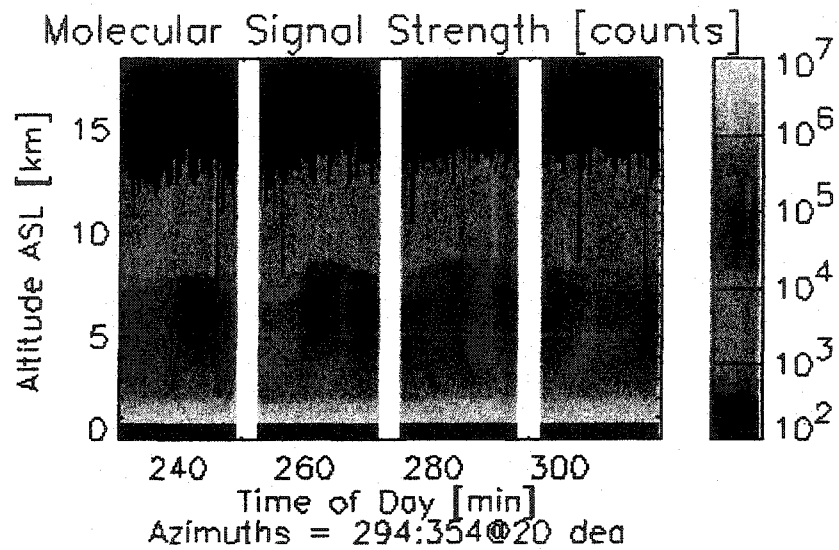
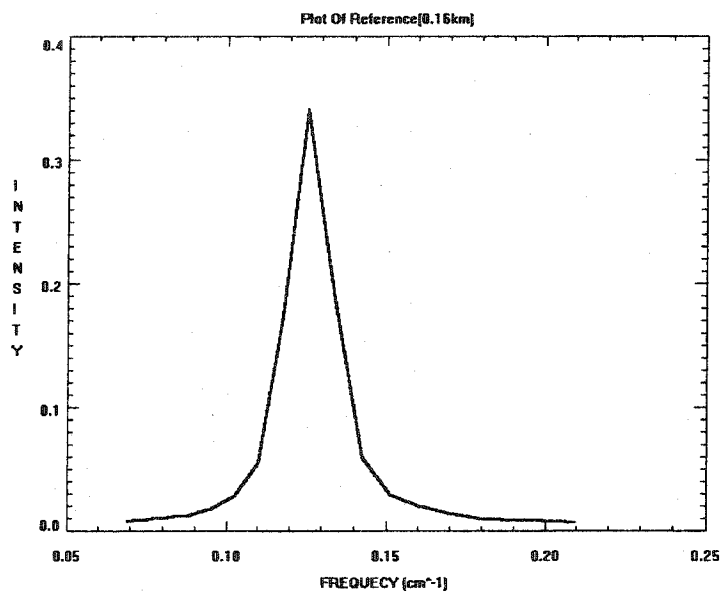


Figure 4.11 Molecular signal strength

A measured RBS spectrum is plotted in figure 4.13. The associated reference signal is also shown in figure 4.12. The reference signal embodies all broadening effects of the instrument, provided the laser line width is negligible (ref. Table 4.3). We can then apply the inverse method discussed in the former chapter to remove the instrumental broadening from the measured RBS spectrum. However, care must be taken when removing the broadening effects. We cannot remove the entire reference signal from the RBS line, only part of it. The reason lies in the fact that, first, the measured RBS lineshape is not perfectly symmetric—as we have argued earlier; second, the spectrum might be overhauled or over-deconvolved by taking off the whole reference signal since the resolution of the data was not high enough besides the laser has a small width. To avoid this, we have chosen to remove a Lorentzian broadening effect with a width that,

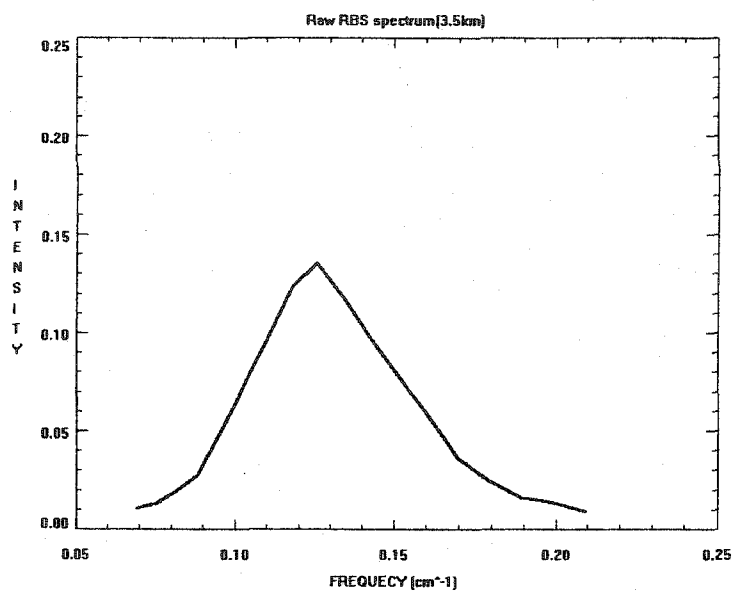
after the removal of broadening effects, there was only one non-zero data point in the deconvolved reference signal (figure 4.15 ).

Figure 4.14 and 4.15 illustrate the measured Rayleigh-Brillouin scattering spectrum after we removed the instrumental broadening effects. The temperature when the data were taken was 280K as measured by a RadioSonde. The altitude was 3.5 kilometer. Pressure was 0.8 atm from the standard model.



**Figure 4.12** A plot of reference fringe





**Figure 4.13** A plot of raw fringe. The corresponding altitude is 3.5 km

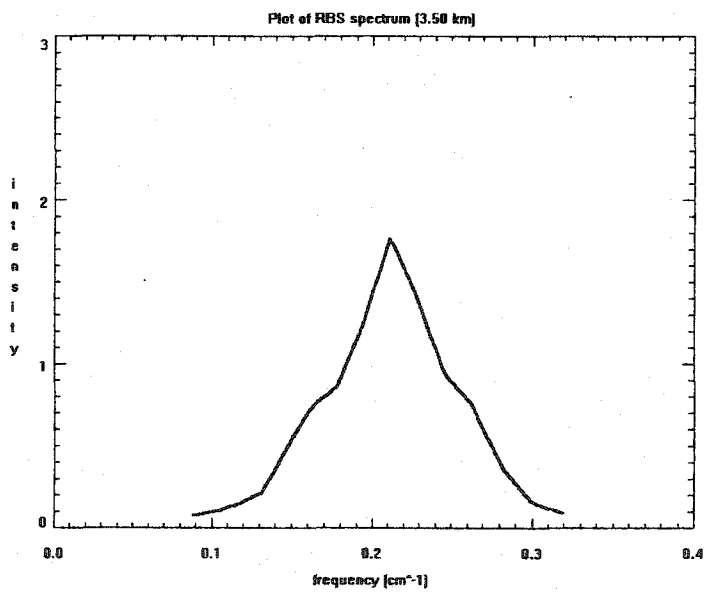


**Figure 4.14** One deconvolved Rayleigh-Brillouin scattering spectrum

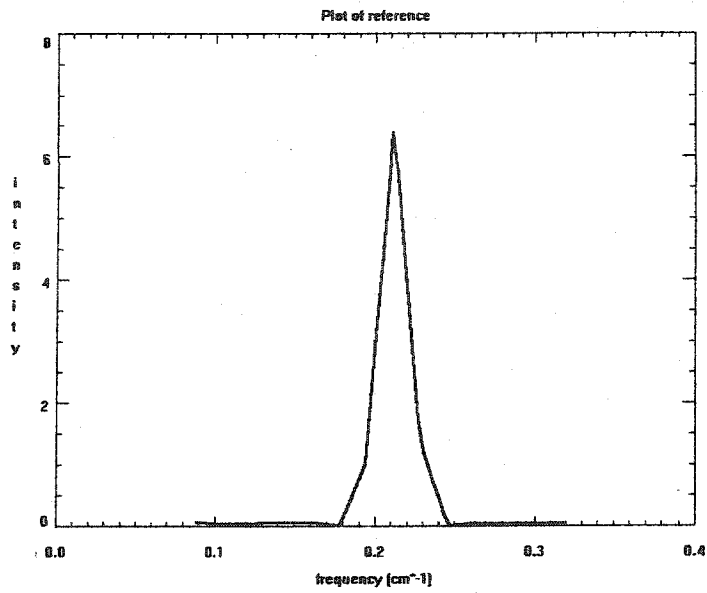


**Figure 4.15 Deconvolved Rayleigh-Brillouin scattering spectrum(upper) and deconvolved reference signal (down)**

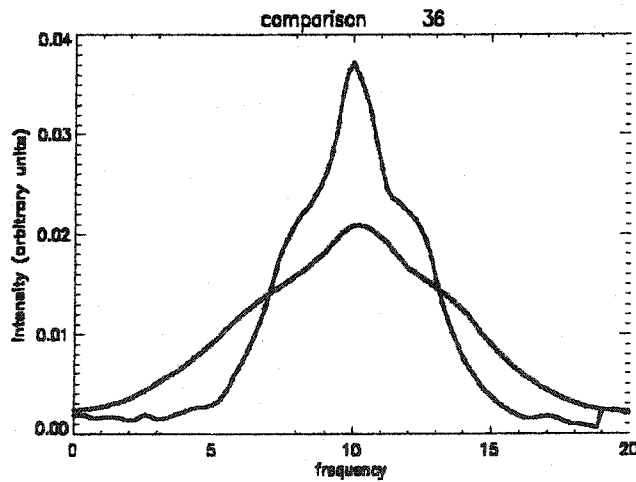


**Figure 4.16 Comparison of raw RBS fringe and deconvolved RBS spectrum.**

Although it is difficult to resolve the Brillouin peaks from the measured RBS spectrum (figure 4.14), the sound velocity can still be derived from the RBS spectrum by measuring the Doppler shift between two Brillouin side bands. From gas dynamics, velocity of sound is given by,

$$v_s = \sqrt{\frac{\gamma RT}{M}} \quad (4.10)$$

where  $\gamma$  is the specific heat ratio,  $R$  is the universal gas constant,  $T$  is the temperature and  $M$  is the molar mass of air. For  $T=300\text{K}$ ,  $\gamma=1.4$ ,  $R=8.31 \text{ JK}^{-1}\text{mol}^{-1}$ ,  $M=0.029 \text{ Kg/mol}$ , we get  $v_s \approx 330 \text{ m/s}$ . Since the Brillouin peak is shifted by twice the sound velocity in a RBS spectrum, this corresponds to a wave number separation of

$$\frac{2v_s}{c\lambda} = 0.04347 \text{ cm}^{-1}$$

Here  $\lambda$  (532 nm) is the incident light wavelength and  $c$  ( $3 \times 10^8 \text{ m/s}$ ) is the speed of light.

From figure 4.14, by fitting the modified hydrodynamic model to the RBS spectrum, the distance between two side lobes is approximately  $0.09 \text{ cm}^{-1}$ . From above analysis, it corresponds to a sound velocity of  $350 \text{ m/s}$ . This is slight larger than one could compute from the temperature and pressure. However, from the thermal relaxation theory, the Brillouin parts will be pushed outwards by the effect of thermal relaxation. It happens too in the hydrodynamic regime (Mountain 1966). It can also be seen in Tenti's S6 model when Brillouin peaks can be singled out (ref. Fig 3.3).

In figure 4.17, the difference between thermal broadening effects, which displays as a Gaussian, and the corresponding Tenti's S6 model under same atmospheric conditions (300K, 1 bar) is plotted. Compared to the Gaussian, there are two symmetric

side lobes on the shoulders of the S6 model. These two parts are significant in the temperature profiling and wind measurements. Shown in figure 4.18 are two plot of S6 models at same atmospheric conditions that only differ in temperature by 40 K. The temperature difference between the black solid line and the blue dashed line is 40K. It is straightforward that a 40K temperature change induced difference of S6 models in figure 4.18, compared to the difference between S6 model and pure thermal broadening Gaussian in figure 4.16, is rather small.

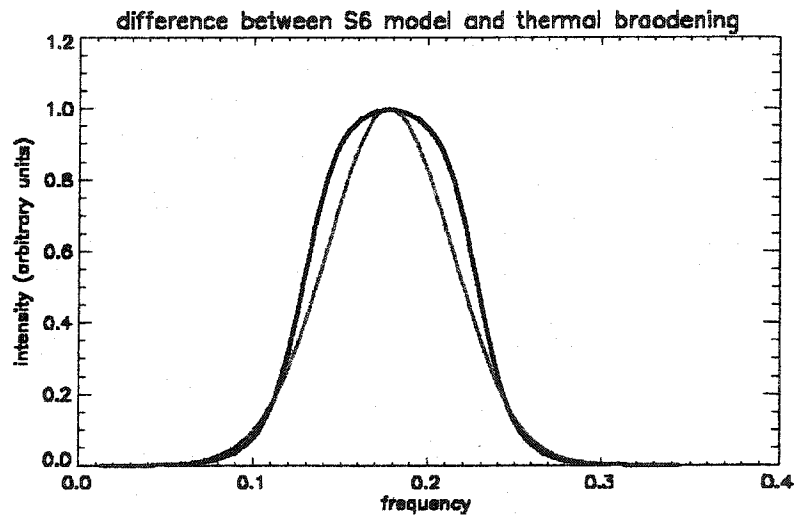


**Figure 4.17 Comparison of S6 model and a thermal broadening Gaussian. They are plotted under same temperature**

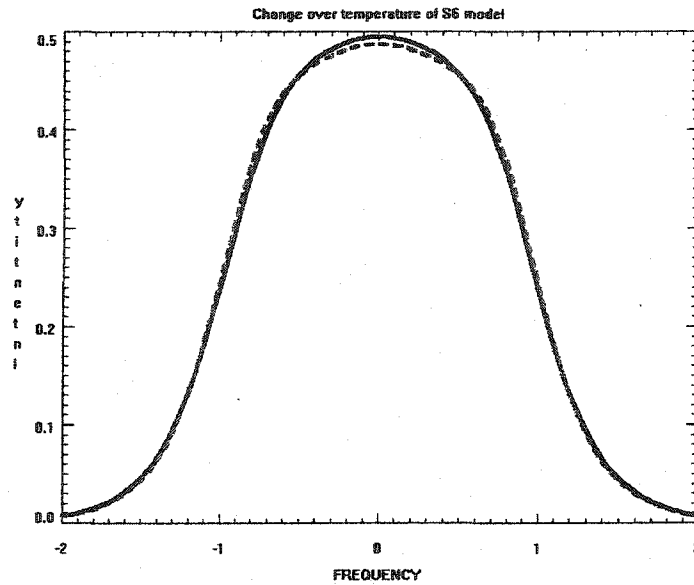


**Figure 4.18** Plot of S6 model at same atmospheric conditions except the temperature. Black solid line corresponds to a temperature 300K while the blue dash line corresponds to 260K

The Landau-Placzek ratio will not be a constant for the Rayleigh-Brillouin scattering in the atmosphere as it is in the hydrodynamic regime. Using the modified hydrodynamic model, we can measure a Landau-Placzek ratio profile as a function of altitude.

Figure 4.19 shows the changes of the Landau-Placzek ratio as a function of altitude. Lower than 4km, the aerosol signal is fairly strong. It is difficult to remove the all the aerosol signal so we will ignore this part in our discussion. Above 4 km with increasing altitude, the ratio decreases as the temperature drops. This means the Brillouin components induced by pressure fluctuations are shrinking while the centered Rayleigh component, broadened by thermal effects, is growing. In the free streaming limit, i.e., when the scattering gas medium is dilute, the Landau-Placzek ratio approaches zero as the Rayleigh scattering induced by thermal motions of air molecules dominates.

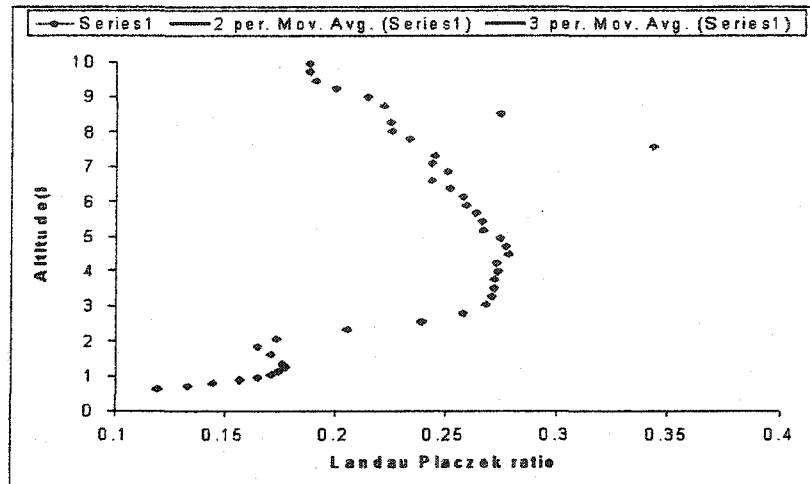


**Figure 4.19 Landau Placzek ratio vs. altitude (km)**

#### **4.7.2 Temperature Profile**

Figures 4.20 and 4.21 are measured temperature profiles obtained from one-day data we have been using in this chapter using the kinetic S6 model. In the retrieval of temperature profile, pressure was calculated from the US Standard Atmosphere 1976. The measured temperature profiles are compared to the temperature profile from a RadioSonde launched 2 hours before the data were taken. Each profile in figures 4.20 and 4.21 corresponds to an integrated data subset of 7 minutes. Multiple temperature profiles, which are retrieved from a series of consecutive 7-minute integrated data, are shown in figure 4.20 with a single 7-minute integrated temperature profile is shown in figure 4.21. In figure 4.23, two fitting plots at different altitudes show the molecular part and aerosol part are separated from the backscattered RBS spectra and the kinetic S6 model was

employed in those fittings. The molecular part was separated from the measured fringe using S6 model hence the aerosol return can also be estimated. The pink line stands for the molecular part and purple line is the aerosol signal. The fitting applies the model to the raw RBS fringe, which includes all the broadening effects. Therefore, the separated molecular spectra in both plots in figure 4.21 are broadened. A temperature profile can also be retrieved from deconvolved RBS spectra. However, the inner nature of deconvolution method determines that its performance is affected when the signal noise ratio is low, although it may give better results when backscattered signal is strong. This can be seen from figure 4.21.

We can tell from these plots that the temperature profiles retrieved from GroundWinds data agree with the radiosonde, though there is a time gap between launch of the radiosonde and lidar measurements; the temperature from the GroundWinds data are systematically off by 5-10K higher. However, the lapse rate is approximately the same. Most importantly, the turning point of temperature, an indicator of end of the troposphere, is clearly shown in our measured temperature profiles, given the backscattered signals at this altitude are relatively weak and degraded.

It is exciting that the temperature measurements offer us a chance to measure other air quantities and ongoing processes. Despite instrumental broadening effects and other impact factors from measurements, turbulence and other latent energies could also affect the Rayleigh-Brillouin scattering spectra in the air. For example, in figure 4.21, which contains just one temperature profile from GroundWinds data, shows considerable scatter. These fluctuations may be statistical or due to some real physical motions (air pockets, turbulence, etc) in the air. One efficient and practical way is to have more

consecutive measurements. From figure 4.20 that contains multiple temperature profiles, we can see a strong indication that these fluctuations are real because all these temperature profiles are varying in a repeatable way. We can then study these fluctuations to retrieve other air quantities or investigate other processes such as wind turbulence and sound propagations. The effects of an external force to the Rayleigh-Brillouin scattering spectra will be studied in chapter 6.

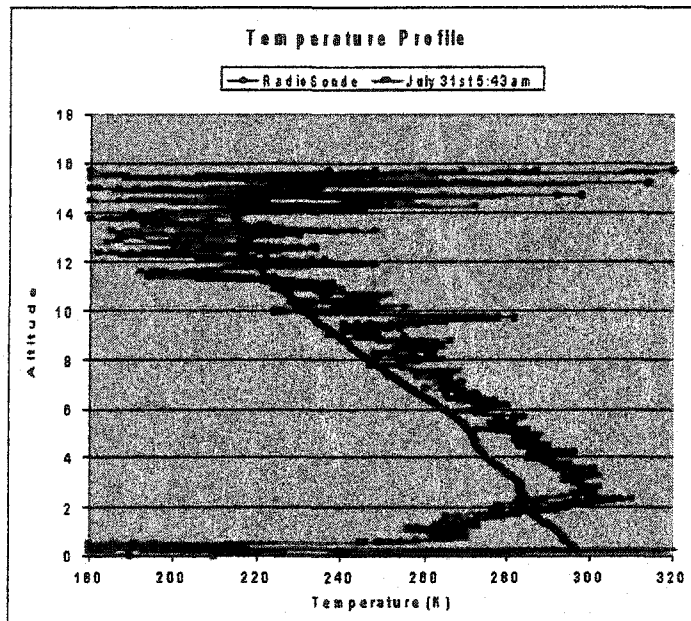


**Figure 4.20 Retrieved temperature profile at 6:00am on July 31<sup>st</sup>, 2002**



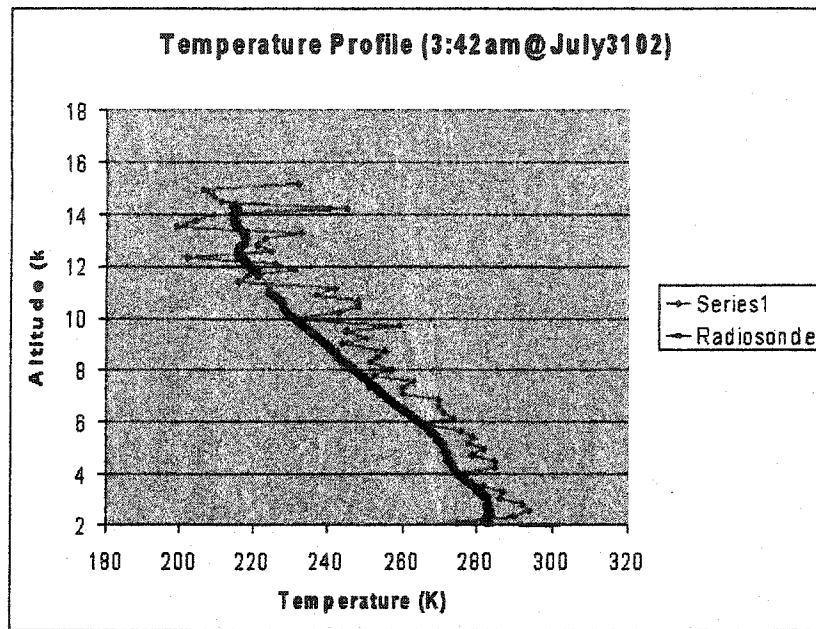
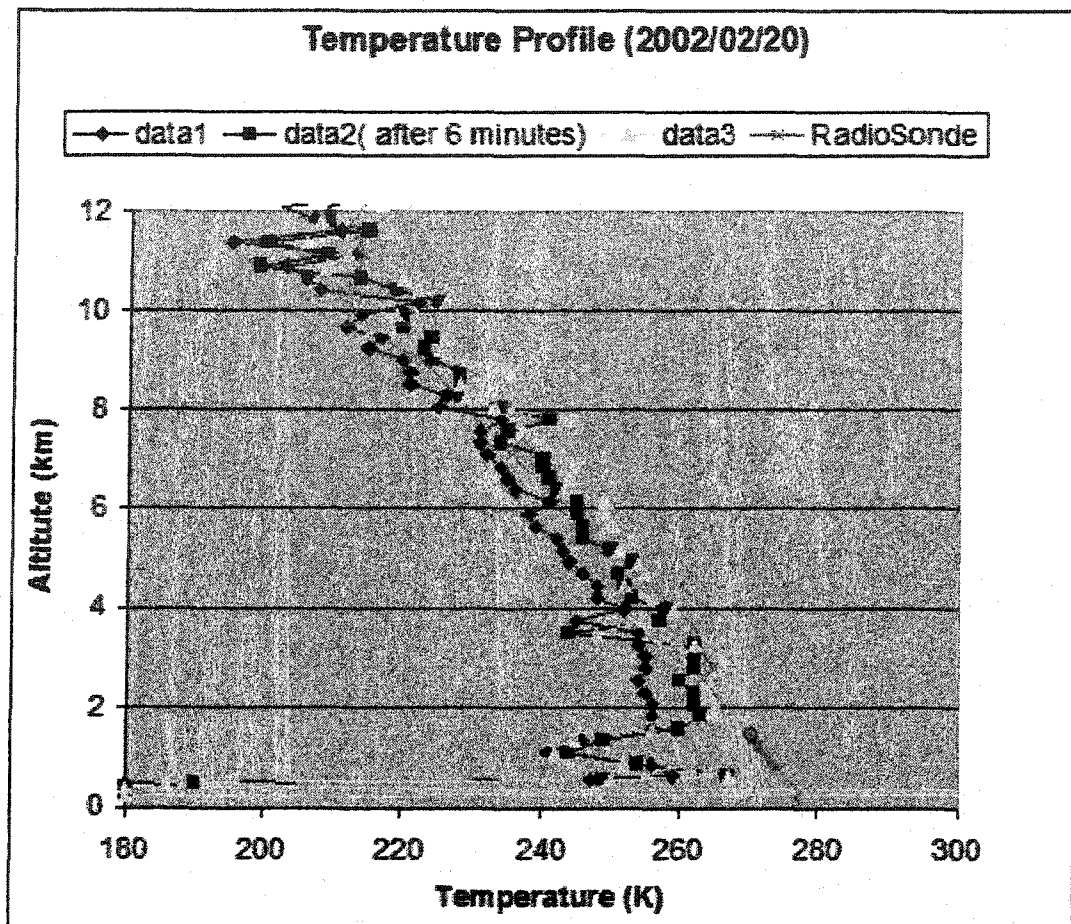
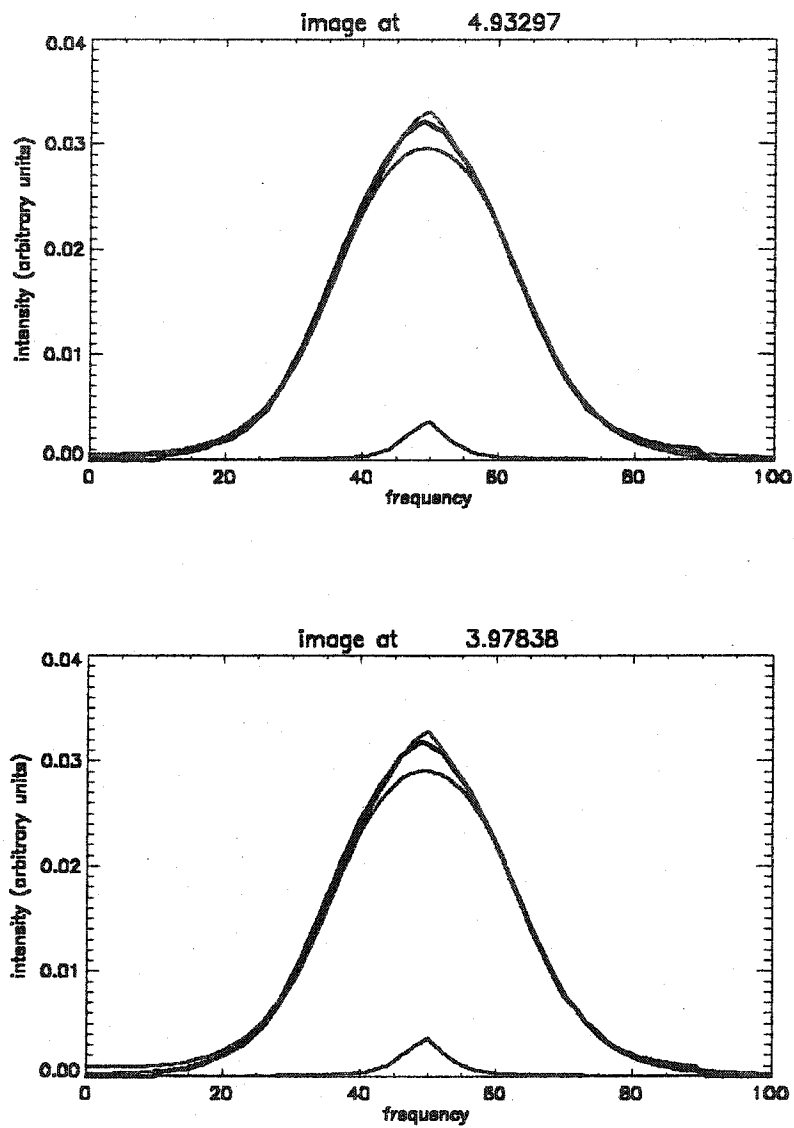


Figure 4.21 Retrieved temperature profile from RBS raw fringe at 4:00am on July 31<sup>st</sup>, 2002



**Figure 4.22 Retrieved temperature profile from deconvolved RBS spectra. The data was taken on Feb 20, 2003 at 2:15am EST**



**Figure 4.23 Fit the kinetic S6 model to the measured RBS fringe. The black solid line is the raw RBS spectrum, the red line is the molecular part and purple line stands for the aerosol part. The upper fitting image is corresponding to an altitude of 4.93 km and the lower is corresponding to an altitude of 4km**

The main interest in temperature profiling is to see how it reflects the Rayleigh-Brillouin scattering spectra in the air. From the temperature profiling, the kinetic S6 model is much better than another common used model—a Gaussian with its width determined by thermal motions of air molecules. The difference between these two models was given in figure 4.17. Such a difference among the models leads to large errors in the temperature measurements particularly at higher altitudes for lidar measurements. It is possible that a temperature profile up to 5 km high could be measured using the thermal broadened Gaussian model (G. Fiocco 1971; Schwiesow R. 1981)—given a good calibration to the measured temperature, because different kinds of errors could be overlooked. The problems can be easily seen when the measurements are extended to 15 kilometers into the stratosphere. At a matter of fact, we know from the kinetic theory that the temperature cannot be measured by an assumed Gaussian lineshape. The temperature measurement is very sensitive to the Rayleigh-Brillouin lineshape, as we can tell from figure 4.17 and 4.18. Compared to the thermal broadened Gaussian, the kinetic S6 model gives a much better lapse rate besides providing a good fit to the measured RBS spectrum. This was also displayed in the Landau-Placzek ratio plot in figure 4.19. The Brillouin proportions are shrinking when the air is getting thinner. That makes the width of the Rayleigh-Brillouin scattering spectra not proportional to square root of temperature as it in thermal broadened Gaussian model.

However, despite the fluctuations and aerosol effect in the lower atmosphere, there are still differences between the temperature profile given by radiosonde data and measured temperature profile from GroundWinds data, and between the measured Rayleigh-Brillouin scattering spectra and the kinetic S6 model. The prerequisites of the

kinetic S6 model is that the scattering is polarized, which means it requires the backscattered signals are in a same polarization plane with that of incident photons from the laser transmitter. Since there is a small part (1~3 %) of backscattered photons are depolarized (polarization direction is changed) during the single scattering process, and this part will not account for the Brillouin part from chapter 3 by kinetic theory, this will make the central Rayleigh line or Gross line have a larger intensity than what it is with pure polarized Rayleigh-Brillouin scattering. In addition, how the inter-diffusion between two main gas species occurs is still unknown. Altogether, it would be interesting to measure 'pure' polarized Rayleigh-Brillouin scattering in the air in the future on the GroundWinds incoherent lidar systems.

#### **4.7.3 Temperature Bias Caused by Non-Uniform Lidar Returns**

The photometric returns of the lidar system decreases with altitude. For GroundWinds NH lidar system, depending on how often the backscattered photons register on the CCD, it bins one-quarter kilometer data vertically so that we have approximately four data points for every kilometer. On the other hand, the temperature drops with altitude. Therefore, for one bin data corresponding to one specific altitude, the temperature retrieved from it will be slightly larger than it should be because this non-uniform photon distribution at different altitude.

The temperature shift caused by the non-uniform photon returns at different altitude can be calculated using the lidar equation (chapter 5),

$$T - T_0 = \frac{\int_0^{0.5} dr T(r) \frac{1}{r^2} \beta_m(r) e^{-2\delta(r)}}{\int_0^{0.5} dr \beta_m(r) e^{-2\delta(r)} \frac{1}{r^2}} - T_0$$

If we assume the real lapse rate of air is around 9.0K/km, then we can roughly get the temperature is systematically shifted up by about 2.0~3.5 K. Calculated temperature biases caused by non-uniform lidar returns from GroundWinds data are shown in Figure 4.24.

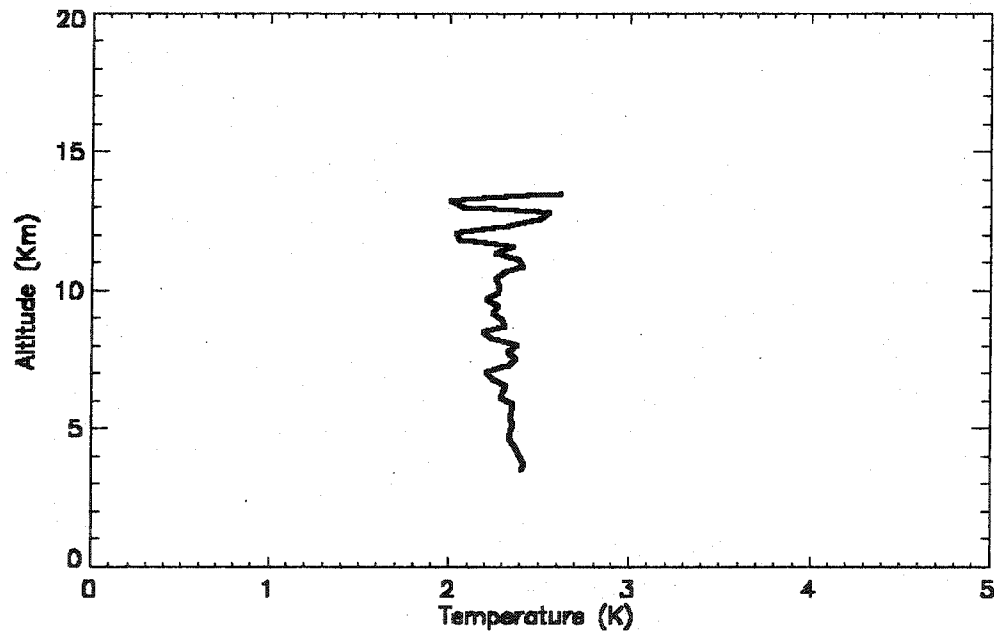


**Figure 4.24** Temperatures are biased up by the non-uniform distribution of photometric returns at different altitude

## 4.8 Discussion

The kinetic S6 model is considered the best Rayleigh-Brillouin scattering (RBS) model for the atmospheric studies. However, with no measurement verification for the real air, it is unconvincing and possibly misleading for its use in many ongoing atmospheric studies. With GroundWinds lidar measurements, for the first time, we were able to compare the measured high-resolution Rayleigh-Brillouin scattering spectra to the kinetic S6 model. In addition, for the reasons that we explained in this chapter, temperature profiling from the measured RBS spectra is necessary for the verification of S6 model. Measured RBS backscattering spectra in the air were shown and compared to the current model. By using the kinetic S6 model, we have successfully retrieved the temperature profile from GroundWinds lidar data products. It was shown that the kinetic S6 model has a much better performance than a simplified thermal broadening Gaussian model.

Although the kinetic S6 model has shown itself to be the best model so far to describe the Rayleigh-Brillouin scattering spectra in the air, the comparison of it with the measured molecular backscatter spectra as well as the temperature profiling in the air still shows that there is room for the S6 model to be improved. Almost all the temperature profiles, summer and winter, show larger lapse rates. It is also straightforward to see that the side lobe of spectra is lower than in the kinetic S6 model.

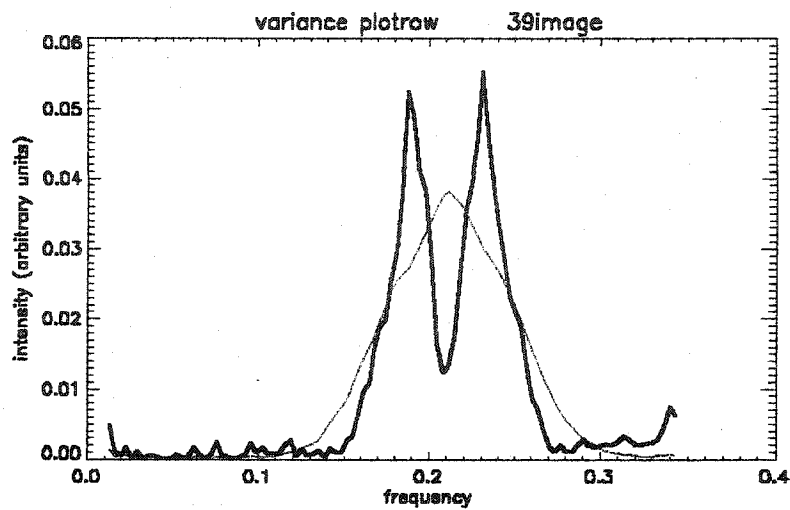
The GroundWinds lidar systems have shown they can be used to measure many other air quantities in addition to its main goal is wind measurements. Through the measurement of temperature profile, we can retrieve other atmospheric properties and

quantities like wind turbulences and other latent energies. Variance analyses can help us to study the turbulence and wind retrieval. Two plots are shown in figure 4.25. They reveal that a much stronger wind at 10:00 am on that day than 6:00am. In addition, as we will show in the next chapter, the molecular photometric returns will help us, for the first time to our knowledge, to measure the Rayleigh scattering backscatter coefficients and extinction coefficients in the real air.

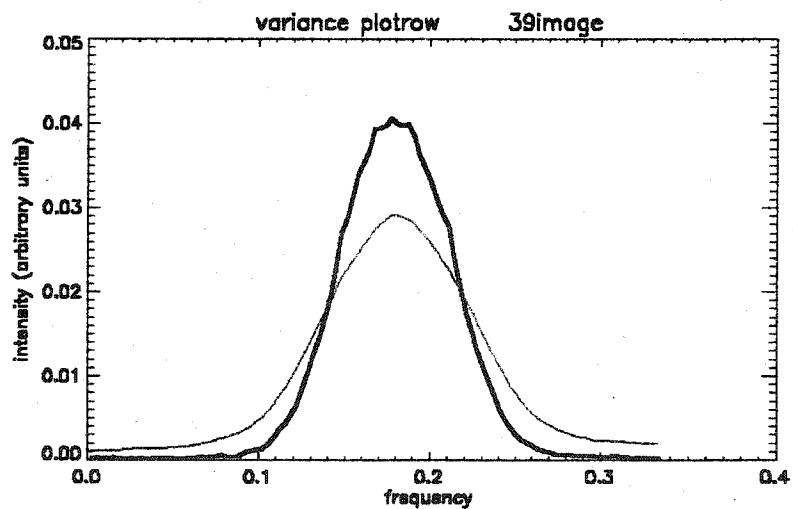
Since the kinetic S6 model was formulated for polarized Rayleigh scattering, as we have shown in chapter 2, it would be very useful and interesting for GoundWinds lidar systems to measure the polarized Rayleigh-Brillouin scattering spectra in the air, not only for the better measurements of winds and temperature as well as other atmospheric quantities, but also for the physical insight of Rayleigh-Brillouin scattering in the air. Related atmospheric studies will benefit from the polarized RBS spectra measurements.

Two variance plots are shown in figure 4.25. These variances were calculated from 40 consecutive measured Rayleigh-Brillouin spectra—corresponding to 7 minutes data—at the same altitude. For example, the altitude for plot (a) is 5.17km (row# 39). The data associated plot (a) was taken on 9:45am EST, July 31<sup>st</sup>, 2002 while that of plot (b) was taken on 5:40am EST of the same day. For case (a), it implies there possibly was wind turbulence at the time the data were taken. The wind turbulence caused large variance on the shoulders of the corresponding Rayleigh-Brillouin spectrum.





(a)



(b)

**Figure 4.25** Plot of variance over 40 consecutive measurements of RBS spectra, they are  
a) a variance plot from data taken at 10:00 EST July 31, 2002 and  
b) a variance plot from data taken at 6:00 EST July 31, 2002

The depolarization ratio is defined as the ratio of the perpendicular and parallel (the same polarization of the incident laser light) polarized photon intensities. It can be written as,

$$\rho_d = \frac{I_{\perp}}{I_{\parallel}}$$

The depolarization process is due to the fact that molecules are not perfect spheres (isotropic). Therefore their polarization coefficient is a tensor. In other words, during the molecular scattering process, the direction of induced dipole is not parallel to the polarization of the incident photons. The depolarization ratio for some gas species of air is tabulated below.

**Table 4.4 Depolarization Ratios for Major Air Species at Various Wavelength\***

Gas species	$\rho_d$ (%)	
	532nm	514.5nm
$N_2$	(1.02 ± 0.02) %	
$O_2$	(2.70 ± 0.10) %	
$CO_2$	(3.91 ± 0.04) %	
$H_2O$	N/A	(0.0299 ± 0.00135) %

\* (Fielding 2002)

The kinetic S6 model does not include the depolarized part of backscattered light. We can see from table 4.4 the depolarized part accounts for approximately 1.3~1.4

percent of the total photometric returns, considering the weights of nitrogen and oxygen in the air. This part of light will increase the temperature that we measured from GroundWinds data because the spectrum of the depolarized broad according to related theories (Tenti, 1976).

## CHAPTER 5

### MOLECULAR BACKSCATTERING COEFFICIENTS IN THE AIR

The GroundWinds lidar system is a fringe imaging direct lidar system that provides twenty molecular channels to describe the entire Rayleigh-Brillouin scattering spectrum. Compared to other incoherent lidar systems, GroundWinds lidar can isolate the molecular photometric returns. This is because the aerosol backscatter width is much narrower than Rayleigh-Brillouin width. That means we have many molecular channels in which only the molecular signal resides. We can therefore use this part data to calculate the molecular backscatter coefficients for Rayleigh-Brillouin scattering in air.

#### 5.1 Lidar Equation and Lidar Ratio

The general lidar equation reads (Klett, 1981, Piironen, 1994),

$$P(r) = E_0 \frac{cO(r)A}{2r^2} \left[ \frac{3}{8\pi} \beta_m(r) + \frac{\rho(\pi, r)}{4\pi} \beta_a(r) \right] e^{-2 \int_0^r \alpha_t(r') dr'}, \quad (5.1)$$

where

$P(r)$  = lidar power incident on receiver from range  $r$ , W;

$E_0$  = laser pulse energy, J;

$c$  = speed of light

$A$  = area of receiver

$\beta_m(r)$  = molecular scattering cross-section per unit volume from range  $r$ ,  $m^{-1}$ ;

$\beta_a(r)$  = aerosol scattering cross-section per unit volume from range  $r$ ,  $m^{-1}$ ;

$\alpha_e(r)$  = extinction cross-section per unit volume from range  $r$ ,  $m^{-1}$ ;

$\frac{\varphi(\theta, r)}{4\pi}$  = aerosol backscatter phase function from range  $r$ ,  $sr^{-1}$  ( $\theta = \pi$  for backscatter);

$\frac{3}{8\pi}$  = molecular backscatter phase function from range  $r$ ,  $sr^{-1}$ ;

$O(r)$  = Lidar overlap function.

The column optical depth  $\delta(r)$  is related to the extinction cross-section by

$$\delta(r) = \int_0^r \alpha(r') dr' \quad (5.2)$$

with

$$\alpha(r) = \alpha_a(r) + \alpha_m(r). \quad (5.3)$$

Here  $\alpha_m$  and  $\alpha_a$  are the molecular extinction coefficient and the aerosol extinction coefficient for air, respectively. Measurements of individual optical properties are not possible with a single channel lidar due to the coupling of extinction cross-section with the aerosol and molecular backscatter cross-sections. However, it can be accomplished with the separation of equation (5.1) into individual molecular and aerosol components,

$$P_m(r) = E_0 \frac{cO(r)A}{2r^2} \frac{3}{8\pi} \beta_m(r) e^{-2\delta(r)} \quad (5.4)$$

and

$$P_a(r) = E_0 \frac{cO(r)A}{2r^2} \frac{\wp(\pi, r)}{4\pi} \beta_a(r) e^{-2\delta(r)} \quad (5.5)$$

respectively; where  $\delta(r)$  was given in (5.2). Multiple scattering and the background contribution have been neglected.

For the photometric return in the molecular channels, the total photometric lidar return at altitude  $r$  is  $P_m(r)$ . However, the aerosol extinction coefficient  $\alpha_a(r)$  must still be included.

The definition of the lidar ratio is the ratio between the extinction coefficient and backscatter coefficient of aerosols layers or clouds. This can be given as

$$S \equiv \frac{8\pi}{3} \alpha_a / \beta_a \quad (5.6)$$

## 5.2 Retrieval of Molecular Backscatter Coefficients and Extinction Coefficients

### 5.2.1 Backscatter Coefficients by Rayleigh Theory

The modern formulation of the molecular scattering cross section per molecule of a gas is (Bucholtz 1995; Hans Naus 2000)

$$\sigma = \frac{24\pi^3 v^4}{N^2} \left( \frac{n^2 - 1}{n^2 + 2} \right)^2 F_K, \quad (5.7)$$

where  $n$  is the refractive index,  $N$  is the molecular density, and  $F_K$  is the King correction factor that depends on the depolarization ratio for the air. For a collection of molecular scatterers, assuming no multiple scattering, the total cross section is (Jackson, 1998),

$$\sigma_{total} = F(\mathbf{q})\sigma. \quad (5.8)$$

$F(\mathbf{q})$  is called structure factor and can be expanded as,

$$F(\mathbf{q}) = \left| \sum_j e^{i\mathbf{q} \cdot \mathbf{x}_j} \right| = \sum_j \sum_{j'} e^{i\mathbf{q} \cdot (\mathbf{x}_j - \mathbf{x}_{j'})} \quad (5.9)$$

where  $\mathbf{q}$  is the vectorial change in wave vector during the scattering.  $\mathbf{x}_j$  is the position of  $j^{\text{th}}$  scatterer.

If we assume that the scatterers are randomly distributed and each individual scatterer is independent from each other, the terms with  $j \neq j'$  give no contribution. Therefore, only the terms with  $j=j'$  are significant and  $F(\mathbf{q})=N$ , the total number of scatterers. The extinction coefficient for a gas is the total cross section, i.e.,

$$\alpha_m = N\sigma = \frac{24\pi^3 v^4}{N} \left( \frac{n^2 - 1}{n^2 + 2} \right)^2 F_K, \quad (5.10)$$

and the backscatter coefficients is

$$\beta_m = \frac{3}{8\pi} \alpha_m = \frac{9\pi^2 v^4}{N} \left( \frac{n^2 - 1}{n^2 + 2} \right)^2 F_K. \quad (5.11)$$

Here,  $\frac{3}{8\pi}$  is the Rayleigh phase function for backscattering. However, Chandrasekhar (1960) showed that it is not exactly  $\frac{3}{8\pi}$ , but is slightly changed by depolarization of the scattering gas molecules. Since the difference is small, we will neglect it in our following analysis.

### 5.2.2 Backscatter Coefficients from GroundWinds Data

A typical molecular channel signal is shown in figure 5.1. Depending on altitude, it has more than twenty molecular channels. The channels correspond to different wave numbers. The counts in each channel represent the molecular backscatter photon intensity at that wave number. For GroundWinds data, the aerosol signal spans 10 channels in the middle part, so we have at least 10 clean molecular channels to use to retrieve the optical properties of the air.



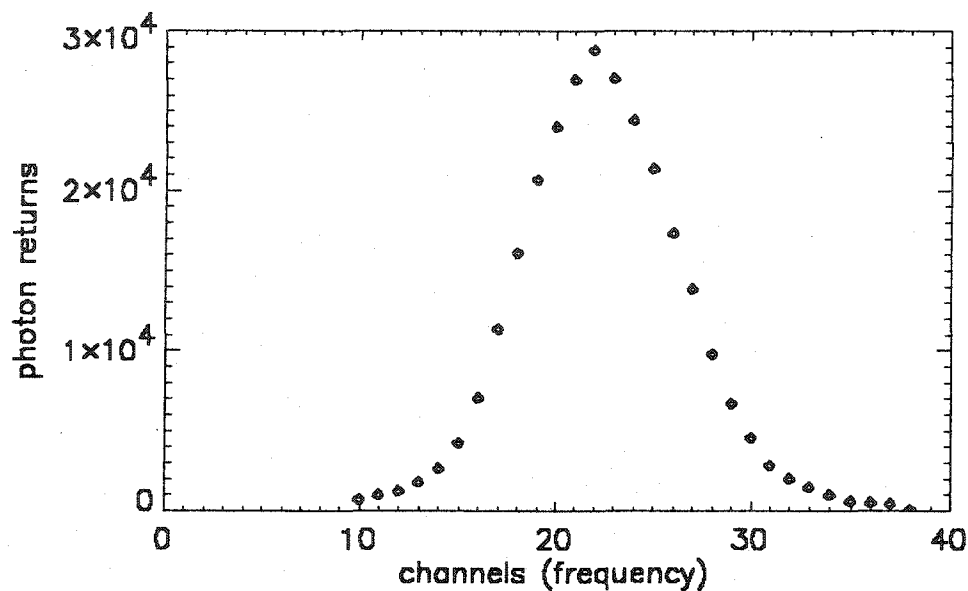


**Figure 5.1 A typical Rayleigh spectrum: photon returns versus different channels**

Because  $\beta_m$  is a coefficient and the integrand of the exponential, the lidar equation (5.1) is nonlinear and must be solved numerically. Klett (1981) proposed a stable analytic inversion method, for the general case, to calculate the aerosol backscatter and extinction coefficients. Fortunately, unlike the aerosol backscatter signal in most cases, molecular backscattering signals are continuous and well behaved. Using the molecular backscattered photon returns of GroundWinds data, we can calculate the molecular backscatter coefficient in a simplified way instead of solving the full lidar equation (5.1).

A molecular photometric return versus altitude is plotted in figure 5.2. This data set was the same dataset that we used in chapter 4 and 5. It was taken around 0600 am EST on 31 July 2002. From figure 5.2, the largest photon return occurs near 1.2 km. From lidar equation 5.4 for molecular returns, the photometric returns at different

altitudes are subject to four major effects: the overlap function  $O(r)$ , the  $\frac{1}{r^2}$  dependence, molecular backscatter coefficients  $\beta_m(r)$ , and the exponential attenuation function  $e^{-2\delta(r)}$ . Except for  $\beta_m(r)$ , the other three functions are rapid varying functions below 4 kilometers. Shown in figure 5.4 is a plot the overlap function  $O(r)$  varying with the altitudes. It can be seen that the overlap function is monotonically increasing and steep below 4 km. So the photometric returns will be increasing first. But with the counter effects of  $\frac{1}{r^2}$  and attenuation loss  $e^{-2\delta(r)}$ , the photometric returns increasing ceases at about 1.2 km. After this, the photometric return is monotonically decreasing with altitude. For the later data analysis, we will use the photometric return data above 4 km since these data are well behaved numerically.

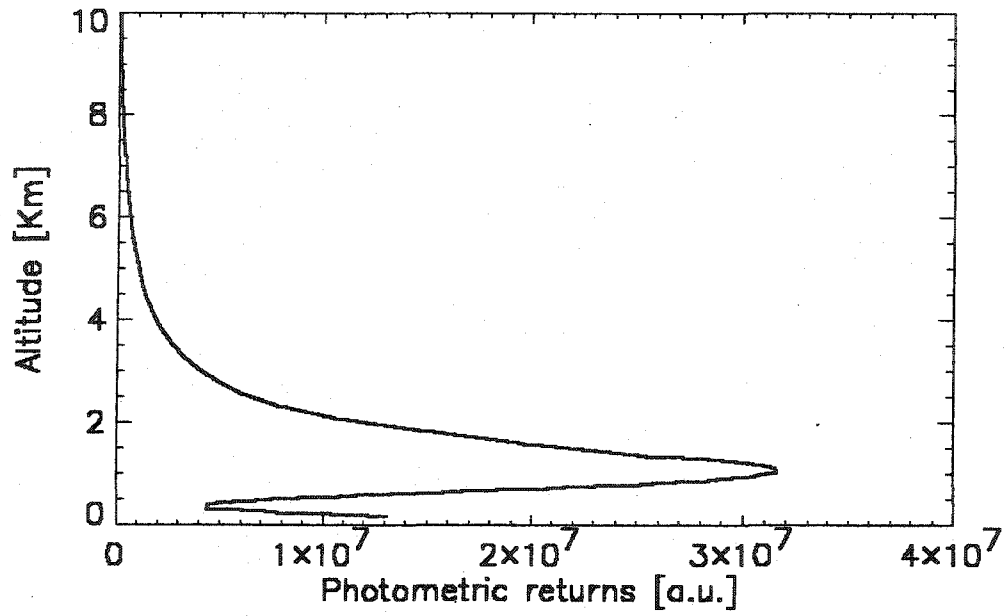


Figure 5.2 One lidar photometric returns of the molecular channels.

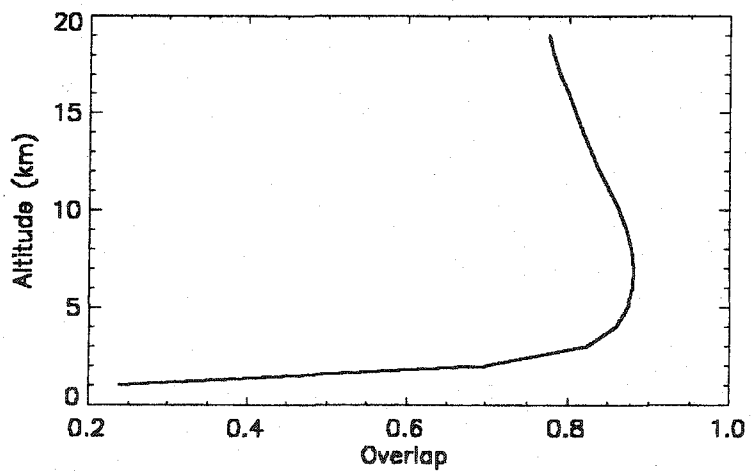
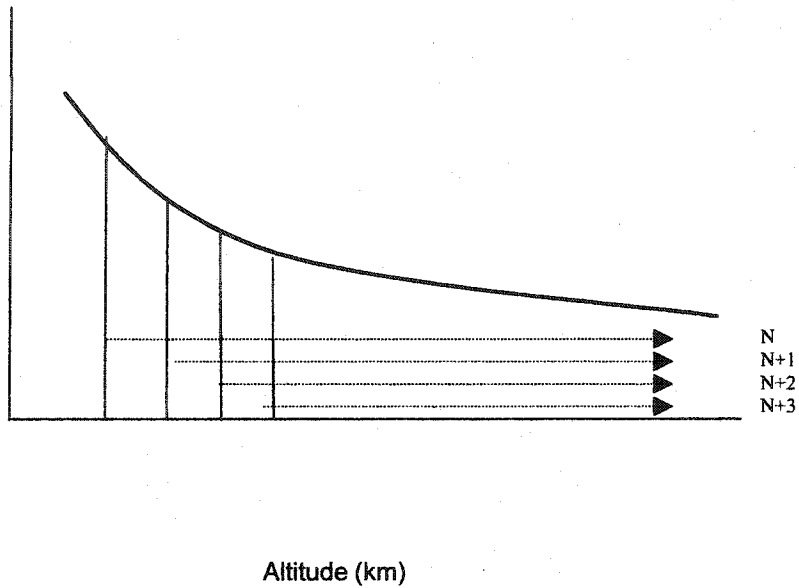


Figure 5.3 the overlap function of GroundWinds NH lidar system.



**Figure 5.4 Fitting scheme.**

For returns above 4 km (figure 5.2), we can retrieve the molecular backscatter and extinction coefficients for Rayleigh scattering using the lidar equation (5.4). First, we manipulate the equation (5.4) leaving the exponential term on the right hand side. It becomes,

$$\frac{16\pi P_m(r)r^2}{cE_0O(r)A\beta_m(r)} = e^{-2\delta(r)} \quad (5.12)$$

With known quantities on the left hand side of equation (5.12), we plot expression (5.12) as a function of altitude and then fit an exponential function to the curve to measure  $\delta(r)$ . From the fitting, we can retrieve the molecular extinction coefficients for

Rayleigh scattering. By (5.11) we know the backscatter coefficients as well. The fitting scheme is illustrated by figure 5.3. For example, suppose we fit it from  $z=2\text{km}$  to infinity, then we fit it from  $z=2.25\text{km}$  and so on. The step length is  $0.25\text{km}$ , which is determined by the binning of the data. Then from each fitting, we can compute the molecular extinction coefficients as well as the backscatter coefficients at different altitudes. The backscatter coefficients versus altitudes are plotted in figure 5.6 and 5.7. For the analysis, the data can be chosen so that the aerosol level is low above the boundary layer.

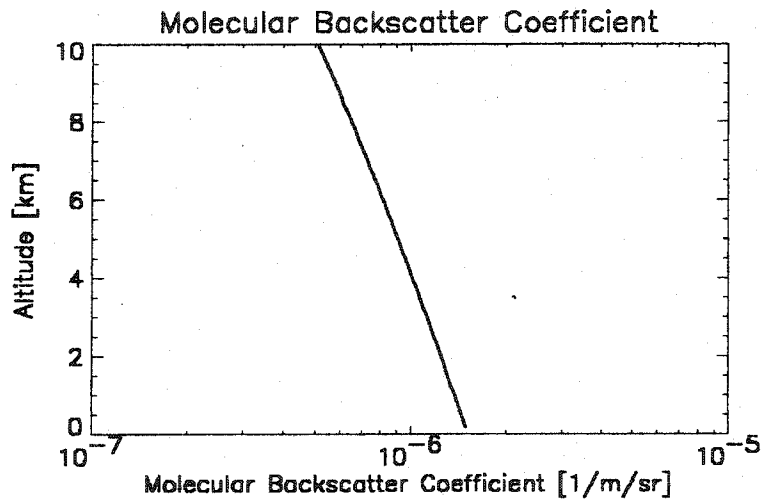


**Figure 5.5 Theoretical molecular backscatter coefficients of air (by eq. 5.11)**

Theoretical Rayleigh (molecular) backscatter coefficients can be computed from equation (5.11). It is a function of the molecular density  $N$ , the refractive index of the air  $n$ , and the incident light frequency, i.e., the laser frequency in our analysis. A plot of theoretical molecular backscatter coefficient for air with altitude is shown in figure 5.5.

Using the slope method described above, we obtained a Rayleigh backscatter coefficient profile of air. It is shown with its theoretical counterparts in figure 5.6. The pink dotted line is the theoretical value and the black solid line represents the measured value. Focusing on the results above 4 km, there is an obvious discrepancy between these two curves: the measured molecular backscatter coefficient is twice as large as the theoretical one.

The possible cause of a larger measured Rayleigh or molecular backscatter coefficients is Brillouin scattering. Brillouin scattering was ignored in the Rayleigh cross-section calculation of the collective effects of air molecules. If we assume, in the Rayleigh cross-section calculation, the weight of the Brillouin scattering of the total Rayleigh-Brillouin scattering can be represented by the Landau-Placzek ratio, we can add this part to the theoretical Rayleigh backscatter coefficients. This is shown in figure 5.7. The purple line is the calculated Rayleigh backscatter coefficients using Landau-Placzek ratio from GroundWinds data. It is still smaller than the measured value but they roughly agree with each other. The blue dotted line stands for the calculated Rayleigh backscatter coefficients using an ideal Landau-Placzek ratio, a constant value of 2.5. The pink dotted line and the black line are the theoretical value and the measured value, respectively, same as in figure 5.6.

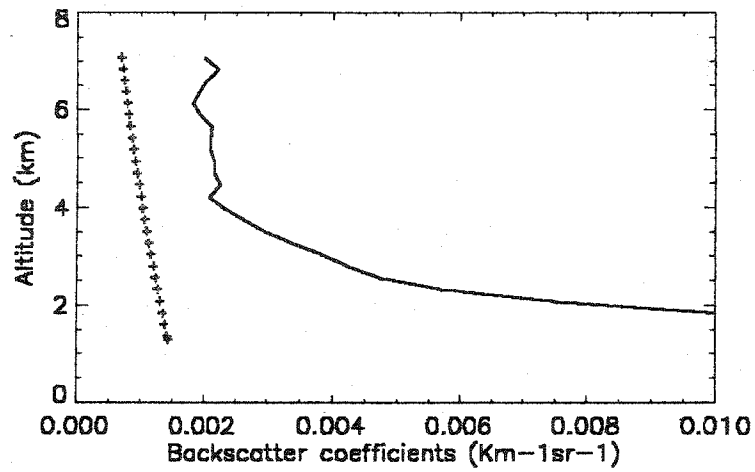


**Figure 5.6 Comparison between measured backscatter coefficients (black solid line) and that from theory (pink dotted line)**

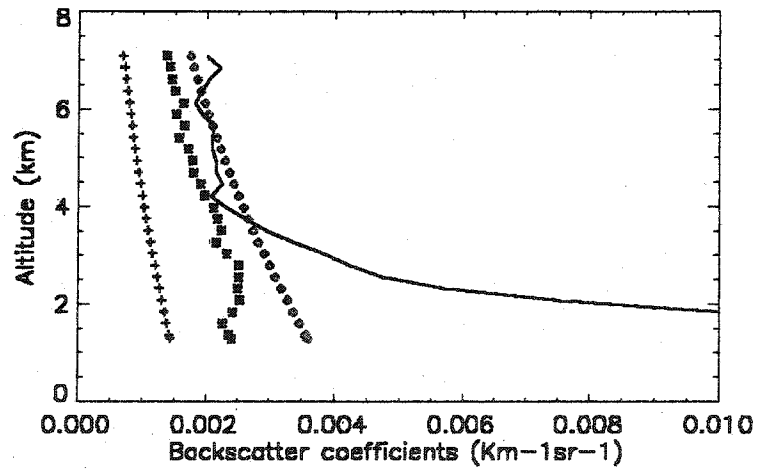


**Figure 5.7 Comparison of backscatter coefficients from GroundWinds lidar measurements, from theory, and calculated by using Landau-Placzek ratio. Red line stands for theoretical BC (Backscatter Coefs) for the air. Black line stands for calculated BC from photometric returns of GWNH data. Purple line stands for calculated BC using Landau-Placzek ratio from GWNH data. Blue square line stands for theoretical BC value assuming the air in the hydrodynamic regime**

### 5.3 An Alternative Method to Retrieve the Backscattering Coefficients

For the retrieval of backscatter coefficients, despite the slope method that we have used above, another method called ratio method (Brown 1979; Kohl 1979) can be used. Given two lidar power returns  $P_1$  and  $P_2$  at different altitude  $r_1$  and  $r_2$  respectively, we can calculate the extinction coefficient  $\sigma_m(r_1)$  at  $r_1$  using the lidar equation (5.4) for the molecular channel, that is,

$$\sigma_m(r_1) = \frac{3 \ln S_2 - \ln S_1}{8\pi \cdot 2(r_2 - r_1)}$$

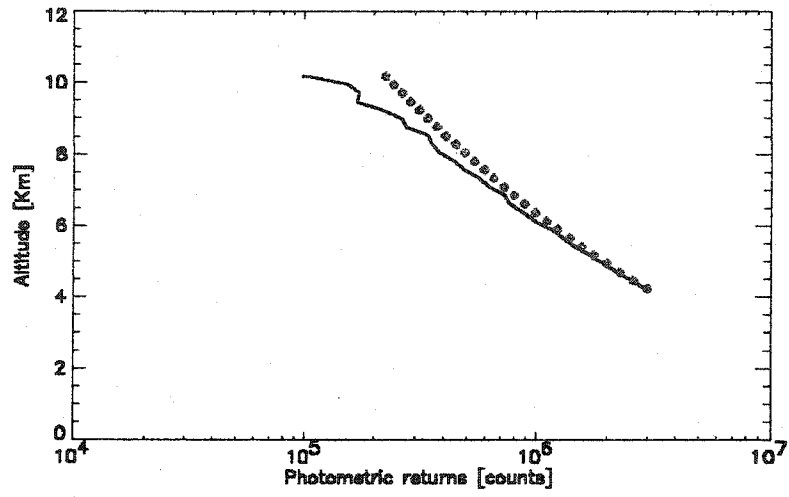
with

$$S_1 = C_1 P_2 r_2^2 O(r_1) \beta_m(r_1) \quad \text{and} \quad S_2 = C_2 P_1 r_1^2 O(r_2) \beta_m(r_2)$$

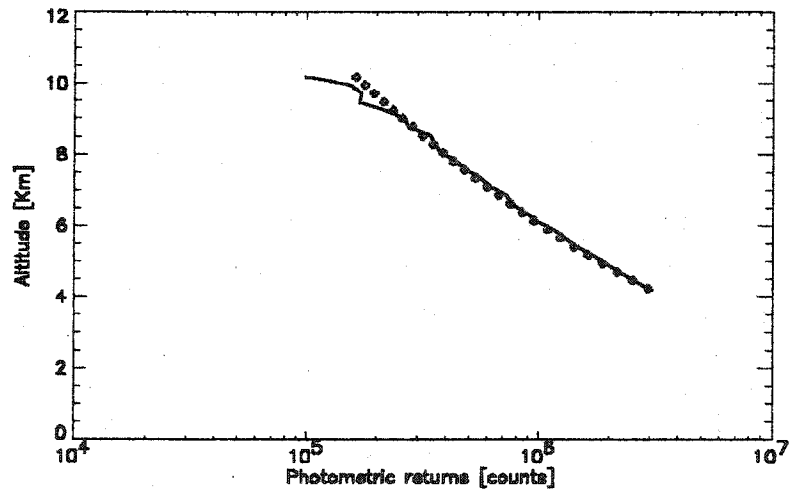
where  $C_1$  and  $C_2$  are the correction caused by the shape change of Rayleigh line in the air.

Using this ratio method, we obtained a group of Rayleigh backscatter coefficients. From 4 km to 6 km, these measured values 0.0021, 0.0023, 0.0018, 0.0025, 0.0017, 0.0024  $\text{sr}^{-1}\text{km}^{-1}$  agree well with what we retrieved from GroundWinds data using slope method in the last section. However, this method requires strong and well-behaved backscatter signals. The relative weaker signal above 6 km leads to large errors on the measured backscatter coefficients.





(a)



(b)

**Figure 5.8 Simulation of photometric returns using (a) theoretical value and (b) Twice of the theoretical value of molecular backscatter coefficients.**

Because of the surprisingly large values of the backscatter coefficients that we have measured we have performed a check of standard coefficients, as they would affect the photometric return in the raw data. In Fig. 5.8, starting with the same measured photometric return at 4 km, we computed the return at higher altitudes from the lidar formula and related parameters using different groups of backscatter coefficients. In (5.8a) the theoretical value of molecular backscatter coefficients—as we shown in figure 5.5—was used. The divergence of the simulation and the data suggests that the molecular backscatter coefficients should be larger. This is because larger backscatter coefficients will bring back more photometric returns at lower altitudes but attenuate quickly as the altitude goes up as opposed that smaller backscatter coefficients lead to a smaller—if same light source is used—but flatter photometric-return profile. In (5.8b) we arbitrarily doubled the backscatter coefficients to approximate our results. A similar simulation with these coefficients agrees with the data supporting our conclusion that the backscatter coefficients must be significantly larger than what has been assumed to date in the literature.

#### **5.4 Conclusions and Discussions**

Molecular backscatter coefficients were measured by GroundWinds lidar system with two methods: slope and ratio methods. It is, to the best of our knowledge, the first *in situ* molecular backscatter coefficients measurements of air. It is shown the measured backscatter coefficients values could be 1.5~2.0 times as large as the theoretical values. The simulation of the photometric returns agrees with our measurements (figure 5.8).

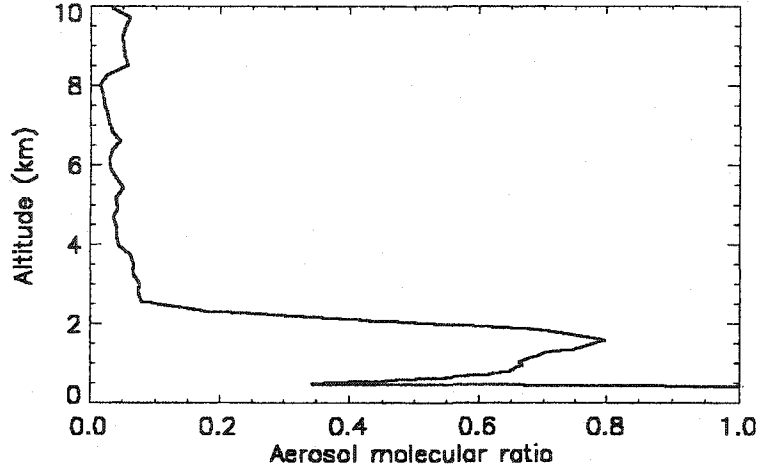


**Figure 5.9 Retrieved aerosol molecular ratio by fitting the S6 model to the measured RBS spectra.**

From the radiative transfer theory, due to the anisotropy of air molecules, molecular backscatter coefficients in the air should be slightly larger than the theoretical value calculated including the effects of the molecular anisotropies, but it should not be that large as what we have measured. The result is significant for many lidar experiments in the terrestrial atmosphere because it implies a strong backscattered signal can be achieved without enhancing the lidar transmitting power. It is worth noting that, however, the only lab verification of Rayleigh scattering cross section (Hans Naus 2000) for  $N_2$  and Ar gases with temperature at 294 K in the 560-650 nm region, agreed the theoretical estimates without Brillouin scattering. However, backscatter coefficients were not measured due to the technology used in this lab experiment. It was estimated instead.

In the analysis above, we have assumed the aerosol signal is weak. The assumption is reasonable. Because from figure 5.9, the measured aerosol backscatter signal is less than one twentieth of the molecular signal. This aerosol backscatter coefficient will account for at most 20% of the measured molecular backscatter

coefficients. This will bring down the Rayleigh backscatter coefficients to a range of 1.2~1.6 times of its theoretical value.

The reason we have a large backscatter coefficients for the air, to my opinion, is due to the rough calculation of the collective effect. For a monochromatic light being scattered by a single molecule, the differential cross section is a dipole radiation and related calculation is straightforward. For a collection of this kind of molecules that involve the scattering process, it has been assumed that each single molecule is independent from any others and the structure factors, denoted as  $F(\mathbf{q})$  in many literatures, is therefore the number of all the molecules,  $N$ . Thus, the total cross section is  $N$  times the cross section for one individual molecule. The air is not under thermodynamic equilibrium and it is not appropriate to assume each molecule is independent from its neighbor molecules. This can be seen from the Rayleigh-Brillouin spectra of the air. Only when the pressure is close to zero or the temperature is extremely high that we can conclude that the air can be described by one thermodynamic parameter—temperature. For the real air, the structure factor  $F(\mathbf{q})$  is larger than  $N$  and it should be related to the Landau-Placzek ratio, i.e., the ratio between the intensities of Brillouin doublets and unshifted Gross line.

From above analysis, for a group of gas molecules, assuming their density and pressure are not changed, the higher the temperature, the smaller the backscatter coefficients. Because when the temperature goes up, each molecule becomes more independent of others. In the mean time, the Brillouin scattering component also approaches to zero as the temperature goes up. This is exactly same as the low-pressure case where Brillouin scattering attenuates and molecules become more independent.

## CHAPTER 6

### ON THE RAYLEIGH-BRILLOUIN SCATTERING WITH EXTERNAL FORCES

#### 6.1 Introduction

We have noticed in Chapter 5 that the temperature profile retrieved from the measured Rayleigh-Brillouin lines is not as smooth as what we got from the radioSonde. Is it real or not? Or in other words, is it just statistical or real measurements of some unknown disturbances that we have not totally been clear? If it is real, what could be the causes? We can not determine these possible causes just by the data, however, we can investigate one special case in which the gas molecules—the scattering medium--subject to an external force, or light scattering in plasma and see how the Rayleigh-Brillouin scattering lineshape responds to the external forces or energy. In particular, by solving for the appropriate kinetic equations, we are able to learn how a propagating acoustic wave changes the shape of RBS line for the air.

## 6.2 Sound

Sound propagates as a longitudinal wave in air. The sound speed is about 340 meters per second. There must be a medium that is able to support the propagation of sound. It is also a longitudinal wave in which the direction of moving particles is parallel to the direction of sound energy transport. Usually human beings can hear sound with a frequency between 20 Hz and 20,000 Hz. If a sound frequency is exceeding 20,000 Hz, it is called an ultrasound or hyper-sound for very large sound frequencies. If a sound frequency is lower than 20 Hz, it is called an infrasound.

As a sound wave propagates in air, it will cause density variations that are usually small. The sound pressure level (SPL) is a measure of the mean square level of fluctuations and is defined as

$$SPL(dB) = 20 \log_{10} \left( \frac{p'}{2 \times 10^{-5} N/m^2} \right) \quad (6.1)$$

Here  $p'$  is the mean square average of the pressure fluctuations. If the instantaneous pressure at a specific location is  $p$ , the average pressure is  $p_0$ , then  $p'$  satisfies

$$p'^2 = \overline{(p - p_0)^2} \quad (6.2)$$

By expression (6.1) the threshold of hearing is  $2 \times 10^{-5} N/m^2$ . There is another common measure of sound level which is defined as,

$$PWL(dB) = 10 \log_{10} \left( \frac{w}{10^{-12} \text{ watts}} \right) \quad (6.3)$$

$w$  denotes the power of the sound wave. These two scales are approximately same in most cases.

In the air, a 130db sound wave will give a 30Pa pressure to the air and the air molecules are pushed by the sound wave with a maximum displacement at

$$A = \frac{\Delta P}{\rho v_s 2\pi f} = \frac{30Pa}{1.2kg/m^3 \times 330m/s \times 2\pi \times 1000} \approx 1.1 \times 10^{-5} m$$

where  $\rho$  is the mass density of air,  $v_s$  is the sound speed,  $f$  is the sound frequency.

### 6.3 Rayleigh-Brillouin Scattering in Gases with External Forces

It is known that Rayleigh-Brillouin scattering in neutral gases can be tackled using the linearized Boltzmann equation or a linearized Boltzmann like equation from the former chapters. Two acoustic wave modes were shown in solving the Boltzmann equation in chapter 2. The gas molecules in those cases are not subjected to any external forces, that is,  $F = 0$  in the linearized Boltzmann equation.

When there is a propagating acoustic wave or pressure wave in the air, it will impose a force on each molecule that supports the wave propagation. The air density disturbances due to the propagating pressure wave are usually small, so we can still use the linearized Boltzmann equation to describe the gas dynamics. Under this circumstance,

an additional term has to be added to the formerly used linearized Boltzmann equation. In the following derivations, we will be using the famous BGK model, because it has several advantages: it is relatively simple to be solved; and it satisfies the Boltzmann H theorem; it satisfies the mass, momentum and entropy conservation. However, since only the translational energy was considered in the BGK model, it can only be applicable to the monatomic gas. For molecular gases or mixed gases like air, the internal energy must be included to get a more rigorous result to the light scattering spectrum. However, we want to show qualitatively, by using the kinetic BGK model, that how the light scattering spectrum will change when an acoustic wave is propagating in the scatters.

The force on each interacting air molecules due to the sound wave can be described by

$$\mathbf{F} = m \mathbf{a} = m \mathbf{A} \exp(i\Omega t) \quad (6.4)$$

Here  $\mathbf{A}$  is the amplitude of the acceleration and  $m$  is the average mass of molecules.

The linearized Boltzmann equation by BGK model is

$$\left( \frac{\partial}{\partial t} + \mathbf{v} \cdot \nabla \right) h(\mathbf{r}, \mathbf{v}, t) + \mathbf{a} \cdot \frac{\partial}{\partial \mathbf{v}} f(\mathbf{r}, \mathbf{v}, t) / f_0(\mathbf{v}) = \lambda \left\{ f_0(\mathbf{v}) \rho(\mathbf{r}, t) - h(\mathbf{r}, \mathbf{v}, t) + \frac{m}{k_B T_0} \mathbf{v} \cdot \mathbf{q}(\mathbf{r}, t) + \tau(\mathbf{r}, t) \left( \frac{mv^2}{2kT_0} - \frac{3}{2} \right) \right\} \quad (6.5)$$



with initial value  $h(\mathbf{r}, \mathbf{v}, t) = \delta(\mathbf{r})$ , where  $h(\mathbf{r}, \mathbf{v}, t)$  satisfies

$$f(\mathbf{r}, \mathbf{v}, t) = f_0(\mathbf{v})(1 + h(\mathbf{r}, \mathbf{v}, t)). \quad (6.6)$$

$f(\mathbf{r}, \mathbf{v}, t)$  is the one particle distribution function.  $f_0(\mathbf{v})$  is the equilibrium Maxwellian distribution which has the form

$$f_0(\mathbf{v}) = \frac{2\pi k_B T_0}{m} \exp\left(-\frac{mv^2}{2k_B T_0}\right). \quad (6.7)$$

$T_0$  is the equilibrium temperature of the gas medium. Other symbols in equation (6.5) are

$$\rho(\mathbf{r}, t) = \int d\mathbf{v} h(\mathbf{r}, \mathbf{v}, t) f_0 \quad (6.8)$$

$$\mathbf{q}(\mathbf{r}, t) = \int d\mathbf{v} \mathbf{v} h(\mathbf{r}, \mathbf{v}, t) f_0 \quad (6.9)$$

$$\frac{3k_B T_0}{m} (\rho(\mathbf{r}, t) + \tau(\mathbf{r}, t)) = \int d\mathbf{v} v^2 h(\mathbf{r}, \mathbf{v}, t) f_0(\mathbf{v}) \quad (6.10)$$

$\tau$  is the deviation of temperature in unit, i.e., the instantaneous local temperature  $T = T_0(1 + \tau)$ .

Now, since the density variations due to the sound wave is small, and that the gas treated here is not far from the equilibrium—actually that's why we can linearize the

kinetic Boltzmann equation here, we can then set the third term on the left side of equation (6.5) to

$$\mathbf{a} \cdot \frac{\partial}{\partial \mathbf{v}} f(\mathbf{r}, \mathbf{v}, t) / f_0(\mathbf{v}) \approx \mathbf{a} \cdot \frac{\frac{\partial}{\partial \mathbf{v}} f_0(\mathbf{v})}{f_0} = -\frac{m}{2kT_0} a \quad (6.11)$$

Taking Fourier transformation of equation (6.5) to (6.10) with respect to the space variable  $\mathbf{r}$ , using expression (6.11), we obtain

$$\frac{\partial}{\partial t} h_k(\mathbf{v}, t) + i\mathbf{k} \cdot \mathbf{v} h_k = \lambda \left\{ \rho_k - h_k + \frac{2}{v_0^2} \mathbf{v} \cdot \mathbf{q}_k + \tau_k \left( \frac{v^2}{v_0^2} - \frac{3}{2} \right) \right\} + \frac{2\mathbf{v} \cdot \mathbf{a}_k}{v_0^2} \quad (6.12)$$

$$\rho_k + \tau_k = \frac{2}{3v_0^2} \int d\mathbf{v} v^2 f_0 h_k \quad (6.13)$$

with  $v_0^2 = \frac{2k_B T}{m}$ .

Here,  $h_k(\mathbf{v}, t)$  is a different representation of  $h(\mathbf{k}, \mathbf{v}, t)$ . Do the Fourier transformation again to the time variable  $t$  of equation (6.12) and (6.13), we find

$$(\lambda - i\omega + i\mathbf{k} \cdot \mathbf{v}) h_k = \lambda \rho_{k,\omega} + \frac{2\lambda}{v_0^2} \mathbf{v} \cdot \mathbf{q}_{k,\omega} + \lambda \tau_{k,\omega} \left( \frac{v^2}{v_0^2} - \frac{3}{2} \right) + h_k(\mathbf{v}, 0) + \frac{2\mathbf{v} \cdot \mathbf{a}_{k,\omega}}{v_0^2} \quad (6.14)$$

$$\rho_{k,\omega} + \tau_{k,\omega} = \frac{2}{3v_0^2} \int dv v^2 f_0 h_{k,\omega} \quad (6.15)$$

Here  $h_k(v,0)$  is the Fourier transform of time of the initial velocity distribution. For convenience, we set the direction of velocity to be parallel to the  $z$  direction, and we can discard the arrow bar from now.

Multiplying (6.14) by  $f_0$  and integrating over the velocity space, we obtain

$$-i\omega\rho_{k,\omega} + ikq_{k,\omega} = \int dv f_0(v) h_k(v,0) = \rho_k(0) \quad (6.16)$$

From the initial condition given above,  $\rho_k(0) = h_k(v,0) = 1$

Let

$$x = \frac{\omega}{kv_0}, \quad y = \frac{\lambda}{kv_0}, \quad z = x + iy$$

and

$$\xi = \frac{v}{v_0},$$

We find two equations for  $\rho(k,\omega)$  and  $\tau(k,\omega)$ :

$$\left\{ 1 - \frac{i}{\pi^{1/2}} \int d\xi \frac{\exp(-\xi^2)}{z - \xi} (y + 2xy\xi) \right\} \rho(k,\omega)$$

$$\begin{aligned}
& -y \left\{ \frac{i}{\pi^{1/2}} \int d\xi \frac{\exp(-\xi^2)}{z-\xi} (\xi^2 - 3/2) \right\} \tau(k, \omega) \\
& = \frac{1}{kv_0} \frac{i}{\pi^{1/2}} \int d\xi \frac{\exp(-\xi^2)}{z-\xi} (1 - 2yi\xi) \tag{6.17}
\end{aligned}$$

$$\begin{aligned}
& \left\{ 1 - \frac{2}{3} \frac{i}{\pi^{1/2}} \int d\xi \xi^2 \frac{\exp(-\xi^2)}{z-\xi} (y + 2xy\xi) \right\} \rho(k, \omega) \\
& + \left\{ 1 - \frac{2}{3} y \frac{i}{\pi^{1/2}} \int d\xi \frac{\xi^2 \exp(-\xi^2)}{z-\xi} (\xi^2 - \frac{3}{2}) \right\} \tau(k, \omega) \\
& = \frac{2}{3kv_0} \frac{i}{\pi^{1/2}} \int d\xi \frac{\xi^2 \exp(-\xi^2)}{z-\xi} (1 - 2yi\xi) \tag{6.18}
\end{aligned}$$

In chapter 2 we have got the relationship between the light scattering spectrum  $S(\mathbf{k}, \omega)$  and density fluctuation  $\rho(\mathbf{r}, t)$ , and it is

$$S(\mathbf{k}, \omega) = 2 \operatorname{Re} \iint dr d\omega \exp(i\mathbf{k} \cdot \mathbf{r} - i\omega t) \rho(\mathbf{r}, t) \tag{6.19}$$

Solving equation (6.17) and (6.18), we get

$$S(\mathbf{k}, \omega) \propto \rho(\mathbf{k}, \omega) = \frac{2}{k v_0} \frac{\gamma_1 \gamma_3 + \gamma_2 \gamma_4}{\gamma_3^2 + \gamma_4^2}$$

with

$$\gamma_1 = A_5 B_1 - A_6 B_2 + y(A_3 C_1 - A_4 C_2)$$

$$\gamma_2 = A_6 B_1 + A_5 B_2 + y(A_4 C_1 + A_3 C_2)$$

$$\gamma_3 = A_1 B_1 - A_2 B_2 + y(A_3 \alpha_1 - A_4 \alpha_2)$$

$$\gamma_4 = A_2 B_1 + A_1 B_2 + y(A_4 \alpha_1 + A_3 \alpha_2)$$

$$\beta_1 = 2(x^2 - y^2)(xU - yV) + 4xy(1 - yU - xV)$$

$$\beta_2 = 2(x^2 - y^2)(xV + yU - 1) + 4xy(xU - yV) - 1$$

$$\varepsilon_1 = xU - yV$$

$$\varepsilon_2 = xV + yU - 1$$

$$\varepsilon_3 = (x^2 - y^2)U - 2xyV + y$$

$$\varepsilon_4 = (x^2 - y^2)V + 2xyU - x$$

$$\alpha_1 = 1 - \frac{2}{3}y(\varepsilon_3 + x\beta_1 + U + 2x\varepsilon_1)$$

$$\alpha_2 = -\frac{2}{3}y(\varepsilon_4 + x\beta_2 + V + 2x\varepsilon_2)$$

$$A_1 = 1 - yU - 2xy\varepsilon_1$$

$$A_2 = -y(V + 2x\varepsilon_2)$$

$$A_3 = \varepsilon_3 - U/2$$

$$A_4 = \varepsilon_4 - V/2$$

$$A_5 = U/2 + y\varepsilon_2 + a\varepsilon_1$$

$$A_6 = V/2 - y\varepsilon_1 + a\varepsilon_2$$

$$B_1 = 1 - \frac{1}{3}y(\varepsilon_3 + x\beta_1 + U - y\beta_2)$$

$$B_2 = -\frac{1}{3}y(\varepsilon_4 + x\beta_2 + V + y\beta_1)$$

$$C_1 = \frac{1}{3}(\varepsilon_3 + y\beta_2 + U + 2y\varepsilon_2 + a(\beta_1 + 2\varepsilon_1))$$

$$C_2 = \frac{1}{3}(\varepsilon_4 - y\beta_1 + V - 2y\varepsilon_1 + a(\beta_2 + 2\varepsilon_2))$$

$$W = U + iV$$

And  $W$  is the plasma dispersion function that is defined as

$$W(z) = \frac{i}{\pi^{1/2}} \int_{-\infty}^{\infty} d\xi \frac{\exp(-\xi^2)}{z - \xi}. \quad (6.20)$$

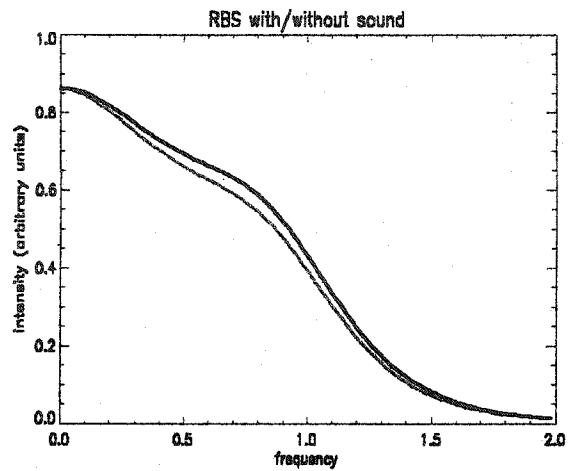


**Figure 6.1** The spectral change when an external force is applied. The blue line is the RBS spectrum of standard air at 300K and 1atm without an external force. The black line is the RBS spectrum of air, which subjects to an external force.

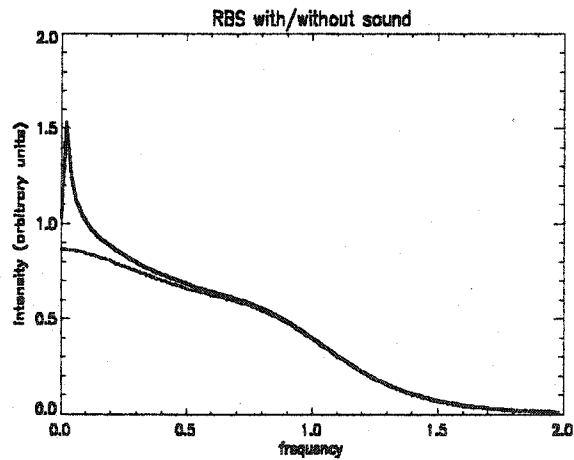


**Figure 6.2** A plot of change of the RBS spectrum when an acoustic wave is propagating in the air. The blue line is for the normal air. The black line is the RBS spectrum for the air with a propagating sound wave. The sound power level is 100db and the sound frequency is 1000Hz.

## CHAPTER 7

### CONCLUSIONS

Rayleigh-Brillouin-scattering spectral analysis is an important tool for lidar measurements of the atmosphere (wind, temperature, turbulence, etc). Additionally, the intensity of Rayleigh-Brillouin scattering can be used to measure the aerosol distribution and velocity-flow field in the troposphere. Our study of Rayleigh-Brillouin scattering in air indicates that the photometric returns of Rayleigh-Brillouin scattering are related to its spectra. We observed and described the decreasing contribution of Brillouin scattering with altitude. We also have indications that the existence of the Brillouin spectral components increases the intensity of backscattered light.

Temperature profiles were obtained using Rayleigh-Brillouin spectra measured by a high-resolution direct detection incoherent lidar system—the GroundWinds lidar system. Wind turbulence can also be measured using variance analysis of the time series of the measured Rayleigh-Brillouin spectra. By the theory of Rayleigh-Brillouin scattering with external forces developed in chapter 6, acoustic wave, Rayleigh-Brillouin scattering spectra in low-temperature plasma, and latent energy will change the shape of Rayleigh-Brillouin scattering spectra. Therefore, future measurements of these properties and phenomena can be performed—in some cases, with improved optical technology.

For temperature retrieval in the lower atmosphere, using a simplified Gaussian lineshape to describe the elastic part of Rayleigh scattering—the Cabannes line—is risky in the kinetic regime that applies in the lower atmosphere. This is because the Cabannes (also Rayleigh-Brillouin) line shape has two components: one is due to the pressure fluctuations (Brillouin scattering) and the other is due to the temperature dependent



molecular velocity distribution (thermal fluctuations). Thus, the width of the Cabannes line is not only a function of temperature, but also a function of pressure. The Brillouin component tends to increase the width of the Cabannes line. Therefore, using a simplified Gaussian in air temperature retrievals leads to incorrect lapse rates and anomalously large temperatures. At very high altitudes the pressure-fluctuation induced Brillouin scattering component is small, so a Gaussian may then be adequate for the temperature measurements using Rayleigh spectra. The temperature measured with GroundWinds, with the exception of a positive offset, tracks the temperature lapse rate as measured with radiosondes showing that the RBS spectrum can be effectively used for remote temperature measurements.

Molecular backscatter coefficients were measured using the molecular photometric returns of GroundWinds lidar system. From our measurements, the molecular backscatter coefficients are at least 1.5 times of the theoretical counterparts. So, if this can be confirmed, it will have a significant effect on the space-lidar power or other mission components.

Future measurements of polarized Rayleigh-Brillouin spectra in air by GroundWinds lidar system are necessary to further assess the current Tenti S6 model as a basis for improving its capabilities and performance for temperature and other atmospheric measurements.

## REFERENCES

- Abreu, V. J., Killeen T.L., and Hays, P.B. (1981). "Tristatic High Resolution Doppler Lidar to Study Winds and Turbulence." Applied Optics 20: 2196-2202.
- Atlas, R. M. (1997). "Atmospheric observations and experiments to assess their usefulness in data assimilation." Journal of Meteorological society of Japan 75: 111.
- Baker, W. E., Emmitt, G.D., Robertson, F., Atlas, R.M., Molinari, J.E., Bowdle, D.A., Paegle, J., Hardesty, R.M., et al (1998). "Lidar measured winds from space: a key component for weather and climate prediction." Bull. American Meteorological Society 79: 581-599.
- Bates, D. R. (1984). Planetary Space Science 32: 785.
- Bhatnagar, P. L., E.P. Gross and M. Krook (1954). "A Model for Collision Processes in Gases. I. Small Amplitude Processes in Charged and Neutral One-Component Systems." Physical Review 94(3): 511.
- Brillouin, L. (1922). Annal physics(Paris) 17: 88.
- Brown, R. T. (1979). Journal of Applied Meteorology 18: 711.
- Bucholtz, A. (1995). "Rayleigh scattering calculations for the terrestrial atmosphere." applied optics 34(15): 2765.
- Bucholtz, A. (1995). "Rayleigh-scattering calculations for terrestrial atmosphere." Applied Optics 34: 2765.
- Cabannes, J. (1921). Annal physics 15: 5-150.
- Chanin, M. L. e. a. (1989). "A Doppler lidar for measuring winds in the middle atmosphere." Geophysical research letters 16: 1273.
- Chen, W., Chiang C, Nee, J. (2002). "Lidar ratio and depolarization ratio for cirrus clouds." Applied Optics 41(30): 6470.
- Fabelinskii, I. L. (1997). "Spectra of molecular scattering of light." progress in optics 37: 95.
- Fielding, J., et al (2002). "Polarized/Depolarized Rayleigh Scattering for Determining Fuel Concentrations in Flames." Proceeding of The Combustion Institute 29: 2703-2709.

- Fischer, K. F., et al (1995). "Visible wavelength Doppler lidar for measurement of wind and aerosol profiles during day and night." optical Engineering 34: 499.
- Flesia, C., and Korb, C.L. (1999). "Theory of the double-edge molecular technique for Doppler lidar wind measurements." Applied Optics 38(3): 432.
- Flesia, C., Korb, C.Laurence (1999). "Theory of the Double-Edge Molecular Technique for Doppler Lidar Wind Measurement." applied optics 38(3): 432.
- G. Fiocco, e. a. (1971). "Measurement of Temperature and Aerosol to Molecule Ratio in the Troposphere by Optical Radar." Nature, Physical Science 229(January): 78.
- G. Fiocco, J. B. D. (1968). "Frequency Spectrum of Laser Echoes from Atmospheric Constituents and Determination of the Aerosol Content of Air." Journal of the atmospheric Science 25: 488.
- Gentry, B. M., Chen, H., Li, S.X. (2000). "Wind measurements with 355-nm molecular Doppler lidar." optics letters 25(17): 1231.
- Hans Naus, W. U. (2000). "Experimental verification of Rayleigh scattering cross sections." optics letter 25(5): 347.
- Hays P.B., A., V.J., Dobbs, M.E., Gell, D.A., Grassl, H.J., and Skinner, W.R. (1993). "The High Resolution Doppler Imager on the upper atmosphere research satellite." Journal of Geophysical Research 98: 10713.
- Hays, P. B. (1990). "Circle To Line Interferometer Optical System." Applied Optics 29(10): 1482.
- Hernandez, G. (1986). "Fabry-Perot Interferometers." **Cambridge Studies in Modern Optics.**
- Huffaker, R. M., Beran, D.W., Little, C.G. (1976). "Pulsed Coherent Lidar systems for airborne and satellite based wind field measurement." AMS.
- Huffaker, R. M. a. H., R.M. (1966). "Remote Sensing of atmospheric wind velocities using solid-state and CO<sub>2</sub> coherent laser systems." Proc. IEEE 84: 181-204.
- Kavaya, M. J., Sammy W. Henderson, James R. Magee, Charley P. Hale, R. Milton Huffaker (1989). "Remote wind profiling with a solid-state Nd:YAG coherent lidar system." Optics Letters 14(15): 776.
- Killeen, T. L., Hays, P.B. (1984). "Doppler Line profile analysis for a multichannel Fabry-Perot interferometer." Applied Optics 23(4): 612-620.
- Kohl, R. H. (1979). Journal of Applied Meteorology 18: 712.

- Korb, C. L., Gentry, B.M (1998). "Theory of the Double-Edge Technique for Doppler Lidar Wind Measurement." applied optics 37(15): 3097.
- I Sicard, P. C., Jacques Pelon, Jae Gwang Won, Soon-Chang Yoon (2002). "Variational Method for the Retrieval of the Optical Thickness and the Backscatter Coefficient from Multiangle Lidar Profiles." Applied Optics 41(3): 493.
- Landau, L. D., and G. Placzek (1934). Physics. Z. Sowjetunion 5: 192.
- Landau, L. D., Lifshitz (1985). "Electrodynamics of Continuous Media."
- Lao, Q. H., P. E. Schoen, and B. Chu (1976). "Rayleigh-Brillouin scattering of gases with internal relaxation." J. Chem. Phys. 64(9): 3547.
- Lothian, G. F. (1975). "Optics and its uses." Van Nostrand Reinhold company.
- Loudon, R. (2000). "The Quantum Theory of Light."
- Mandelshtam, L. I. (1913). Annal physics (Leipzig) 41: 609.
- May, H. M. a. A. D. (1975). Canadian Journal of Physics 53: 343.
- May, V. G.-M. a. A. D. (1980). "Rayleigh-Brillouin spectrum of compressed He, Ne, and Ar. I. Scaling." PHYSICAL REVIEW A 22(2): 692.
- McKay, J. A. (2000). "Comment on Theory of the Double-Edge Molecular Technique for Doppler Lidar Wind Measurement." applied optics 39(6): 993.
- Mountain, R. (1966). "Spectral distribution of Scattered light in a simple fluid." Review of Modern Physics 38: 205.
- O'Connor, T., et al (1975). " Experimental determination of the Landau-Placzek ratio for liquid helium to the lamda line." Journal of physics: C Solid State physics 8: 101-108.
- P. C. Wait , T. P. N. (1996). "Landau Placzek ratio applied to distributed fibre sensing." optics communications 122(4-6): 141-146.
- Pecora, R. (1964). "Doppler Shifts in Light Scattering from Pure Liquids and Polymer Solutions." THE JOURNAL OF CHEMICAL PHYSICS 40(6): 1604.
- Penndorf, R. (1957). Journal of optical Society of America 47: 176.
- Rayleigh, L. (1871). Philos. Mag(4) 41: 107, 274.
- Rayleigh, L. (1899). Philos. Mag(5) 12: 81.

Rye, B. J. (1998). "Molecular backscatter heterodyne lidar: a computational evaluation." Applied Optics **37**(27): 6321.

Sandoval, R. P. a. A. R. L. (1976). "Rayleigh Brillouin spectra in molecular nitrogen." Physical Review A **13**: 752.

Schwiesow R., L. L. (1981). "Temperature profiling by Rayleigh scattering lidar." Applied Optics **20**(11): 1972.

Tenti, G., C.D. Boley, AND RASHMI C. DESAI (1974). "On the Kinetic Model Description of Rayleigh-Brillouin Scattering from Molecular Gases." Canadian Journal of Physics **52**(4): 285.

Tepley, C. S., Sargoytchev, and C. Hines (1991). "Initial Doppler Rayleigh Lidar Results from Arecibo." Geophysical research letters **18**: 167.

Van, Leeuwen, J. M. J., Yip, S. (1965). "Derivation of Kinetic Equations for Slow-Neutron Scattering." Physical Review **139**(4A): A 1138.

Vaughan, J. M. (1989). "The Fabry-Perot Interferometer." Adam Hilger.

Xingguo Pan, M. N. S., and Richard B. Miles (2002). "Coherent Rayleigh-Brillouin Scattering." PHYSICAL REVIEW LETTERS **89**(18): 183001-1.

Yan, H.-X., et al (2000). "Numerical simulation of an adaptive optics system with laser propagation in the atmosphere." Applied Optics **39**(18): 3023.

Yip, S. (1971). "Rayleigh Scattering in Dilute Gases." The Journal of the Acoustical Society of America **49**(3 (Part 3)): 941.

Yip, S. a. S. A. (1967). "Kinetic Model Analysis of Light Scattering by Molecular gases." THE PHYSICS OF FLUIDS **10**(9): 1911.

Young, A. T. (1982). "Rayleigh Scattering." PHYSICAL TODAY: 42.

## APPENDIX

### The Plasma Dispersion Function

The Hilbert transform of a Gaussian function is defined as *plasma dispersion function*:

$$W(\xi) = \frac{i}{\sqrt{\pi}} \int_{-\infty}^{\infty} \frac{\exp(-t^2)}{t - \xi} dt \quad (\text{A.1})$$

Here  $\xi$  is complex. The plasma dispersion function is commonly encountered in the plasma physics, where different kinds of kinetic equations are used to study the properties of ionized gases.

The plasma dispersion function is very important in many kinetic theories and plasma physics; it is useful for us to list its main properties here:

$$1) W'(\xi) = 2(\xi W - i)$$

This is because,

$$W'(\xi) = \frac{i}{\pi^{1/2}} \int_{-\infty}^{\infty} \frac{\exp(-t^2)}{(t - \xi)^2} dt = -\frac{i}{\pi^{1/2}} \int_{-\infty}^{\infty} \frac{2t}{t - \xi} \exp(-t^2) dt = 2(\xi W - i).$$

$$2) \frac{i}{\pi^{1/2}} \int_{-\infty}^{\infty} \frac{t}{\xi - t} \exp(-t^2) dt = \xi W - i$$

Proof. This can be seen from 1).

$$3) \frac{i}{\pi^{1/2}} \int_{-\infty}^{\infty} \frac{t^2}{\xi - t} \exp(-t^2) dt = \xi(\xi W - i)$$

Proof.

$$\frac{i}{\pi^{1/2}} \int_{-\infty}^{\infty} \frac{t^2}{\xi - t} \exp(-t^2) dt = \frac{i}{\pi^{1/2}} \int_{-\infty}^{\infty} \left( \frac{\xi}{\xi - t} - 1 \right) t \exp(-t^2) dt = \xi(\xi W - i)$$

$$4) \frac{i}{\pi^{1/2}} \int_{-\infty}^{\infty} \frac{t^3}{\xi - t} \exp(-t^2) dt = \xi^2(\xi W - i) - i/2$$

$$5) \frac{i}{\pi^{1/2}} \int_{-\infty}^{\infty} \frac{t^4}{\xi - t} \exp(-t^2) dt = \xi^3(\xi W - i) - \frac{i}{2}\xi$$

6) An alternative representation of the plasma dispersion function is:

$$W(\xi) = -2 \exp(-\xi^2) \int_{-\infty}^{i\xi} \exp(-t^2) dt.$$

Using this expression, we can get,



7) For small  $\xi$ , the plasma dispersion function can be expanded to:

$$W(\xi) = -\pi^{1/2} \exp(-\xi^2) - 2i\xi \left( 1 + \frac{2\xi^2}{3} + \frac{4\xi^4}{15} - \frac{8\xi^6}{105} + \dots \right). \quad (\text{A.2})$$

8) For large  $\xi$ , where  $\xi = x + iy$ , the plasma dispersion function  $W(\xi)$  can be expanded asymptotically into,

$$W(\xi) = -\pi^{1/2} \eta \exp(-\xi^2) - 2i\xi^{-1} \left( 1 + \frac{1}{2\xi^2} + \frac{3}{4\xi^4} + \frac{15}{8\xi^6} + \dots \right). \quad (\text{A.3})$$

Here,

$$\eta = \begin{cases} 0 & y > 1/x \\ 1 & |y| < 1/x, \quad x > 0 \\ 2 & y < -1/x \end{cases}$$